2020-01-28

Numerical Analysis of Supersonic and Hypersonic Intake Systems with Nanoparticle Injection

Jagannathan, Rangesh

UNIVERSITY OF CALGARY

Numerical Analysis of Supersonic and Hypersonic Intake Systems

with Nanoparticle Injection

by

Rangesh Jagannathan

A THESIS

SUBMITTED TO THE FACULTY OF GRADUATE STUDIES

IN PARTIAL FULFILLMENT OF THE REQUIREMENTS FOR THE

DEGREE OF DOCTOR OF PHILOSOPHY

GRADUATE PROGRAM IN MECHANICAL AND MANUFACTURING ENGINEERING

CALGARY, ALBERTA

JANUARY, 2020

Abstract

Inter-phase momentum and energy transfer interactions in gas-particle flows were studied for applications in high-speed airbreathing engines. The overall aim of the thesis is to investigate nanoparticle injection across high-speed intake systems. In the first stage, existing numerical strategies were assessed for the modeling of compressible, gas-nanoparticle flows. Based on a detailed literature review, a combination of quasi-1D and 3D computational fluid dynamic (CFD) approaches were selected. CFD simulations were conducted using a custom-modified, unsteady, compressible, Eulerian-Lagrangian gas-particle CFD solver in OpenFOAM. A novel solution verification method was developed for predicting numerical uncertainties in multiphase flow simulations with one-way coupling, which was used to verify the CFD solutions.

In the second stage, the effect of nanoparticle injection on the performance of supersonic/hypersonic intake systems was investigated. A parametric study using Mach number (M_∞), Stokes number (Stk), particle Eckert number (Ec_p), particle mass loading ratio (S_L), and thermal transport number (α_t) was conducted across a quasi-1D converging-diverging (C-D) supersonic intake at idealized and single-shock compression cases. Gains in pressure recovery were observed at specific combinations of the five input parameters, which was further investigated. The 1D study was followed by CFD simulations of a rectangular, mixed-compression intake at Mach 3. The CFD results predicted a 16% gain in pressure recovery, consistent with the 1D model predictions.

In the final stage, starting and buzz characteristics of high-speed intakes were investigated with nanoparticle injection. Isentropic and Kantrowitz contraction limits were estimated at particle mass loading ratios of 0, 0.12 and 0.24. These results were followed by CFD simulations of a 2D, external compression intake with an operating Mach number of 2. The CFD study was conducted at particle mass loading ratios of 0, 0.12 and 0.24; and nozzle throttling ratios from 0.57 to 0.44. The effect of nanoparticle injection on the Ferri-type instability and unstart were investigated. The potential for nanoparticles to attenuate buzz, once the instabilities are triggered, was also assessed.

Acknowledgments

To Prof. Craig Johansen: the Vito to my Michael.

To Benjamin, Colin, Declan, Derek, Graham, Henry and Mr. T: for being hyper-competitive and supportive at the same time.

To Marcel, Connor and Schuyler: for beers, CFD and socialism

To Madhu, Vivek, Madhuri, Parag, Akshay, Harsha, Varun, Poornima, and Sneja, my grownup friends that have taught me so much.

Finally, to my family- Amma, Appa, Suba and Sanjay: for everything

Preface

This is a manuscript-based dissertation adopted from the following patent, journal and conference publications:

1. Dass, P., Johansen, C., Jagannathan, R., & Trivedi, M. (2016) Pre-cooled airbreathing engine, Patent (PCT/CA2016/051289)

2. Jagannathan, R., Hinman, W. S., & Johansen, C. T. (2019). Solution verification of multiphase flows with one-way coupling. *Journal of Computational Physics*, 109033.

3. Jagannathan, R., Hinman, W. S., & Johansen, C. (2019). Performance assessment of supersonic and hypersonic intake systems with nano-particle injection. *Acta Astronautica*, 159, 609-621.

4. Jagannathan, R., & Johansen, C., (2019) Numerical assessment of intake buzz with nano-particles across a supersonic external compression intake. In *AIAA Joint Propulsion Conference*(AIAA-2019-4425), Indianapolis, IN.

Chapter 2 has been reproduced from Article-2 and Chapter 3 has been adopted from Article-3. A portion of Chapter 4 is based on Paper-4. Additionally, results from Chapter 4 will be submitted to the AIAA journal for journal publication. The results from this work has also supported the technical justification of Patent-1.

Table of Contents

List of Tables

List of Figures and Illustrations

List of Symbols, Abbreviations and Nomenclature

A Cross Sectional Area, m^2

A_1 First-Order Spatial Discretization Error Coefficient (Chapter 2)

A_2 Second-Order Spatial Discretization Error Coefficient (Chapter 2)

a Wave Speed, ms^{-1}

B_1 First-Order Temporal Discretization Error Coefficient (Chapter 2)

B_2 Second-Order Temporal Discretization Error Coefficient (Chapter 2)

C_D Drag Coefficient

C_p Gaseous Specific Heat Capacity at Constant Pressure, $J\,kg^{-1}\,K^{-1}$

C_{pp} Particle Specific Heat Capacity, $J\,kg^{-1}\,K^{-1}$

C_{pr} Particle-Gas Specific Heat Ratio (Appendix C)

D Diameter, m

Ec Eckert Number

f Buzz Frequency, Hz (Chapter 4)

F Force, N

h Convective Heat Transfer Coefficient, $W\,m^{-2}\,K^{-1}$

Kn Knudsen Number

ℓ Error Norms (Chapter 2)

L Axial Length Scale, m

m Mass, kg

$\dot{m}$ Mass Flow Rate, $kg\,s^{-1}$

M Mach Number

M_s Shock Strength (Chapter 3)

ΔM Operating Mach Number Range (Chapter 4)

Nu Nusselt Number

P Pressure, Pa

Pr Prandtl Number

r Grid Refinement Ratio w.r.t. most-Refined Grid

R Specific Gas Constant $J\,kg^{-1}\,K^{-1}$

Re Reynolds Number

S_{ref} Drag Reference Area, m^{-2}

S_L Particle-to-Gas Mass Flow Rate Ratio

Stk Stokes Number

T Temperature, K

V Velocity, $m\,s^{-1}$

x_{sh} Instantaneous Normal Shock Location, m (Chapter 4)

x_{msh} Time-Averaged Shock Location, m (Chapter 4)

Δx_{sh} Shock-Amplitude, m (Chapter 4)

α_t Particle Thermal Transport Number (Chapter 3)

γ Gaseous Specific Heat Ratio

Γ Non-Dimensionalized Time (Chapter 2)

δ Discretization Error (Chapter 2)

η Observed Temporal Order of Accuracy (Chapter 2)

κ Thermal Conductivity, $W\,m^{-1}\,K^{-1}$

Λ Non-Dimensionalized Velocity

μ Dynamic Viscosity, $N\,s\,m^{-2}$

ν Courant-Freidrichs-Lewvy Criterion (Chapter 2)

π Stagnation Pressure non-dimensionalized w.r.t Freestream Value

π_c Stagnation Pressure Recovery

ρ Density, $kg\,m^{-3}$

σ Standard Deviation

τ Relaxation Time-Scale, s

ϕ_p Particle Volumetric Fraction

Ψ Non-Dimensionalized Solution Variable of Interest (Chapter 2)

ψ Solution Variable of Interest (Chapter 2)

Subscript/Superscript

0   Stagnation Conditions

∞ Freestream/Reference

0∞ Freestream Stagnation Conditions (Appendices A and C)

aw   Adiabatic Wall Conditions

e   Engine/Nozzle Exit Conditions (Chapter 4)

ex   Intake Exit Conditions (Chapters 3 and 4)

ext   Extrapolated Variable (Chapter 2)

h   Spatial Discretization (Chapter 2)

τ Temporal Discretization (Chapter 2)

h, τ Spatial and Temporal Discretization (Chapter 2)

p   Particle

p∞ Freestream Particle Value (Appendices A and C)

ps   Particle Properties Estimated at Particle Surface

*p*0   Grid Independent Solution (Chapter 2)

*p*1   Particle Variable Computed at the Grid, $r = 1$ (Chapter 2)

*p*2   Particle Variable Computed at the Grid, $r = 2$ (Chapter 2)

*p*3   Particle Variable Computed at the Grid, $r = 4$ (Chapter 2)

r   Relative, w.r.t Particle

s   Gas Properties Estimated at Particle Surface

t   Throat Conditions (Chapter 4)

∗   Non-Dimensionalized Variable (Appendices A and C)

∗   Intake Sonic Exit Conditions (Chapters 3 and 4)

Conventions

A Scalar

A   Vector

A Tensor

$|\mathbf{A}|$ Magnitude of the Vector- A

Chapter 1

Introduction

Hypersonic airbreathing propulsion has been an important component of aerospace research for the last several decades. Recently, there has been a renewed interest in the field due to applications such as reusable space launch vehicles, wave-riders, long-range cruise missiles, interceptors, and commercial transportation (Heiser and Pratt, 1994; Smart and Tetlow, 2009). Airbreathing engines belong to a class of engine technologies that use atmospheric oxygen, instead of an on-board oxidizer, for combustion. Airbreathing engines are advantageous due to their re-usability and high specific impulse (Heiser and Pratt, 1994). Airbreathing engines are typically classifiable as turbojet, ramjet and scramjet engines. Turbojets are a class of engines which function using an externally powered compression device (known as the compressor). Turbojets typically operate at subsonic and transonic Mach numbers. On the other hand, both ramjet and scramjet engines undergo compression using the ramming effect of the freestream gas. Ramjets typically operate at supersonic speeds while scramjets are more suitable within the hypersonic range. Furthermore, high surface temperatures and significant pressure losses are associated with the use of any moving component within the engine at hypersonic velocities (Curran and Murthy, 1991). For these reasons, externally powered compressors are usually not considered for the design of hypersonic airbreathing engines. In such cases, the design and optimization of the compression process inside an intake system becomes critically important for the development of hypersonic airbreathing engines.

A typical intake is optimized for its performance, stability, and uniformity (Seddon and Goldsmith, 1999). The performance of an intake system is characterized by parameters such as pressure recovery (a measure of pressure losses), flow ratio, and external drag (Seddon and Goldsmith, 1999). The net standard thrust generated by the engine is directly proportional to the intake pres-

sure recovery (Heiser and Pratt, 1994). The intake pressure recovery is primarily affected by the presence of complex flow features such as the shockwaves, boundary layers and shockwave-boundary layer interactions (SBLIs). The flow ratio refers to the ratio of captured to the on-design flow entering the intake while the external drag describes the retarding force generated over the surface of the intake. The external drag can further be divided into the spillage, cowl-friction, and cowl-pressure drag (Seddon and Goldsmith, 1999). The spillage drag refers to the drag generated by the 'spillage' effect which occurs at off-design flow ratios. While performance evaluates the quality of air supplied by the intake at critical conditions, stability assesses the compatibility of an intake system with the engine when the conditions are less than ideal. Around these conditions (typically sub-critical but also for super-critical conditions for some cases), the intake exhibits a form of instability known as the buzz (Dailey, 1955; Ferri and Nucci, 1951; Fisher et al., 1970). The intake buzz typically occurs at high back pressures (throttling) or off-design Mach numbers, which is characterized by rapid oscillations of the normal shockwave across the ramp. Intake buzz causes significant losses in pressure recovery and combustion instabilities that eventually lead to the complete engine breakdown.

The above challenges to the intake design are generally addressed by: geometric optimization (Carrier et al., 2001; Gaiddon and Knight, 2003; Gaiddon et al., 2004; Smart, 1999); and auxillary flow control and cooling mechanisms (Herrmann and Gülhan, 2014; Sutton and Biblarz, 2010). Intake optimization depends on parameters such as the: operating Mach number; geometric shape (axisymmetrical, rectangular or three dimensional); geometric configuration (fixed or variable geometry); type of compression (external, internal or mixed); source of shock generation (single ramp, multiple ramps, curved ramps for isentropic compression, and shock-train design); location with respect to the aircraft (nose, top, bottom, forward, mid, aft); number of intakes (1-4); and intake-combustor interface (Mahoney, 1990). At high Mach numbers ($M > 2$), geometric optimization as a standalone design tool has been found to be insufficient for achieving the desired performance, stability and temperatures (Seddon and Goldsmith, 1999). Thus, in addition to

geometric optimization, auxillary flow control and cooling mechanisms are usually required for supersonic and hypersonic intakes. Flow control techniques can be used to minimize pressure losses (Verma and Manisankar, 2012; Zhao et al., 2014) and improve stability characteristics (Herrmann and Gülhan, 2014; Soltani et al., 2016; Trapier et al., 2006). On the other hand, high gaseous temperatures on the walls of intakes and combustors can be dealt with cooling techniques such as the film and regenerative cooling mechanisms (Chamberlain, 1992; Heufer and Olivier, 2006; Liu et al., 2012; Melis and Wang, 1999).

Overall, several studies have been published on the design and aerodynamic analysis of supersonic and hypersonic intakes. However, as discussed above, high-speed intake flows are still not thoroughly understood due to the sheer array of parameters involved, as well as due to the presence of multiple complex aerodynamic features. Thus, the present study takes a fundamental approach to understand supersonic intakes along with the use of a novel flow control technique. The method involves the injection of solid, metallic nanoparticles (Dass et al., 2017).

There are several benefits to using solid, metallic nanoparticles. First, the volumetric thermal capacity of solids are typically much higher than liquids or gases (Williams, 2015). Second, a decrease in particle size leads to an increase in the net surface area per unit volume. Thus, the use of nanosized particles can improve the rates of momentum and heat transfer between the gas and solid phases. Finally, powdered metallic fuels have been studied for ramjet combustion at high Mach numbers and burner entry temperatures, due to the relative stability of metallic oxides (combustion products) compared to their hydrocarbon counterparts at high temperatures (Goroshin et al., 2001).

In the present study, the injection of solid, metallic nanoparticles will then be tested for improved intake performance and stability at supersonic speeds. The primary research objectives of the dissertation are as follows:

1. To develop a numerical computational fluid dynamics (CFD) solver to investigate compressible gas-particle flows around the nano-regime. This includes a detailed

assessment of the existing numerical modeling and verification techniques from the literature.

2. To develop and evaluate a new approach to verify multiphase flows with one-way coupling.

3. To investigate the effect of nanoparticle injection on the performance of idealized and practical intake configurations at supersonic and hypersonic velocities.

4. To assess the impact of nanoparticle injection on stability and starting characteristics of supersonic intakes.

Chapter 2 investigates the process of solution verification for multiphase flows with one-way coupling. A new method, known as the mixed-polynomial extrapolation, was derived for estimating the discretization errors of the dispersed phase variables. Chapter 3 investigates the effect of nanoparticle injection on the performance of high-speed intakes. First, a parametric analysis (using a low-fidelity quasi-1D solver) of idealized supersonic intakes was conducted. The parametric analysis was followed by CFD simulations of a 2D, mixed-compression intake at Mach 3. Chapter 4 analyzes the impact of nanoparticles on the stability and starting characteristics of supersonic intakes. A 2D, two-shock, external compression intake was used for the CFD simulations.

Chapter 2

Solution Verification of Multiphase Flows with One-Way Coupling

2.1 Introduction

Gas-droplet and gas-particle flows represent a vast sub-group of multiphase flows having numerous applications such as spray drying, pollution control and recently, supersonic intakes (Jagannathan et al., 2019a; Loth, 2000; Schwarzkopf et al., 2011). The modeling of inter-phase interactions represents a critical aspect of gas-particle and gas-droplet flow simulations (Schwarzkopf et al., 2011). Inter-phase interaction models are typically divided into three groups: one-way, two-way and four-way coupling. When the fluid properties affects the discrete phase while the reverse effect is negligible, the flow is one-way coupled. On the other hand, if the interaction between the two phases is mutual, the flow is two-way coupled. Finally, the flows where particle-particle interactions become significant, in addition to the inter-phase interaction terms, are four-way coupled. The strategy for identifying the type of coupling depends on the application and volume fraction of the dispersed phase (ϕ_p) (Elghobashi, 1994; Schwarzkopf et al., 2011). Flows with low dispersed phase concentrations ($\phi_p < 10^{-6}$) are one-way coupled. Particle Image Velocimetry studies (Tedeschi et al., 1999), coldspray coating (Dykhuizen and Smith, 1998), and gas-particle flows through supersonic inertial separators (Musgrove et al., 2009) fall under this category. For $10^{-6} < \phi_p < 10^{-3}$, the flow is two-way coupled. Some applications include solid rocket motors (Hwang and Chang, 1988) and recently, supersonic intakes (Jagannathan et al., 2019a). The four-way coupling is used when $\phi_p > 10^{-3}$. Gasification processes across fluidized beds are four-way coupled (Yang, 2003).

Gas-particle and gas-droplet flows are typically modeled using Eulerian-Eulerian (E-E) and

5

Eulerian-Lagrangian (E-L) approaches. The E-E approach considers the particle field as a continuum (Crowe, 1982) and involves the use of closure models to estimate the fluid parameters of the particulate phase (Ibsen et al., 2004). The E-E approach can be classified into mixed and separated (also known as two-fluid) fluid models (Loth, 2000). The former assumes local dynamic and thermal equilibrium conditions between the phases, while the latter incorporates the relative velocity and temperature differences between the phases. The E-L approach (also known as the discrete particle model) treats the fluid as a continuum and the particles as discrete elements. This method can be classified into point-volume and resolved volume approaches (Loth, 2000). The former solves the particle momentum and energy equations at a point while the latter incorporates the finite volume of the discrete particles. The resolved volume approach is the most accurate method, but comes with a higher computational cost. The point-volume samples a cluster of physical particles in a cell and treats it as a single computational particle (known as the parcel), and computes the corresponding momentum and energy source terms using theoretical and empirical expressions. Flows with one-way and two-way coupling are typically modeled using the E-L approach. On the other hand, flow simulations with four-way coupling are typically modeled using an Eulerian-Eulerian approach (E-E) (Ibsen et al., 2004; Loth, 2000; Schwarzkopf et al., 2011) because of the computational costs associated with the E-L model. With the rise in high performance computing (HPC), modeling and simulations of such flows have been made possible. However, the complexity of modeling and implementing the CFD of multiphase flows increases with the dispersed phase concentration. Therefore, gas-particle and gas-droplet flow simulations necessitate an extensive verification and validation process, so as to establish the credibility of their results.

Verification refers to the process of evaluating model implementation with respect to the actual conception and solution of the intended model, while validation deals with evaluating the accuracy of physics involved in the mathematical model (Roache, 1998). Verification is divided into code and solution verification. Code verification is further classified into numerical algorithm testing and software quality assessment. The former refers to estimating the accuracy of numerical al-

gorithms used in the model, while the latter deals with the reliability of the software code itself. Solution verification is the process of quantifying the different types of numerical errors associated with the model (Roy, 2005). Numerical errors in CFD are classified into round-off, iterative convergence, and discretization errors. Round-off errors arise due to the arithmetic limits imposed by the computers (Oberkampf and Trucano, 2002). These errors can be minimized by using double-precision calculations and 64-bit computer architecture (Roy, 2005). Iterative convergence (IC) errors are generated due to insufficient residual tolerances between iterations. A general way of estimating the IC error is by monitoring the residuals after each iteration and terminating the simulation only after the iterations converge. Another approach is to use the solutions computed at three different iteration levels to estimate the IC error (Roy and Blottner, 2001). The discretization error arises from the approximations made in simplifying a system of partial differential equations into a set of algebraic equations (Oberkampf and Trucano, 2002; Roache, 1998). Discretization error estimators are typically classified into *a priori* and *a posteriori* methods (Roy, 2005). *A priori* methods assess the behavior of discretized equations without obtaining a numerical solution while *a posteriori* error estimators usually require a set of numerically parameterized solutions. The most popular approach, known as the Richardson extrapolation (Richardson, 1911; Richardson and Gaunt, 1927), estimates error *a posteriori*. This method calculates a higher order estimate of the exact solution based on CFD solutions at multiple grid refinements levels.

While there are several studies on the verification of single-phase flows (Oberkampf and Roy, 2010; Oberkampf and Trucano, 2002; Roache, 1997; Roy, 2005), there are few notable studies on multiphase flows (Brady et al., 2012; Choudhary and Roy, 2018; Choudhary et al., 2016; Musser and Choudhary, 2015; Shahnam et al., 2016). Studies by Musser and Choudhary (2015), Brady et al. (2012), and Choudhary et al. (2016) focus on the code verification of multiphase flows using the method of manufactured solutions (MMS). Recently, solution verification studies were conducted for the multiphase gasification process in fluidized beds (Choudhary and Roy, 2018; Shahnam et al., 2016). The studies utilized an E-E approach to model the fluid-particle systems.

7

Volumetric particle concentrations were considerably high ($\phi_p > 0.1$), implying that the flows were four-way coupled.

The present study investigates the solution verification process for gas-particle flows with one-way coupling, which were modeled using an E-L approach. Flows with one-way coupling, modeled using an E-L approach, provides a fundamental perspective into the problem by focusing on the individual particle characteristics. A combination of *a priori* and *a posteriori* approaches has been used to devise a novel way of estimating the discretization errors for multiphase flows. CFD simulations were conducted using a custom, compressible E-L solver in OpenFOAM.

2.2   A Priori Error Investigation

This section investigates the sources of discretization error for the dispersed phase variables. Particle motion is described by the generic time-dependent ordinary differential equation (ODE) as shown in Eq. 2.1, where ψ_p represents the particle solution variable (velocity or temperature) and S_ψ is the source term from the carrier phase. The source term is expanded to give Eq. 2.2.

$$\frac{d\psi_p}{dt} - S_\psi = 0 \tag{2.1}$$

$$\frac{d\psi_p}{dt} - \frac{1}{\tau_\psi}(\psi - \psi_p) = 0 \tag{2.2}$$

where ψ is the gas phase solution variable (velocity or temperature) and τ_ψ is the relaxation time constant. Eq. 2.2 is discretized using a first order scheme (Eq. 2.3).

$$\frac{\psi_p^{n+1} - \psi_p^n}{\Delta t} - \frac{1}{\tau_\psi}(\psi_j^n - \psi_p^n) = 0 \tag{2.3}$$

The term, ψ_p^{n+1}, is then expanded using the Taylor series (Eq. 2.4) and re-arranged to give Eq. 2.5.

$$\psi_p^{n+1} = \psi_p^n + \left(\frac{d\psi_p}{dt}\right)^n \Delta t + \left(\frac{d^2\psi_p}{dt^2}\right)^n \frac{\Delta t^2}{2} + O(\Delta t^3) \tag{2.4}$$

$$\frac{\psi_p^{n+1} - \psi_p^n}{\Delta t} = \left(\frac{d\psi_p}{dt}\right)^n + \left(\frac{d^2\psi_p}{dt^2}\right)^n \frac{\Delta t}{2} + O(\Delta t^2) \tag{2.5}$$

Eq. 2.5 is then substituted in Eq. 2.3,

$$\frac{d\psi_p}{dt} - \frac{1}{\tau_\psi}(\psi - \psi_p) = -\frac{\Delta t}{2}\frac{d^2\psi_p}{dt^2} - O(\Delta t^2) \tag{2.6}$$

The numerical solution of Eq. 2.2 (obtained through Eq. 2.3) constitutes an exact solution to a different differential equation (described by Eq. 2.6). The right hand side of Eq. 2.6 is known as the truncation error to the ODE (Anderson and Wendt, 1995).

The truncation or discretization error can be estimated using *a posteriori* analysis known as the generalized Richardson extrapolation (Oberkampf and Trucano, 2002; Richardson, 1911; Roache, 1998). In this method, the discretization error $((\delta_\tau)_p)$ is approximated using a power series expansion

$$(\delta_\tau)_p = \frac{\psi_p(\Delta t \to 0) - \psi_p(\Delta t)}{\psi_p(\Delta t \to 0)} = B\Delta t^\eta + O(\Delta t^{\eta+1}) \tag{2.7}$$

η represents the temporal order of convergence of the particle solution variable, ψ_p, and B is the error coefficient. For an ηth order accurate solution, the extrapolated solution will be $(\eta + 1)^{th}$ order accurate.

In addition to the temporal discretization error, the particle solution is also affected by the discretization of gas-phase equations. Under such circumstances, the validity and accuracy of the generalized Richardson extrapolation method is not known. In the current study, a different approach to estimate discretization errors has been derived. The present study focuses on compressible gas-particle flows. For this purpose, the gas-phase solution variable, ψ, has been simplified to follow a hyperbolic, 1D wave equation (Eq. 2.8).

$$\frac{\partial \psi}{\partial t} + a\frac{\partial \psi}{\partial x} = 0 \tag{2.8}$$

9

where a denotes the wave speed. Considering a first-order forward difference scheme in time and first-order rearward difference in space, the expression for truncation error is obtained for the gas-phase variable (a detailed explanation of the procedure is given in (Anderson and Wendt, 1995))

$$\frac{\partial \psi}{\partial t} + a\frac{\partial \psi}{\partial x} = \frac{a\Delta x}{2}(1-v)\frac{\partial^2 \psi}{\partial x^2} + \frac{a(\Delta x)^2}{6}(3v - 2v^2 - 1)\frac{\partial^3 \psi}{\partial x^3}$$
$$+O\left[(\Delta t)^3, (\Delta t)^2(\Delta x), (\Delta t)(\Delta x)^2, (\Delta x)^3\right] \tag{2.9}$$

$$v = \frac{a\Delta t}{\Delta x} \tag{2.10}$$

where v is the Courant-Freidrichs Levy (CFL) number, and usually varies from 0 to 1 (in the present study, v is kept constant at 0.1 (Greenshields et al., 2010)). Based on Eq. 2.9, the gas-phase discretization error is written as (approximated upto 2 orders)

$$\delta_h = A_1\Delta x + A_2(\Delta x)^2 + O\left[(\Delta t)^3, (\Delta t)^2(\Delta x), (\Delta t)(\Delta x)^2, (\Delta x)^3\right] \tag{2.11}$$

where A_1 and A_2 are error coefficients for first and second-order terms. Eq. 2.6 can be non-dimensionalized using the relations $\Psi_p = \psi_p/\psi_\infty$, $\Psi = \psi/\psi_\infty$, $\Gamma = t/\tau_\psi$,

$$\frac{d\Psi_p}{d\Gamma} - (\Psi - \Psi_p) = -\frac{\Delta t}{2\tau_\psi}\frac{d^2\Psi_p}{d\Gamma^2} - \frac{(\Delta t)^2}{6\tau_\psi^2}\frac{d^3\Psi_p}{d\Gamma^3} + O(\Delta t)^3 \tag{2.12}$$

ψ from Eq. 2.13 and δ_h from Eq. 2.11 are substituted into the above equation to arrive at Eq. 2.14.

$$\Psi(\Delta x) = \Psi(\Delta x \to 0) - \delta_h \tag{2.13}$$

$$\frac{d\Psi_p}{d\Gamma} - [\Psi(\Delta x \to 0) - \Psi_p] = -A_1\Delta x - A_2(\Delta x)^2 - \frac{\Delta t}{2\tau_\psi}\frac{d^2\Psi_p}{d\Gamma^2} - \frac{(\Delta t)^2}{6\tau_\psi^2}\frac{d^3\Psi_p}{d\Gamma^3}$$
$$+O\left[(\Delta t)^3, (\Delta t)^2(\Delta x), (\Delta t)(\Delta x)^2, (\Delta x)^3\right] \tag{2.14}$$

As observed in the above equation, the particle solution variable is affected by the two different discretization schemes in Eqs. 2.2 and 2.9. The impact of these two discretization schemes is

further understood by analyzing the particle momentum equation as an example. Here $\psi_p = V_p$, $\Psi_p = \Lambda_p$, and ignoring higher order terms,

$$\frac{d\Lambda_p}{d\Gamma} - [\Lambda(\Delta x \to 0) - \Lambda_p] = -A_1 \Delta x - A_2(\Delta x)^2 - \frac{\Delta t}{2\tau_v} \frac{d^2 \Lambda_p}{d\Gamma^2} - \frac{(\Delta t)^2}{6\tau_v^2} \frac{d^3 \Lambda_p}{d\Gamma^3} \qquad (2.15)$$

where Λ is the non-dimensionalized velocity and τ_v is the dynamic relaxation time scale. Using a Stokes drag approximation,

$$\tau_v = \frac{\rho_p D_p^2}{18\mu} \qquad (2.16)$$

$$Stk = \frac{\tau_v}{\Delta t} \qquad (2.17)$$

Eq. 2.15 now becomes,

$$\frac{d\Lambda_p}{d\Gamma} - [\Lambda(\Delta x \to 0) - \Lambda_p] = -A_1 \Delta x - A_2(\Delta x)^2 - \frac{1}{2(Stk)} \frac{d^2 \Lambda_p}{d\Gamma^2} - \frac{1}{6(Stk)^2} \frac{d^3 \Lambda_p}{d\Gamma^3} \qquad (2.18)$$

Since *Stk* is proportional to the square of particle diameter, the temporal discretization error will dominate at smaller particle diameters, while the impact of the gas phase source term will have an increased significance at larger diameters.

2.2.1 Mixed Polynomial Extrapolation

Based on the above analysis, a new method has been introduced to estimate the discretization error of the discrete phase variables. The method employs a mixed spatial and temporal polynomial extrapolation as described by

$$\begin{aligned}
(\delta_{h,\tau})_p &= A_1(\Delta x) + A_2(\Delta x)^2 + B_1(\Delta t) + B_2(\Delta t)^2 \\
&\quad + O\left[(\Delta t)^3, (\Delta t)^2(\Delta x), (\Delta t)(\Delta x)^2, (\Delta x)^3 \right]
\end{aligned} \qquad (2.19)$$

A 3-point grid solution is employed to calculate the grid independent solution. A similar approach was used by Roy (2003) that involved mixed-order spatial schemes to assess grid convergence in hypersonic flows.

$$\psi_{p0} - \psi_{p1} = A_1(\Delta x) + A_2(\Delta x)^2 + B_1(\Delta t) + B_2(\Delta t)^2 \tag{2.20}$$

$$\psi_{p0} - \psi_{p2} = A_1(r\Delta x) + A_2(r\Delta x)^2 + B_1(r\Delta t) + B_2(r\Delta t)^2 \tag{2.21}$$

$$\psi_{p0} - \psi_{p3} = A_1(r^2\Delta x) + A_2(r^2\Delta x)^2 + B_1(r^2\Delta t) + B_2(r^2\Delta t)^2 \tag{2.22}$$

where ψ_{p0} is the exact solution, and ψ_{p1}, ψ_{p2} and ψ_{p3} represent the discretized CFD solutions from refined, medium, and coarse grid, respectively. A and B are coefficients, while Δx and Δt denote the spatial and temporal grid dimensions. The variable, r, is known as the grid refinement ratio.

$$C_1 = A_1(\Delta x) + B_1(\Delta t) \tag{2.23}$$

$$C_2 = A_2(\Delta x)^2 + B_2(\Delta t)^2 \tag{2.24}$$

By substituting Eqs. 2.23 and 2.24 in Eqs. 2.20-2.22, the error expressions are simplified into Eqs. 2.25-2.27.

$$\psi_{p0} - \psi_{p1} = C_1 + C_2 \tag{2.25}$$

$$\psi_{p0} - \psi_{p2} = rC_1 + r^2C_2 \tag{2.26}$$

$$\psi_{p0} - \psi_{p3} = r^2C_1 + r^4C_2 \tag{2.27}$$

The variables C_1, C_2 and ψ_{p0} are the obtained from Eqs. 2.28-2.30.

$$C_1 = \frac{r^2 \psi_{p1} + \psi_{p3} - \psi_{p2}\left(1+r^2\right)}{r\left(1-r\right)^2} \tag{2.28}$$

$$C_2 = \frac{\psi_{p2}\left(1+r\right) - r\psi_{p1} - \psi_{p3}}{r\left(1-r^2\right)\left(1-r\right)} \tag{2.29}$$

$$\psi_{p0} = \psi_{p1} + C_1 + C_2 \tag{2.30}$$

The above method is applicable only when: the source code of the solver has been verified; the grid solutions exhibit an asymptotic convergence; and the iterative convergence errors are negligible (Oberkampf and Trucano, 2002). Two test cases of supersonic flows, with a single particle injected along with the gas, across a compression ramp and diverging duct were considered for the study. CFD simulations were conducted using a custom-modified, Eulerian-Lagrangian, compressible gas-particle solver in OpenFOAM. The mixed polynomial extrapolation method is evaluated using a property of the dispersed phase as the solution variable of interest.

2.3 Governing Equations

The solver is comprised of an Eulerian component that solves for the carrier gas phase and a Lagrangian component that solves for the dispersed solid phase.

2.3.1 Carrier Gas Phase

The carrier gas phase equations are represented by

(i) **Continuity equation**:

$$\frac{\partial \rho}{\partial t} + \nabla \cdot \left(\rho \mathbf{V}\right) = 0 \tag{2.31}$$

(ii) **Momentum Equation**:

$$\frac{\partial \rho \mathbf{V}}{\partial t} + \nabla \cdot \left[\left(\rho \mathbf{V}\right) \mathbf{V}^{\mathrm{T}}\right] = -\nabla P + \nabla \cdot \tau + \mathbf{S}_M \tag{2.32}$$

where $\mathbf{S}_M$ represents the momentum source term due to the dispersed phase and τ represents the viscous stress tensor.

$$\tau = \left[\frac{-2}{3}\mu(\nabla \cdot \mathbf{V})\right]I + \mu\left[(\nabla\mathbf{V}) + (\nabla\mathbf{V})^{\mathrm{T}}\right] \qquad (2.33)$$

(iii) **Energy Equation**:

$$\frac{\partial\rho E}{\partial t} + \nabla \cdot [(\rho E)\mathbf{V}] = -\nabla \cdot (P\mathbf{V}) + \nabla \cdot (\tau \cdot \mathbf{V}) - \nabla \cdot \mathbf{Q} + S_E \qquad (2.34)$$

where S_E represents the energy source term due to the dispersed phase and E is the specific total energy. The heat conduction $\mathbf{Q}$ is modeled using Fourier's law

$$\mathbf{Q} = -\kappa\nabla T \qquad (2.35)$$

where κ is the thermal conductivity of the operating gas. For the sake of simplicity, the specific heats, thermal conductivity and viscosity were assumed to be constant for the present study.

2.3.2 Dispersed Solid Phase

The Lagrangian module of the solver has been used to model the solid dispersed phase. The equations are represented by,

(i) **Momentum Equation**

$$m_p \frac{d\mathbf{V}_p}{dt} = \mathbf{F}_p = \frac{\pi D_p^2}{8}\rho C_D |\mathbf{V} - \mathbf{V}_p|(\mathbf{V} - \mathbf{V}_p) \qquad (2.36)$$

C_D is modeled using an empirical expression obtained from the literature (Tedeschi et al., 1999). The model is valid across all rarefaction regimes and when $M_p <$

$1, Re_p < 200$. The momentum source term due to the particle drag force per unit volume is given by

$$\mathbf{S}_M = \frac{1}{vol_{\text{cell}}} \frac{3}{4} \Sigma_{N_p} \left[\frac{C_D Re_p m_p \mu}{\rho_p D_p^2} \right] (\mathbf{V}_p - \mathbf{V}) \qquad (2.37)$$

where vol_{cell} represents the cell volume.

(ii) **Energy Equation:**

$$m_p C_{p_p} \frac{dT_p}{dt} = h_p A_p (T_{aw} - T_p) \qquad (2.38)$$

where $A_p = \pi D_p^2$ is the surface area of the particle in contact with carrier phase and h_p is the convective heat transfer coefficient. It is estimated using the relation

$$h_p = \frac{(Nu_{ps})\kappa_s}{D_p} \qquad (2.39)$$

where κ_s is the thermal conductivity of the carrier gas estimated at the particle surface temperature T_{ps}, which is estimated using Eq. 2.40.

$$T_{ps} = T + 0.5(T_p - T) + 0.22(T_{aw} - T) \qquad (2.40)$$

The adiabatic wall temperature, T_{aw}, is obtained from the expression (Schetz and Bowersox, 2011)

$$T_{aw} = T + r \frac{V_r^2}{2C_p} \qquad (2.41)$$

$$r \approx Pr^{0.5} \qquad (2.42)$$

15

(Nu_{ps}) is estimated from an empirical expression obtained from Carlson and Hoglund (1964). The energy source, which is comprised of heat transfer and pressure work from the nanoparticles on the carrier phase is given by

$$S_E = \frac{-1}{vol_{\text{cell}}} \Sigma_{N_p} \left(m_p C_{p_p} \frac{dT_p}{dt} + \mathbf{F}_p \cdot \mathbf{V}_p \right) \tag{2.43}$$

where C_{p_p} represents the specific heat of the solid dispersed phase. The source terms $\mathbf{S}_M$ and S_E will be zero for flows with one-way coupling.

2.3.3 Solver Description and Discretization

The Eulerian part of the solver is adopted from rhoCentralFoam. RhoCentralFoam is a density-based compressible solver and utilizes the flux splitting KT (Kurganov and Tadmor, 2000) and KNP (Kurganov et al., 2001) schemes for interpolation. KT and KNP schemes are second order, semi-discrete, non-staggered, central-upwind schemes that are multi-dimensional and total variation diminishing (Greenshields et al., 2010). Initially, the convective derivatives and interpolated fluxes are determined at the current time step. Next, Eq. 2.31 is explicitly solved to estimate the density. The momentum equation is solved using a predictor-corrector algorithm. In the predictor step, the inviscid momentum equation is explicitly solved,

$$\left(\frac{\partial \rho \mathbf{V}'}{\partial t} \right)_I + \nabla \cdot \left[(\phi \mathbf{V}') \right] + \nabla P = 0 \tag{2.44}$$

Eq 2.44 is solved to obtain the inviscid flux $\phi = \rho \mathbf{V}'$ and the intermediate velocity is obtained by,

$$\mathbf{V}' = \phi / \rho \tag{2.45}$$

The final velocity is obtained by solving the corrector step,

$$\left(\frac{\partial \rho \mathbf{V}}{\partial t} \right)_V - \nabla \cdot (\mu \nabla \mathbf{V}) - \nabla \cdot T_{exp} = \mathbf{S}_M \tag{2.46}$$

where,

$$T_{exp} = \mu \left[(\nabla \mathbf{V})^T - \frac{2}{3} tr(\nabla \mathbf{V}) I \right] \tag{2.47}$$

The subscripts, I and V, represent the time-derivatives due to inviscid and viscous fluxes, respectively. The third term in the Eq. 2.46 is explicitly solved while the second term is solved implicitly. Eq. 2.46 can be simplified by substituting the following relation onto Eq. 2.47,

$$tr(\nabla \mathbf{V}) = \nabla \cdot \mathbf{V} \tag{2.48}$$

After further simplification, Eq. 2.46 becomes,

$$\left(\frac{\partial \rho \mathbf{V}}{\partial t} \right)_V - \nabla \cdot \tau = \mathbf{S}_M \tag{2.49}$$

The updated velocity from Eq. 2.46 is used to solve the predictor step of the energy equation,

$$\left(\frac{\partial \rho E'}{\partial t} \right)_I + \nabla \cdot \left[(\rho E' + P) \mathbf{V} \right] - \nabla \cdot (\tau \cdot \mathbf{V}) = 0 \tag{2.50}$$

Eq. 2.50 is solved explicitly to obtain the intermediate E'.

$$e' = \left(\frac{(\rho E')}{\rho} - \frac{|\mathbf{V}^2|}{2} \right) \tag{2.51}$$

The corrector step of the algorithm incorporates the diffusion and energy sources terms to determine the temperature,

$$\left(\frac{\partial \rho C_v T}{\partial t} \right)_V - \nabla \cdot \mathbf{Q} = S_E \tag{2.52}$$

The Lagrangian parcel fields are injected/initialized/evaluated once the function parcel *evolve* is called. The particle momentum and energy equations are solved by splitting the Eulerian time step Δt into multiple Lagrangian time steps for each particle (Δt_l),

$$\Delta x_l = min \left[(|\mathbf{V}_p| \Delta t), (CFL_l \Delta x_{cell}) \right] \tag{2.53}$$

$$\Delta t_l = \frac{\Delta x_l}{\mid \mathbf{V}_p \mid} \qquad (2.54)$$

where CFL_l represents the maximum Lagrangian Courant number. Δt_l is further divided if the particle crosses a cell face and enters another.

The particle momentum and energy equations are solved semi-implicitly. The drag force and heat transfer terms are estimated explicitly while the particle velocity and temperature are estimated using the Euler scheme (Ripplinger, 2013). The gas carrier phase velocity and temperature are obtained from the Eqs. 2.44 and 2.50. The properties are then interpolated from volume center to the particle position.

$$\mathbf{V}_p^{t+dt} = \frac{\mathbf{V}_p^t + \alpha\beta\Delta t_l}{1 + \beta\Delta t_l} \qquad (2.55)$$

$$\alpha = \mathbf{V}_{inp}^{\prime t} \qquad (2.56)$$

where $\mathbf{V}_{inp}^{\prime t}$ represents the interpolated gas velocity.

$$\beta = \frac{3}{4}\frac{m_p C_D Re_p \mu}{\rho_p D_p^2} \qquad (2.57)$$

The particle temperature is obtained by,

$$T_p^{t+dt} = \frac{T_p^t + \alpha'\beta'\Delta t_l}{1 + \beta'\Delta t_l} \qquad (2.58)$$

$$\alpha' = \left(T_{aw}^{\prime t}\right)_{inp} \qquad (2.59)$$

where $T_{inp}^{\prime t}$ represents the interpolated gas temperature.

$$\beta' = \frac{6h_p}{\rho_p C_{p_p} D_p (T_{aw}^t - T_p^t)} \qquad (2.60)$$

OpenFOAM offers three interpolation functions to convert the Eulerian fields to point Lagrangian source terms. These are *Cell*, *CellPoint* and *CellPointFace* interpolation. The *Cell* interpolates the nearest cell values onto the parcel positions. The *CellPoint* breaks each face down to

18

triangles. These triangles are used to define the tetrahedra and cell centre-point. The algorithm determines the location of the point through these tetrahedra and uses inverse distance weight functions to perform linear interpolation. The *CellPointFace* interpolation determines the point location nearest to the cell face. The point values are obtained through a linear interpolation of the corresponding face. In the present study, the *CellPoint* interpolation was used. It was found to provide an accurate interpolation of fields without much compromise in the computational cost.

2.4   Code Verification

The present study uses OpenFOAM, a widely used open source finite volume CFD framework based on the standard template library feature of C++. In OpenFOAM, the code and software quality is established through functional (FQ) and structural quality (SQ) assessments. FQ is achieved by verifying each individual functions of the solver and by testing the solver's capability of solving the problem as a whole unit. SQ refers to the assessment of complex attributes like maintennability, reliability and efficiency. There are some notable studies on verification and validation (V&V) of OpenFOAM solvers (Arisman et al., 2015; Greenshields et al., 2010; Hinman and Johansen, 2016b; Jagannathan et al., 2019a; Jagannathan and Johansen, 2019; Jasak, 1996; Persson, 2017). Greenshields et al. (2010) verified rhoCentralFoam for the 1D shocktube case and the supersonic flow over a forward-facing step problem. In the same study, rhoCentralFoam was validated against experimental data for a supersonic jet and a hypersonic flow over a bi-conic wedge. Arisman et al. (2015) performed V&V using FLUENT simulations and velocimetry data, respectively, for hypersonic flows over a flate plate. Hinman and Johansen (2016b) conducted V&V for the hypersonic blunt body problem. Recent studies have performed V&V across supersonic intakes for the E-L solver used in the present study (Jagannathan et al., 2019a; Jagannathan and Johansen, 2019).

Case	Grid cells	r	Δx (m)	Δt (s)
1	2×10^4	32	1.02×10^{-3}	6.67×10^{-8}
2	8×10^4	16	5.07×10^{-4}	3.23×10^{-8}
3	3.2×10^5	8	2.53×10^{-4}	1.64×10^{-8}
4	1.28×10^6	4	1.26×10^{-4}	8.23×10^{-9}
5	5.12×10^6	2	6.32×10^{-5}	4.13×10^{-9}
6	2.048×10^7	1	3.16×10^{-5}	2.075×10^{-9}

Table 2.1: Verification test cases for the oblique-shock simulations at $D_p = 250$ nm

2.5 Oblique-Shock Test Case

2.5.1 Computational Domain and Boundary Conditions

The oblique-shock test cases, which involve the physics of nanoparticle intakes, are described in Table 2.1. Both Richardson and mixed polynomial extapolation methods utilize a 3-grid solution. The inlet flow conditions were selected to represent a vehicle intake at Mach 2.5 flight at an altitude of 30 km. This corresponds to a freestream pressure, $P_\infty = 1197$ Pa, and temperature, $T_\infty = 226.51$ K (data obtained from ISA), while solving for inter-phase heat transfer and drag. The chosen particles had a density $\rho_p = 1000$ kgm^{-3} and specific heat $C_{p_p} = 710$ Jkg^{-1}K^{-1}, which are representative of solid metallic fuels for alternate high propulsion systems. Intially, the particles were assumed to be in a dynamic and thermal equilibrium with the gas. The flow conditions and geometry are similar to those simulated in a related work on supersonic intakes with nanoparticle injection with two-way coupling, which are discussed in the subsequent chapters (Jagannathan et al., 2019a).

The CFD domain is shown in Figs. 2.1. A uniform grid was constructed in Pointwise. The wedge half-angle was $8°$ with an expected oblique shock angle of $30°$. Slip flow conditions were used for the wedge. An example of the flowfield and particle trajectory is shown in Fig. 2.1.

2.5.2 Results

Iterative Convergence Errors:

IC errors were monitored by controlling the residual tolerance and maximum iterations per time step. An array of 4 test cases was built by varying these parameters, as shown in Table 2.2. For
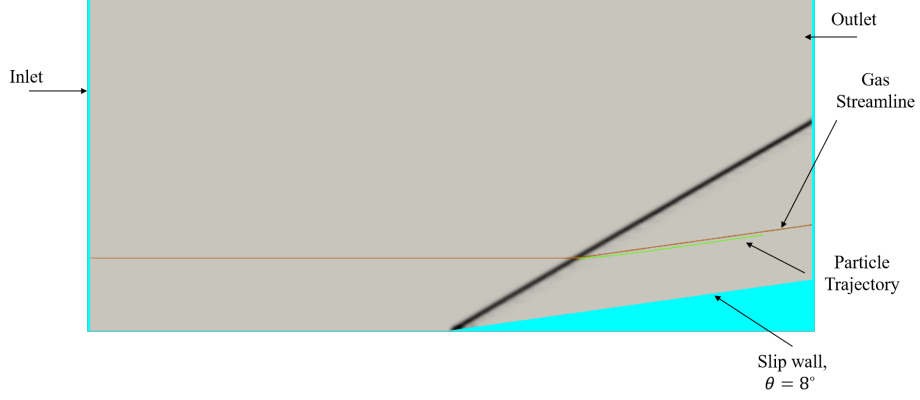
Figure 2.1: Synthetic schlieren and particle trajectory from the CFD solution of the oblique-shock case, $D_p = 250\,\text{nm}$

Case	Residual	Maximum iterations per time step	Relative Error (%)
1	10^{-10}	10^2	6.6×10^{-5}
2	10^{-12}	10^3	1.65×10^{-5}
3	10^{-14}	10^4	1.4×10^{-5}
4	10^{-16}	10^5	-

Table 2.2: Assessment of iterative convergence errors computed at $r = 32$

every subsequent test case, the residual tolerance was decreased by two orders of magnitude and the maximum number of iterations per time step was increased by an order of magnitude. Errors (in the velocity integrated across the domain area) due to iterative and grid convergence (GC) have been tabulated in Tables 2.2 and 2.3, respectively. Relative IC and GC errors are compared for the coarsest grid, $r = 32$, which are described by case-2 from Table 2.2 and case-1 from Table 2.3, respectively. The IC error for the coarsest grid was found to be smaller than the GC error by more than two orders of magnitude. Hence, IC errors can be neglected by using residual tolerances $< 10^{-10}$. Therefore, a uniform residual tolerance of 10^{-12} was used across all the simulations in this study.

Grid Convergence Error Analysis:

The y-particle velocity was identified to be the solution variable of interest for this analysis. The exact solution for this case was obtained using a 2D semi-analytical model. The following param-

Case	Refinement level (r)	Residual	Relative Error (%)
1	32	10^{-12}	2×10^{-3}
2	16	10^{-12}	1×10^{-3}
3	8	10^{-12}	6.5×10^{-4}
4	4	10^{-12}	3.4×10^{-4}
5	2	10^{-12}	1.7×10^{-4}
6	1	10^{-12}	-

Table 2.3: Relative errors due to grid convergence

eters were used for the analysis:

$$\delta_p = \frac{(\psi_p)_{\text{CFD}} - (\psi_p)_{\text{exact}}}{(\psi_p)_{\text{exact}}} \tag{2.61}$$

$$\ell^1 = \sum_{n=1}^{N} \frac{|(\psi_p)_{\text{CFD}} - (\psi_p)_{\text{exact}}| / (\psi_p)_{\text{exact}}}{N} \tag{2.62}$$

$$\ell^2 = \left(\sum_{n=1}^{N} \frac{|(\psi_p)_{\text{CFD}} - (\psi_p)_{\text{exact}}|^2 / (\psi_p)_{\text{exact}}^2}{N} \right)^{0.50} \tag{2.63}$$

where δ_p denotes the local discretization error, ℓ^1 and ℓ^2 represent the error norms (Roy, 2003).

$$\delta_{\text{ext}} = \sum_{n=1}^{N} \frac{|(\psi_p)_{\text{ext}} - (\psi_p)_{\text{exact}}| / (\psi_p)_{\text{exact}}}{N} \tag{2.64}$$

where δ_{ext} is the error due to the extrapolated solution and $(\psi_p)_{\text{ext}}$ represents the extrapolated solution variable.

Local GC errors were plotted at varying grid refinement levels in Fig. 2.2. The CFD solutions converged monotonically. The error norms were compared against varying grid refinement levels, as shown in Fig. 2.3. In addition to the IC errors being negligible, the solutions exhibited an asymptotic convergence, the combination of which ensures the validity of *a posteriori* extrapolation methods (Oberkampf and Trucano, 2002; Roache, 1998).

Extrapolation errors were compared for the mixed-order polynomial and generalized Richardson extrapolation, as shown in Fig. 2.4. The errors were computed at three refinement levels. For instance, δ_{ext} at $r = 1$ is computed using the CFD solutions at grid refinement levels of $r = 1, 2, 4$.
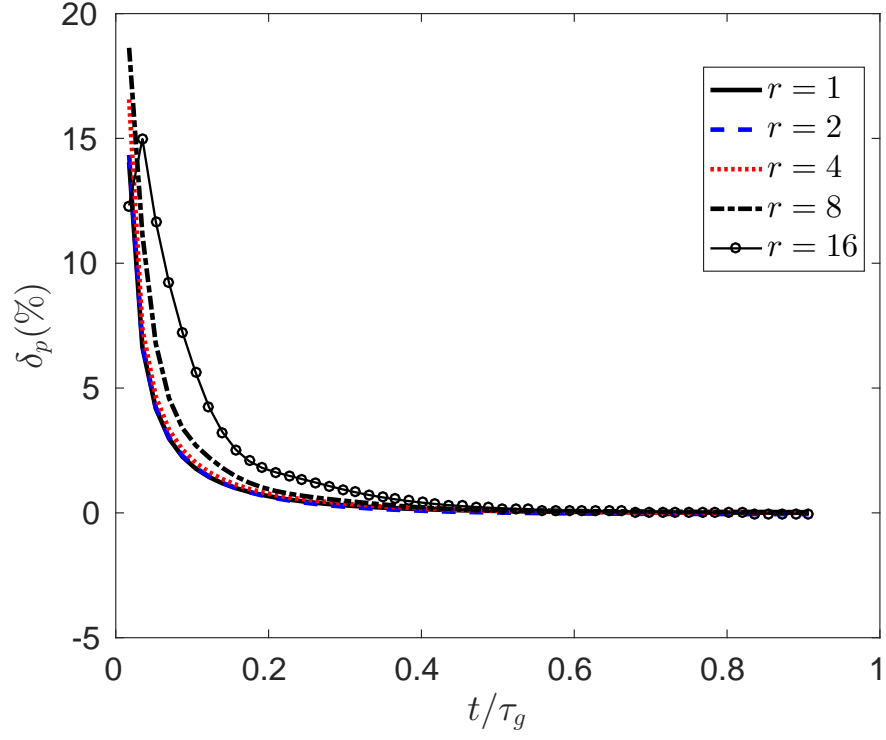
Figure 2.2: Local discretization errors in y-particle velocity in the post-oblique-shock region at varying grid refinement levels
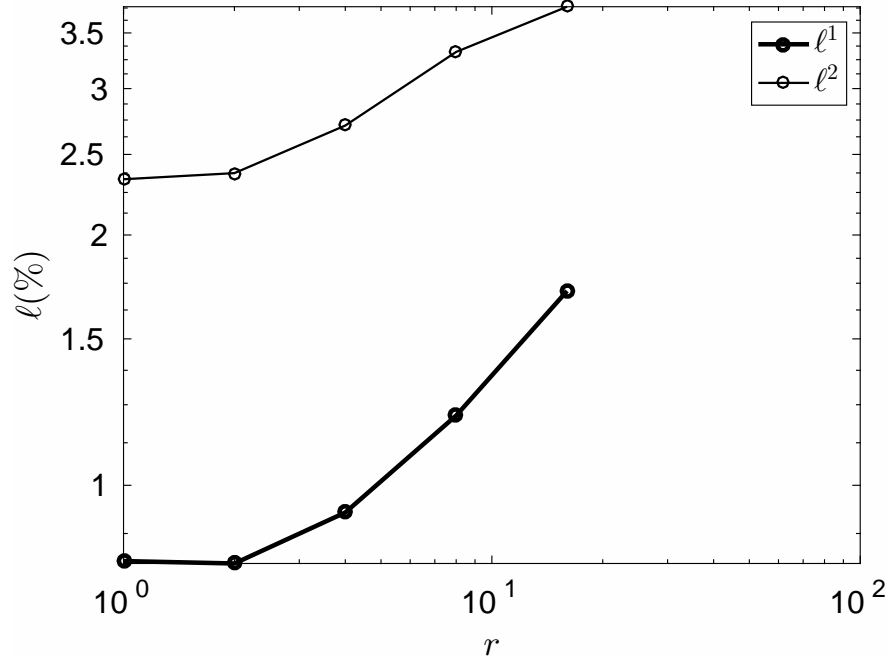
Figure 2.3: Error norms computed for y-particle velocity in the post-oblique-shock region at varying grid refinement levels

As expected, the accuracy of extrapolation increases with solutions computed from increasing grid refinement levels. The generalized Richardson method over-predicted the observed order of accuracy which is equal to 1.13 (computed using the grids at $r = 1, 2, 4$) while compared to the theoretical value of 1. At all three grid refinement levels, the mixed-order polynomial method provides a more accurate estimate of the exact solution.
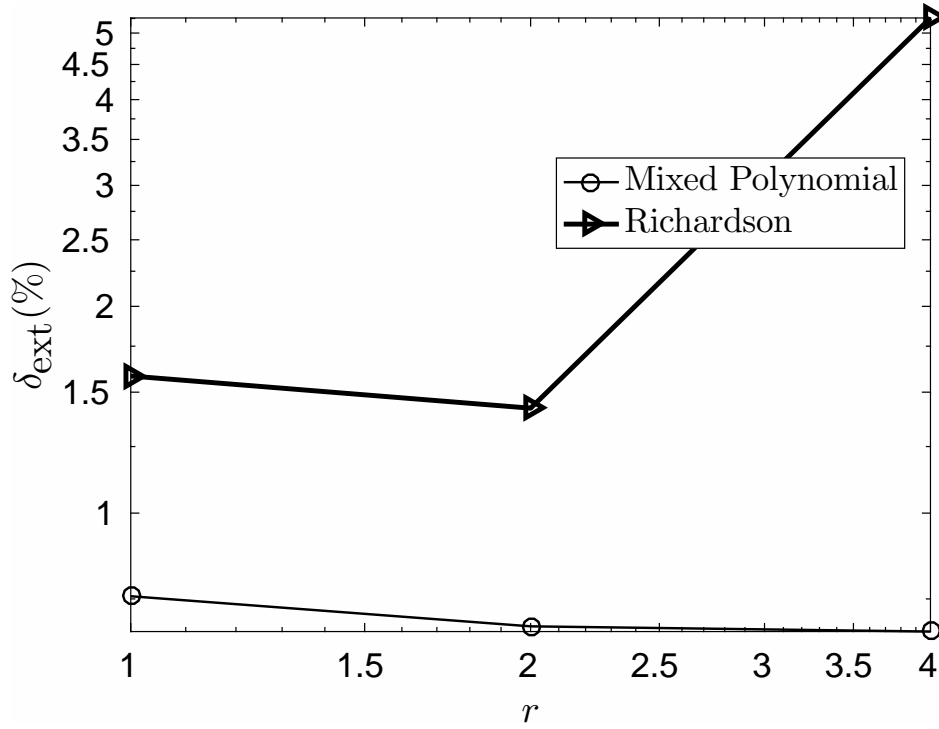
Figure 2.4: Extrapolation errors in y-particle velocity in the post-oblique-shock region at varying grid refinement levels

2.6 Diverging Duct Case

2.6.1 Computational Domain and Boundary Conditions

In this case, a single particle was injected into a supersonic flow across a diverging duct. The flow domain is shown in Fig. 2.5. A uniform grid was constructed in Pointwise. The duct had an area ratio of 3, inlet diameter (D) of 0.05 mm and length $L = 30D$. Similar to the previous test case, the inlet flow conditions were selected to represent Mach 2.5 at an altitude of 30 km with

Case	Grid cells	r	Δx (m)	Δt (s)
1	1.2×10^4	16	2×10^{-4}	1.32×10^{-8}
2	5×10^4	18	1×10^{-4}	6.62×10^{-9}
3	2×10^5	4	5×10^{-5}	3.31×10^{-9}
4	8×10^5	2	2.5×10^{-5}	1.66×10^{-9}
5	3.2×10^6	1	1.25×10^{-5}	8.28×10^{-10}
6	1.28×10^7	0.5	6.25×10^{-6}	4.14×10^{-10}

Table 2.4: Verification test cases for the diverging duct simulations at $D_p = 500\,\text{nm}$

freestream pressure $P_\infty = 1197\,\text{Pa}$, velocity, $V_\infty = 754\,\text{ms}^{-1}$, and temperature, $T_\infty = 226.51\,\text{K}$ (data obtained from ISA). The injection velocity and temperature of the particle were $754\,\text{ms}^{-1}$ and 280 K, respectively. A slip flow boundary condition was used for the walls. Simulation test cases are tabulated in Table 2.4. Five grids were used to investigate the convergence behavior. A highly refined solution (case-6 in Table 2.4) was approximated as the exact solution.
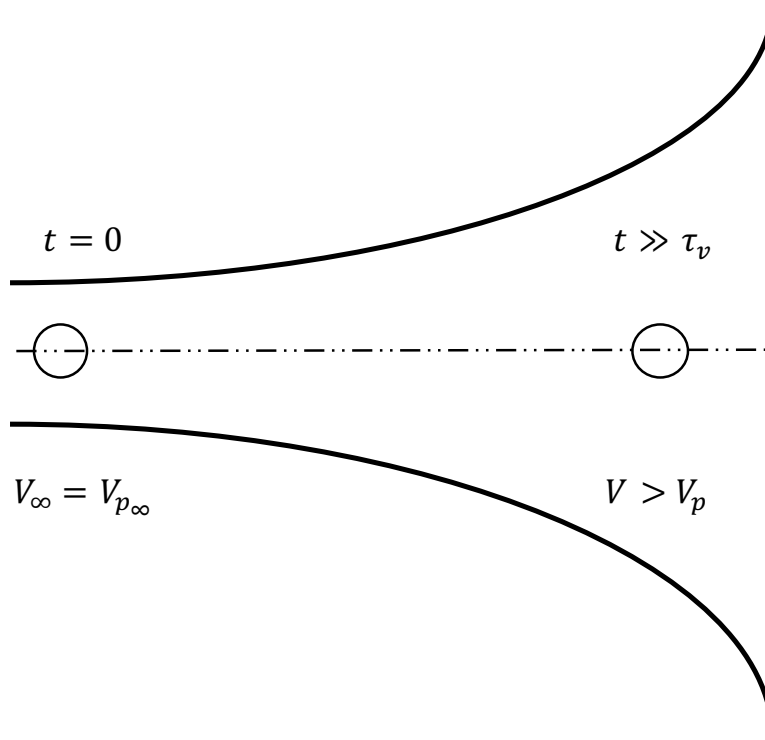
Figure 2.5: A single particle injected at the duct centre in a flow at $M_\infty = 2.5$

2.6.2 Results

IC errors were estimated using the same procedure as the oblique-shock test case and were found to be smaller than GC errors by at least two orders of magnitude. The same parameters (δ_p, ℓ and δ_{ext}) utilized in the previous case has been used here. The *x*-particle velocity was identified to be the solution variable of interest.
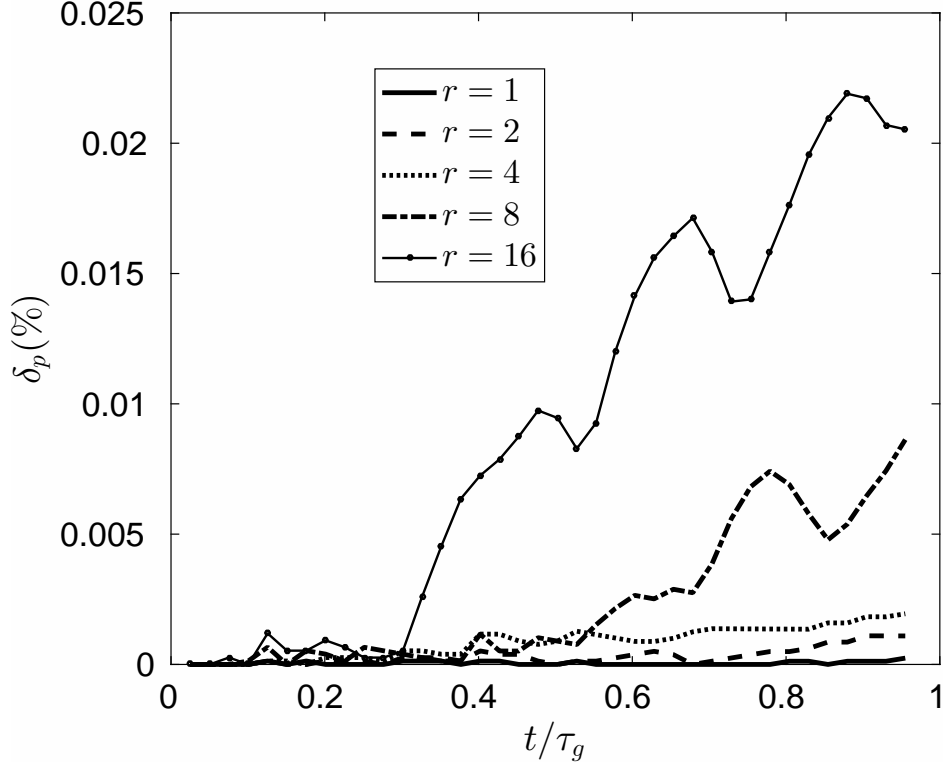
Figure 2.6: Local discretization errors in *x*-particle velocity across the diverging duct at varying grid refinement levels

The discretization error w.r.t time is plotted in Fig. 2.6 at different grid levels. The solution converges monotonically and the error propagates with particle motion. The error norms are shown in Fig. 2.7. The solutions lie in the asymptotic region, thus establishing the applicability of *a posteriori* extrapolation methods for the test case.

The two extrapolation methods are compared against each other in Fig. 2.8. It should be noted that while using the generalized Richardson method, a limit was imposed on the observed order of accuracy. This was $0.25 < p < 1$ (1 is the theoretical order of accuracy), which is based on
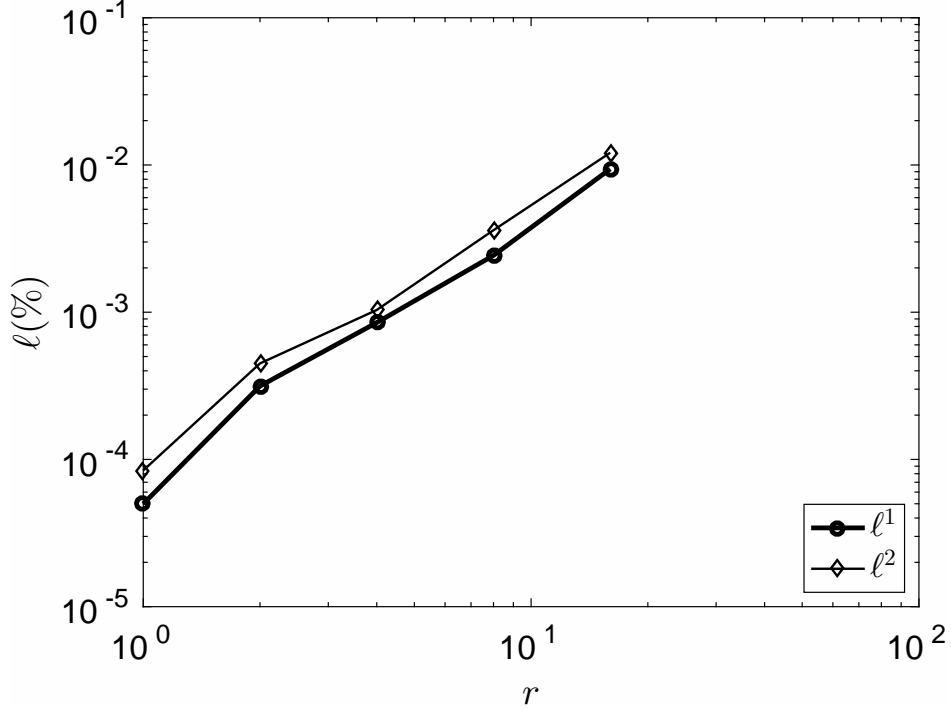
Figure 2.7: Error norms computed for *x*-particle velocity across the diverging duct at varying grid refinement levels

Oberkampf and Roy (2010). The generalized Richardson method was conservative in nature, with the mean observed order of accuracy of 0.25 (computed using the three most-refined grids). However, the mixed-polynomial extrapolation predicted a more accurate estimate of the exact solution. In addition, at coarser grids, the new method performed better than the Richardson method by an order of magnitude.

2.7   Discussion

A fundamental investigation into the solution verification of multiphase flows was conducted. Through a combination of *a priori* and *a posteriori* approaches, a new method to estimate the discretization errors for the dispersed phase variables was developed. This was tested against the generalized Richardson extrapolation using two test cases: supersonic flows through a compression ramp and diverging duct. The method, known as the mixed-polynomial extrapolation, was found to provide a more accurate estimate of the exact solution than the Richardson method. Fur-
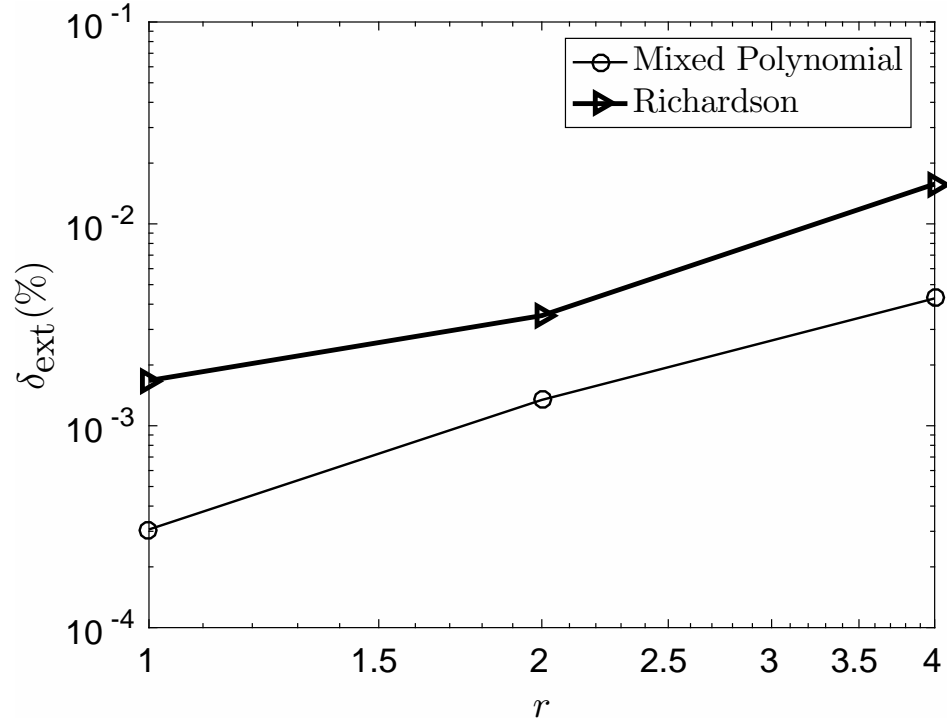
Figure 2.8: Extrapolation errors in *x*-particle velocity across the diverging duct at varying grid refinement levels

ther studies are required to test this method towards more complex flow modeling techniques such as two-way coupling.

Chapter 3

Performance Assessment of Supersonic and Hypersonic Intake Systems with Nanoparticle Injection

3.1 Introduction

Hypersonic air-breathing propulsion has been a major component of aerospace research since the 1950s, with possible applications in high-speed transport, space launch, and missile systems. More recently, it has been understood that hypersonic air-breathing propulsion technologies are fundamentally important to the advancement of aeronautical industries and to facilitate ease of access to space (Auslender et al., 2009; Flaherty et al., 2010; Smart and Tetlow, 2009). Intakes are a crucial component of high-speed airbreathing engines, as they are responsible for supplying high-pressure air to the engine for subsequent combustion and expansion - thereby generating thrust. Intake performance is assessed using parameters such as spillage drag and pressure recovery (Seddon and Goldsmith, 1999). Pressure losses in supersonic intakes are primarily caused by the presence of oblique and normal shockwaves. In addition to shockwaves, other aerodynamic features such as shockwave-boundary-layer interactions (SBLIs), wall friction, and flow separation can seriously decrease intake performance. A loss in stagnation pressure translates to a decrease in thrust (Heiser and Pratt, 1994). Hence, extensive efforts have been given to improve intake flow characteristics and pressure recovery. Many techniques have been employed to improve performance such as geometric optimization, variable-geometry intakes, flow control and cooling mechanisms (Seddon and Goldsmith, 1999). A brief overview of these techniques is presented here. Geometric optimization remains a key part of modern intake development and has been studied extensively in the literature (Brown et al., 2006; Carrier et al., 2001; Gaiddon and Knight, 2003; Gaiddon et al., 2004; Smart, 1999). A limitation of geometric optimization is that the intake design is typically only optimized

for a single flight speed or operating point. To address this, variable-geometry intakes have been developed (Curran, 2001; Dalle et al., 2011), but suffer from added complexity to the overall design and increased mass of the intake geometry (Billig, 1995). Thermal challenges associated with high gas temperatures experienced in supersonic engines have typically been dealt with using techniques such as regenerative, transpiration, ablation, radiation, and film cooling (Sutton and Biblarz, 2010). Among these techniques, the use of regenerative and film cooling are the most common (Chamberlain, 1992; Heufer and Olivier, 2006; Liu et al., 2012; Melis and Wang, 1999; Richards and Stollery, 1977). Film cooling involves the continuous injection of a secondary fluid through discrete slots that thermally insulates a wall or boundary from a supersonic gas stream (Eckert et al., 1966). This method benefits from its simple fabrication and light-weight nozzle assemblies compared to alternative approaches. However, this method suffers because of several complexities. For instance, the method requires a continuous supply of fluid to insulate the solid surface, which can be a difficult engineering problem (Kestin and Wood, 1970). Additionally, injection of a secondary fluid complicates flow development within the engine by introducing a source of turbulence, three dimensionality, separation, and mixing (Kestin and Wood, 1970). Some studies showed a decrease in pressure recovery as a result of film cooling (Zhang et al., 2014). Regenerative cooling is achieved by passing the cold propellant/oxidizer through tubes/channels/jacket around the combustion chamber/nozzle to cool the engine (Qin et al., 2009). In addition to the above methods, the supersonic flow stream can also be cooled prior to entering the engine using heat exchangers (Jivraj et al., 2007; Taguchi et al., 2015). This method has been shown to improve pressure recovery (Taguchi et al., 2015) and is currently being used in the development of Reaction Engines' Synergetic Airbreathing Rocket Engine (SABRE). Several flow control mechanisms have been employed to address the adverse effects of SBLIs. These include passive methods like bleeds (Delery, 1985; Fukuda et al., 1975; Harloff and Smith, 1996; Owens et al., 2008) and vortex generators (Blinde et al., 2009; McCormick, 1993), and active flow control mechanisms such as thermal bumps (Yan and Gaitonde, 2011; Yang et al., 2010), micro-air jets (Verma and Manisankar, 2012),

heat sources (Macheret et al., 2004; Soltani et al., 2011), magnetohydrodynamic and plasma actuators (Bobashev et al., 2005; Shang and Surzhikov, 2005; Shneider and Macheret, 2005; Zhao et al., 2014). Recently, solid nanoparticles have been shown to improve the characteristics of SB-LIs through momentum transfer between phases (Teh and Johansen, 2016). The extensive effort spent in improving intake performance is a clear illustration of its importance. To date, there has been no work attempting to use solid particle injection, specifically at the nano-scale, to improve intake performance.

Compressible gas-particle flows have been extensively studied for a wide array of applications such as inertial separators (de la Mora et al., 1990; Musgrove et al., 2009), cold sprays (Dykhuizen and Smith, 1998), fluidized beds (Deen et al., 2007), and solid rocker motors. Among them, there are several relevant studies analyzing fundamental nozzle flows and solid rocket motors (Amano et al., 2016; Carlson, 1965; Chang, 1980, 1983, 1990; Crowe and Willoughby, 1966; Daniel et al., 1994; Forde, 1986; Greenfield et al., 2011; Hoglund, 1962; Hwang and Chang, 1988; Jolgam et al., 2012; Lear and Sherif, 1997; Lear et al., 1997; Miller, 1975; Nishida and Ishimaru, 1990; Rudinger, 1970; Sherif et al., 1994; Vasenin et al., 1995; Yu and Liu, 2007; Zhang and Kim, 2018). Lear et al. (1997) developed 1D analytical solutions to study acceleration of gas-particle flows across a converging-diverging (C-D) nozzle, using velocity ratio, temperature ratio (relative to stagnation temperature), mass flow rate ratio, and specific heat ratio between the two phases as parameters. The study reported over 30% loss in the nozzle efficiency for some cases. A numerical study by Chang (1980) analyzed the effect of particle size (1-20 μm) and mass fraction (1-45%) for inviscid transonic gas-particle flows across the Jet Propulsion Laboratory (JPL) and Titan III nozzles. The study showed a decrease in gas velocities at smaller particle sizes and higher mass fraction. Nishida and Ishimaru (1990) used a time-dependent, total variation diminishing MacCormack method to assess steady, inviscid gas-particle flows across an axisymmetric JPL nozzle. The study reported an increased interaction between the two phases at higher mass loading ratios (at a particle diameter of 1 μm), and the presence of particle-free zones. Chang (1983) studied the effect of particle

size and gas specific heat ratio across a rounded square 3D supersonic nozzle, and showed considerable differences in the 3D flowfield when particle size was varied. A recent numerical study by Greenfield et al. (2011) analyzed the impact of particle size (0.1-3 μm) and mass loading ratio (1-100%) on the thrust production for viscous gas-droplet (liquid) flow across micro-nozzles. The study demonstrated a decrease in performance with particle size, showing $\sim 50\%$ reduction at the smallest size and highest mass loading ratio. Some studies have investigated the effect of gas-particle flows on normal shockwaves (Forde, 1986; Zhang and Kim, 2018). Forde (1986) used a time-dependent quasi 1D solution and Zhang and Kim (2018) used a viscous computational fluid dynamic (CFD) study to demonstrate a strong effect of particle mass loading on the location and strength of normal shockwaves formed in C-D nozzles. In an expansion nozzle, particles delay the gaseous expansion and heat the supersonic gas, thus decreasing the nozzle efficiency. On the other hand, if the gas-particle system were to be compressed, particles would cool the gas and add momentum to it, thus improving pressure recovery (Dass et al., 2017). From the literature, clearly, the fundamental aspects of gas-particle interaction in supersonic flows are understood. However, the extent to which particles and, in particular, nanoparticles can be used to improve intake flows has never been studied. For instance, while particle momentum and thermal inertia are known to reduce the efficiency of expansion nozzles, the extent to which these effects can be used in reverse to enhance an intake is unclear. Additionally, little advancement has been made to reduce the negative impact of shockwaves aside from manipulating intake geometries. Because of the high local particle lag associated with shock-wave particle interaction, the present study aims to show that particles can significantly reduce pressure losses associated with intake shock waves.

The idealized form of a supersonic intake is a one-dimensional C-D nozzle. Therefore, to illustrate the potential benefits of nanoparticles on intake performance, a parametric one-dimensional analysis of particle intake flows is presented here. One-dimensional supersonic compression processes across C-D intakes at idealized and single shock cases are used for the analysis. The peak potential of using nanoparticles in an intake is then demonstrated using the idealized compression

case. To better understand gas-particle interactions across an intake, specific parameters are derived from the basic governing equations. These are used throughout the work and are shown to effectively parameterize the problem. Predictions from the 1D model are then tested using CFD simulations of a supersonic particle laden flow through a more practical mixed-compression intake. Simulations are performed with, and without, particle injection using an unsteady compressible Eulerian-Lagrangian solver, developed in the OpenFOAM framework.

3.2 Inter-phase Modeling

It is necessary to determine which inter-phase momentum and energy transfer mechanisms will be significant in supersonic gas-particle flows through intakes. As such, simple order-of-magnitude and rate analyses were performed (refer to Appendix-A). Boron nanoparticles were chosen for analysis due to their high energy content and promise as a solid powdered fuel in high-speed air-breathing engines (Goroshin et al., 2001). A wide range of particle sizes ($500\,\text{nm} < D_p < 60\,\mu\text{m}$), intake Mach numbers ($2 < M_\infty < 5$), and flight altitudes ($\leq 30\,\text{km}$) were considered, albeit in non-dimensional forms discussed later.

3.2.1 Model Approximations

A particle dispersed in fluid flow typically interacts with the fluid through aerodynamic drag, Saffman and Magnus lift, thermophoresis, gravity, and unsteady forces (Fan and Zhu, 2005; Schwarzkopf et al., 2011). Unsteady force (Ling et al., 2011a,b, 2013; Tedeschi et al., 1992) and heat transfer (Ling et al., 2016) terms have shown to be negligible at low density ratios ($\rho/\rho_p << 1$). Boron particles are much denser than air ($\rho/\rho_p < 10^{-3}$ at sea level and $\rho/\rho_p < 10^{-4}$ at 30 km altitude). Hence, unsteady momentum and energy source terms were neglected. Li and Bai (2014) studied the effects of drag, Saffman lift, thermophoresis, and Brownian motion for particles/droplets moving through a supersonic boundary layer, and found the latter two force terms to be negligible. Williams (2015), using a time-scale analysis, assessed energy source terms for particles dispersed
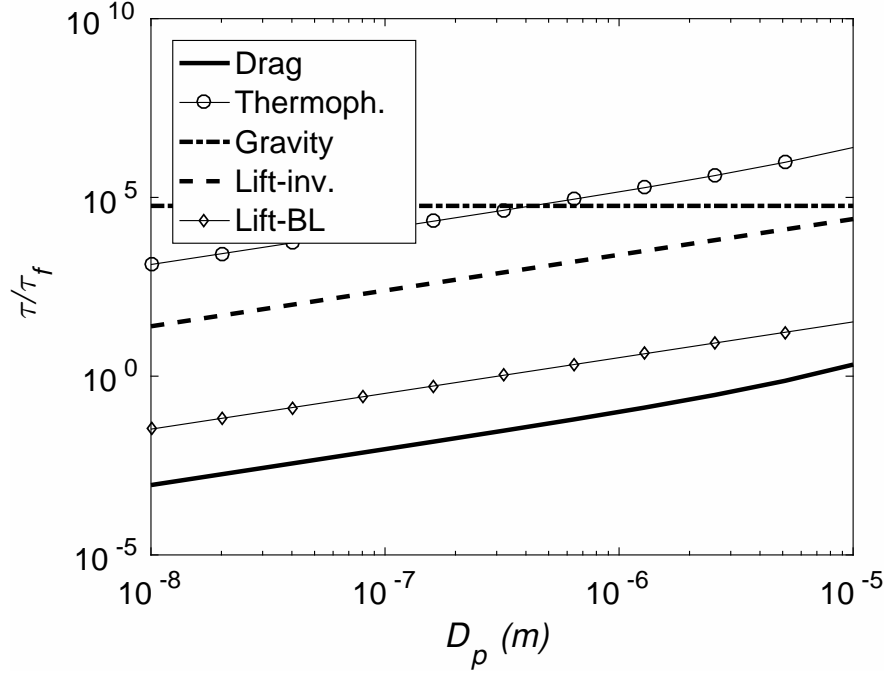
Figure 3.1: Time-scale comparisons between the drag, Saffman lift (at the inviscid region and boundary layers), thermophoretic and gravitational forces, when $M_\infty = 2.5$, $L \sim 1$ m and calculated using the conditions for an altitude of 30 km

in subsonic incompressible flows and found convection as the dominant source term for heat transfer. In the present study, a time-scale analysis was used to assess the momentum and heat source terms for compressible gas-particle flows through channels/nozzles. The analysis revealed aerodynamic drag and convection as dominant sources of momentum and heat transfer, respectively (as observed in Figs. 3.1 and 3.2). A detailed assessment of the time-scale analysis has been explained in Appendix-A.

Based on the above analysis, the following assumptions have been made to study supersonic gas nanoparticle flows: a) particles are incompressible; b) particles are spherical in shape; c) particles are modeled using a point-volume approach; d) temperature is uniformly distributed within the particles; e) effect of thermal radiation has been neglected; f) Saffman lift, thermophoretic, Magnus, gravitational and unsteady force terms have been neglected; g) chemical reactions and phase changes have been ignored; h) particle-spin has been neglected; and i) the gas-particle system assumes a two-way coupling ($\phi_p < 10^{-4}$).
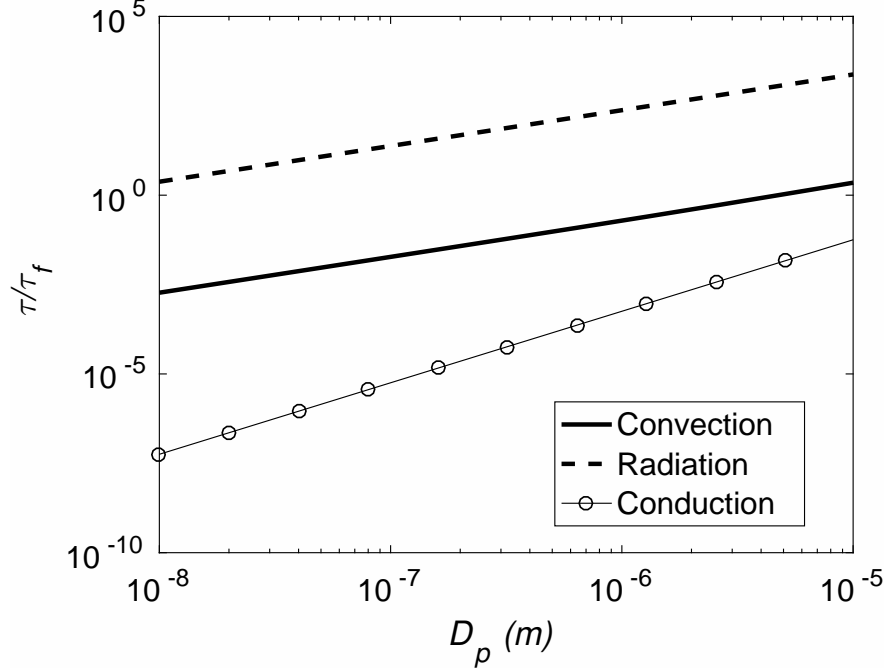
Figure 3.2: Thermal time constants of convection, radiation and internal conduction versus the gas flow timescale with particle diameter

3.2.2 Empirical Drag and Heat Transfer Models

The particle drag coefficient, C_D, and Nusselt number, Nu_p, are estimated using the empirically derived expressions from literature (Carlson and Hoglund, 1964; Tedeschi et al., 1999). The drag and heat transfer expressions account for compressibility and rarefaction. The aerodynamic drag coefficient, particle Knudsen number, and particle Mach number are given by Eqs. 3.1, 3.2, and 3.3, respectively.

$$C_D = \frac{24}{Re_p}k[1 + 0.15(kRe_p)^{0.687}]\xi(Kn_p)C \tag{3.1}$$

$$Kn_p = \frac{M_p}{Re_p}\left(\frac{\gamma\pi}{2}\right)^{0.50} \tag{3.2}$$

$$M_p = \frac{|\mathbf{V} - \mathbf{V}_p|}{(\gamma RT)^{0.5}} \tag{3.3}$$

where k is the Cunningham correction factor and C is the compressibility factor. The model is

extended to free molecular flows by incorporating the parameter, ξ. The model is valid across all rarefaction regimes and when $M_p < 1$ and $Re_p < 200$. The particle Nusselt number is described by the expression

$$(Nu_{ps}) = \frac{(Nu_{pc})}{1 + 3.42 M_{ps} \frac{(Nu_{pc})}{Pr_{ps} Re_{ps}}} \tag{3.4}$$

$$(Nu_{pc}) = 2 + 0.459 Re_{ps}^{0.55} Pr_{ps}^{0.33} \tag{3.5}$$

Eq. (3.5) represents the Nusselt number expression used for the continuum regime. The non-dimensional numbers, Re_{ps}, Pr_{ps}, and M_{ps} are estimated at the reference surface temperature T_{ps}, which is described by (Eckert, 1956)

$$T_{ps} = T + 0.5(T_p - T) + 0.22(T_{aw} - T) \tag{3.6}$$

The adiabatic wall temperature, T_{aw}, is obtained from the expression (Schetz and Bowersox, 2011)

$$T_{aw} = T + r\frac{V_r^2}{2C_p} \tag{3.7}$$

$$r \approx Pr^{0.5} \tag{3.8}$$

3.3 1D Analysis

As explained previously, a parametric assessment of particle injection across simplified intake geometries was conducted using a quasi-1D, compressible, gas-particle flow model.

3.3.1 Governing Equations

The governing equations of the quasi-1D gas-particle model are given by Eqs. 3.9-3.16 (refer to Appendix-B for derivation).

Gas Phase Continuity Equation

$$\frac{d(\rho A V)}{dx} = 0 \tag{3.9}$$

Gas Phase Momentum Equation:

$$\left(T_{\text{area}} + T_{\text{energy}} + T_{\text{drag}}\right) \left\{ \frac{M[2 + (\gamma - 1)M^2]}{2(1 - M^2)} \right\} = \frac{dM}{dx} \tag{3.10}$$

$$T_{\text{area}} = \frac{-1}{A} \frac{dA}{dx} \tag{3.11}$$

$$T_{\text{energy}} = \frac{1 + \gamma M^2}{2T_0} \frac{dT_0}{dx} \tag{3.12}$$

$$T_{\text{drag}} = \frac{S_{\text{L}} V}{R T_0} \left(1 + \frac{\gamma - 1}{2} M^2\right) \frac{dV_p}{dx} \tag{3.13}$$

T_{area}, T_{energy}, and T_{drag} represent the area (pressure) source term, energy source term, and aerodynamic drag term, respectively.

Gas Phase Energy equation:

$$C_{\text{p}} \frac{dT_0}{dx} = \frac{-6 S_{\text{L}} N u_{ps} \kappa_s}{\rho_p D_p^2 V} (T_{aw} - T_p) - S_{\text{L}} V_p \frac{dV_p}{dx} \tag{3.14}$$

Particle Momentum Equation:

$$C_{\text{D}} \frac{1}{2} \rho V_r \mid V_r \mid S_{\text{ref}} = m_p V \frac{dV_p}{dx} \tag{3.15}$$

Particle Thermal Energy Equation:

$$\frac{6 N u_{ps} \kappa_s (T_{aw} - T_p)}{\rho_p D_p^2 V} = C_{\text{p}p} \frac{dT_p}{dx} \tag{3.16}$$

C_{D} and Nu_{ps} were obtained using Eqs. 3.1 and 3.4, respectively. The governing equations were solved numerically using a fourth-order Runge-Kutta method.

3.3.2 Geometry and Case Setup

Based on an order of magnitude analysis, important particle parameters were identified as the Stokes number (Stk), thermal transport parameter (α_t), and particle Eckert number (Ec_p) (refer Appendix-C for derivation). The performance parameter, pressure recovery (π_c), is evaluated by varying the freestream Mach number and four particle parameters. The intake pressure recovery has been defined as the ratio of exit-to-freestream stagnation pressure. Inlet flow conditions were selected to represent a supersonic flow at an altitude of 30 km. This corresponds to a freestream pressure and temperature of 1197 Pa and 226.51 K, respectively. The density and specific heat capacity of Boron particles are $\rho_p = 2370\,\mathrm{kg\,m^{-3}}$, and $C_{pp} = 1026\,\mathrm{J\,kg^{-1}\,K^{-1}}$, respectively. The particle mass loading ratio was fixed at 0.11, assuming stoichiometric conditions at the combustor. The gas-particle system was investigated at two different operating conditions across a C-D intake.

The first operating condition represents an idealized, shockless compression process across the intake. An ideal case of compression is typically characterized by a converging-diverging geometry, with the flow achieving sonic conditions in the throat region. However, the throat conditions of a C-D intake were found to be affected by particle injection. Therefore, in addition to the five parameters described above, intake pressure recovery is also dependent on the intake geometry (Eq. 3.17). In the present study, the intake geometry is described using a simplified circular arc, which is symmetrical about the intake throat. The throat cross-section is defined by two conditions: $dA/dx = 0$ and $x = L/2$. By applying the above constraints, the optimized intake geometry is constructed by estimating the throat area ratio (Eq. 3.18).

$$(\pi_c) = f\left(Ec_p, \alpha_t, Stk, M_\infty, \frac{A_t}{A_\infty}\right) \tag{3.17}$$

$$\left(\frac{A_t}{A_\infty}\right)_{\text{gas/particle}} = \left(\frac{A^*}{A_\infty}\right)_{\text{gas/particle}} \tag{3.18}$$

The second case represents a super-critical flow condition, which incorporates two important physical effects encountered in intakes: an unoptimized geometry; and the presence of normal

shockwaves. Here, the geometry is fixed for every Mach number tested. The selected cross-section was marginally larger than the single-phase critical area to ensure super-critical conditions (refer Eq. 3.19). Here, the pressure recovery of the gas-particle system was dependent on five parameters, as described in Eq. 3.20. The shock strength was fixed, at $M_s = 1.95$, to produce a stable flow (shock formed in the diverging portion) within the range of parameters tested.

$$\left(\frac{A_t}{A_\infty}\right)_{\text{gas/particle}} = f(M_\infty) = \left[\left(\frac{A^*}{A_\infty}\right)_{\text{gas}} + \varepsilon\right] \tag{3.19}$$

where $0 < \varepsilon << 1$.

$$\pi_c = f(Ec_p, \alpha_t, Stk, M_\infty, M_s) \tag{3.20}$$

3.3.3 Idealized Compression through a C-D Intake

Effect of Heat Transfer:

In the case of idealized compression, pressure recovery for a single-phase flow (i.e. without particle injection) will be unity. Inter-phase heat transfer effects on pressure recovery are studied here by varying α_t. The results are shown in Fig. 3.3. The supersonic flow undergoes compression through the intake, which increases the static temperature and decreases the gas velocity. There are three observed outcomes with particle heat transfer: a) $\alpha_t \sim 1$; b) $0 < \alpha_t < 1$; c) $\alpha_t \sim 0$. Case(a) corresponds to a super-cooled stream of particles since the injection temperature approaches absolute zero. In this case, particles cool the gas during the entire flow (shown by the bottom curve in Fig. 3.4). This represents the maximum achievable performance through particle cooling. In case(b), the heat flow direction changes while it moves through the intake. Initially, the particles heat the gas when injected. The particles then begin to cool the gas after the system attains a momentary thermal equilibrium (shown by the top two curves in Fig. 3.4). At a given Mach number, pressure recovery increases (compared to the gas-only case) when there is a net heat energy transfer from the gas to particles, and decreases if the heat flow is reversed. The particle injection temperature

39
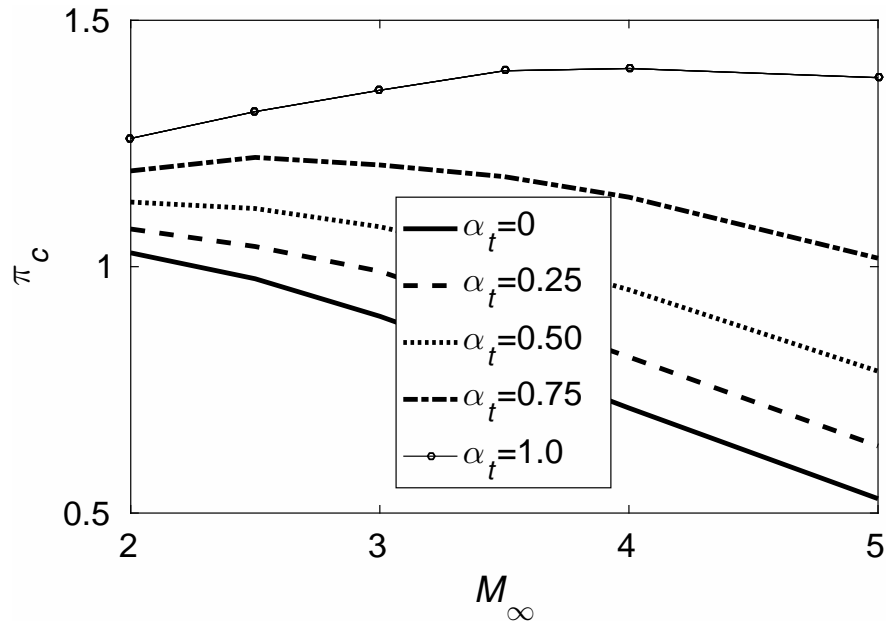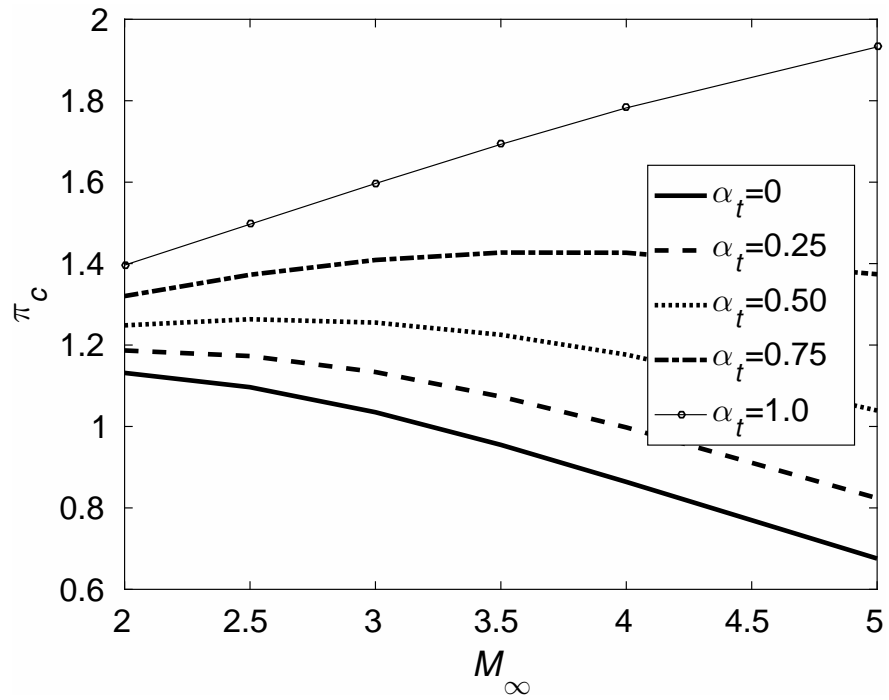
Figure 3.3: Stagnation pressure recovery against Mach number when α_t is varied, at $S_L = 0.11$, $Stk = 0.007$ and: a) $Ec_p = 0.5$; b) $Ec_p = 1$; and π_c for the gas-only case is 1
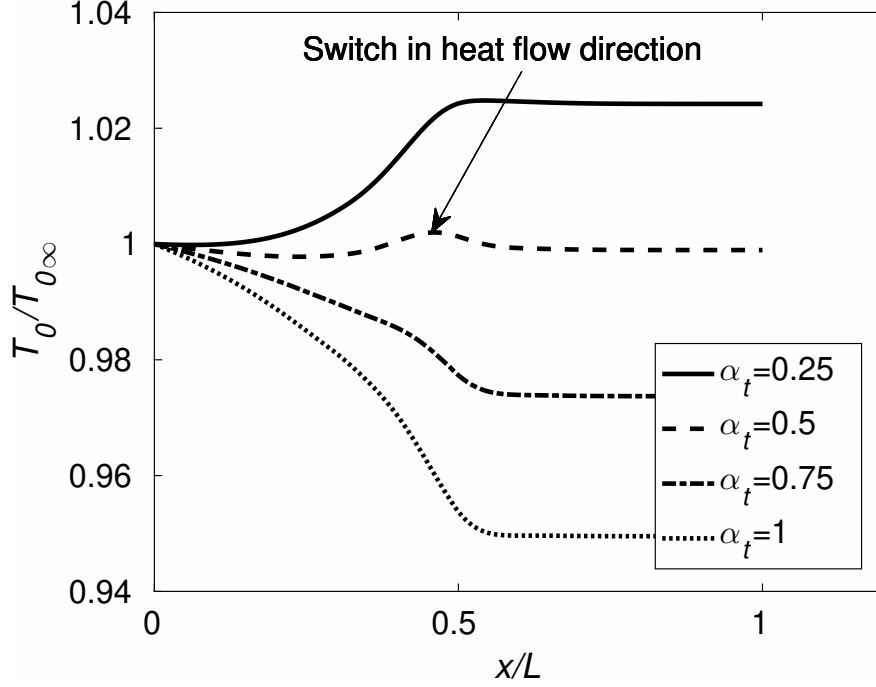
Figure 3.4: Stagnation temperature across the nozzle length when α_t is varied at $S_L = 0.11$, $Stk = 0.2$, $Ec_p = 1$ and $M_\infty = 4$

approaches the gas stagnation temperature in case(c). The heat energy transfers from the particles to gas throughout the compression process. This reduces pressure recovery. However, there is still a net gain in pressure recovery for $\alpha_t = 0$, when $M_\infty = 2$ (seen in Fig. 3.3). This is an effect of momentum transfer, which is discussed in the following section.

Effect of Momentum Transfer and Pressure Work:

Momentum and pressure work effects on pressure recovery are studied here by varying the particle Eckert number. The results are shown in Fig. 3.5. At a given Mach number, pressure recovery increases with Ec_p. There are two observed outcomes with particle advection in gas-nanoparticle flows: a) $Ec_p > Ec$; b) $0 \leq Ec_p < Ec$ (Ec is the Eckert number defined with gas velocity). Case(a) corresponds to a situation when particles are injected at velocities higher than the gas. In this case, the drag force on the gas acts in the flow direction throughout the compression process, and transfers momentum and pressure work to the gas (visually explained in Fig. 3.6(a) and demonstrated by the bottom curve in Fig. 3.7). This increases pressure recovery (also explains the anomaly
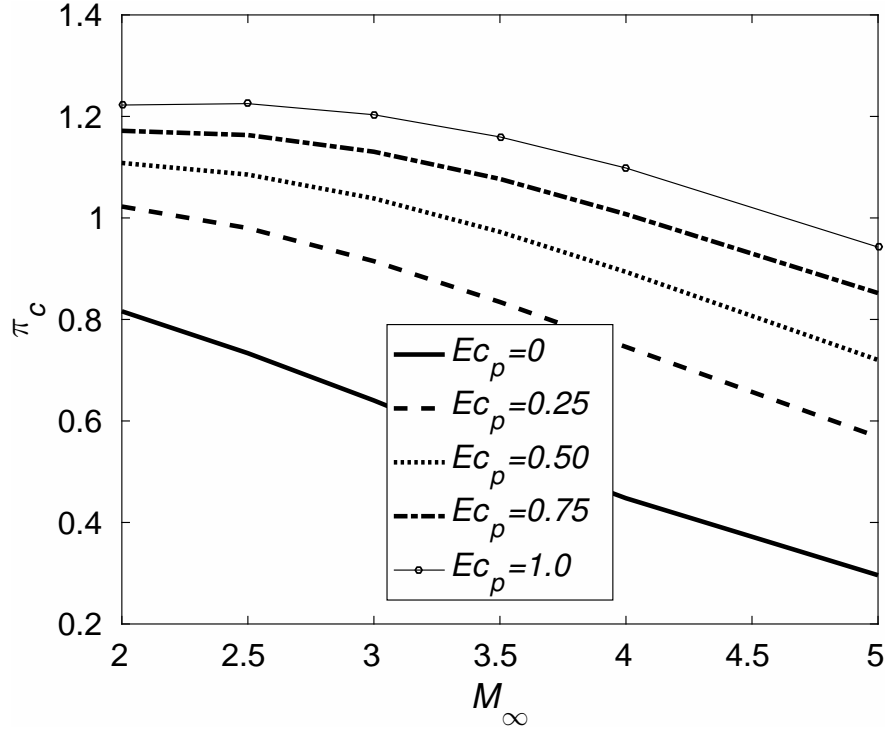
(a)
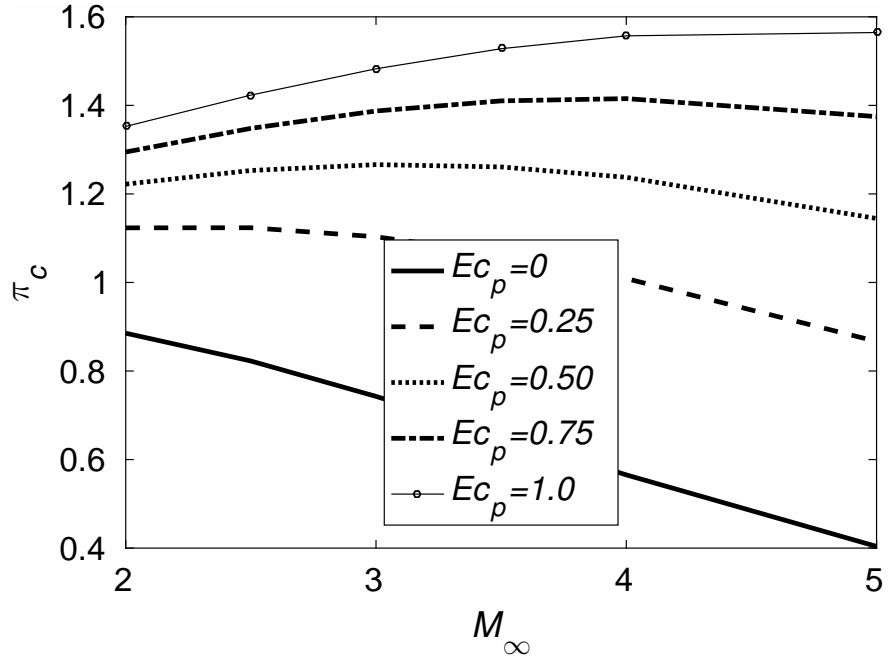
(b)

Figure 3.5: Stagnation pressure recovery against Mach number when Ec_p is varied, at $S_L = 0.11$, $Stk = 0.007$ and: a) $\alpha_t = 0.4$; b) $\alpha_t = 0.85$; and π_c for the gas-only case is 1

observed in Fig. 3.3(b), at $M_\infty = 2$ and $\alpha_t = 0$, where there is a gain in pressure recovery). For case(b), the particles are injected at a velocity lower than that of the gas. Initially, the drag force on the gas acts against the flow direction. This transfers momentum to the particles, and the particle velocity increases while the gas velocity decreases. The system reaches a momentary dynamic equilibrium inside the intake, but the gas velocity continues to decrease downstream because of the compression process. Particles transfer momentum to the gas beyond this equilibrium point (visually explained in Fig. 3.6(b) and demonstrated by the top two curves in Fig. 3.7). The point of momentary equilibrium moves downstream with a decrease in the injection velocity. Pressure recovery increases if there is a net transfer of momentum and pressure work to the gas, and decreases if the direction is reversed (compared to the gas-only case). Pressure recovery increases with Ec_p, but the gain in pressure recovery becomes larger with a higher value of α_t.

Effect of Particle Size:

Particle size effects are observed through the Stokes number, Stk, as shown in Fig. 3.8. Particle size primarily affects the rates of momentum and energy transfer between the phases. Rates of momentum and energy transfer increase with a decrease in particle size (seen in Fig. 3.8). Pressure recovery increases (at a given Mach number) when the momentum is added to the gas, or when the heat energy is removed from it (seen in Fig. 3.8(a)). Similarly, pressure recovery decreases (at a given Mach number) when momentum is removed from the gas, or when the heat energy is added to it (observed in Fig. 3.8(b)). Particle size has a greater effect at higher Mach numbers (larger gains in Fig. 3.8(a) and greater losses in Fig. 3.8(b)).

Based on the above discussions, it can be difficult to isolate the effects of inter-phase momentum and energy transfer on pressure recovery. Pressure recovery increases with cooling but also depends on the injection velocity (seen in Fig. 3.3). Similarly, pressure recovery improves when the particles add momentum and pressure work to the gas, but this also depends on the injection temperature (refer to Fig. 3.5). Rates of energy and momentum transfer increase when the particle size decreases. The net gain/loss in pressure recovery depends on a combination of α_t, Ec_p, Stk,
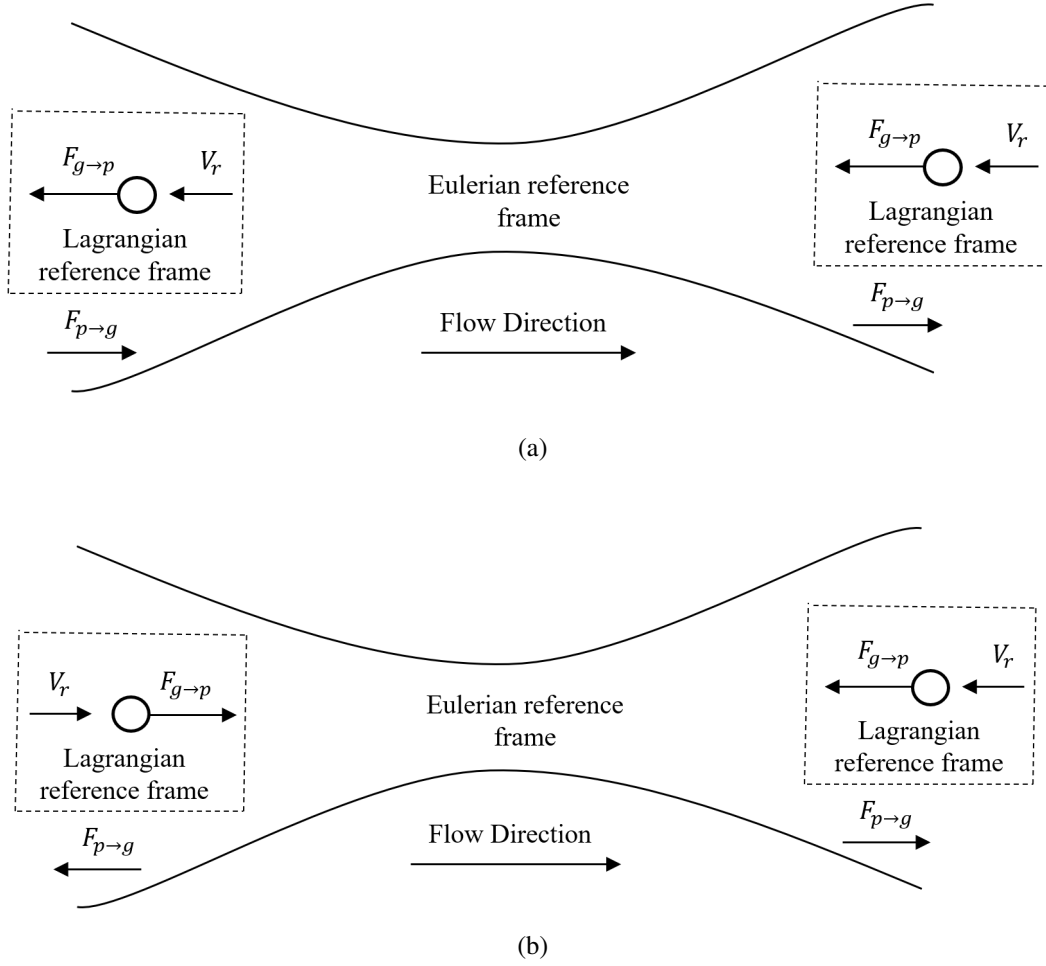
Figure 3.6: The direction of drag force by the particles on the gas, $F_{p \to g}$, for: a) $Ec_p > Ec$; b) $0 < Ec_p < Ec$
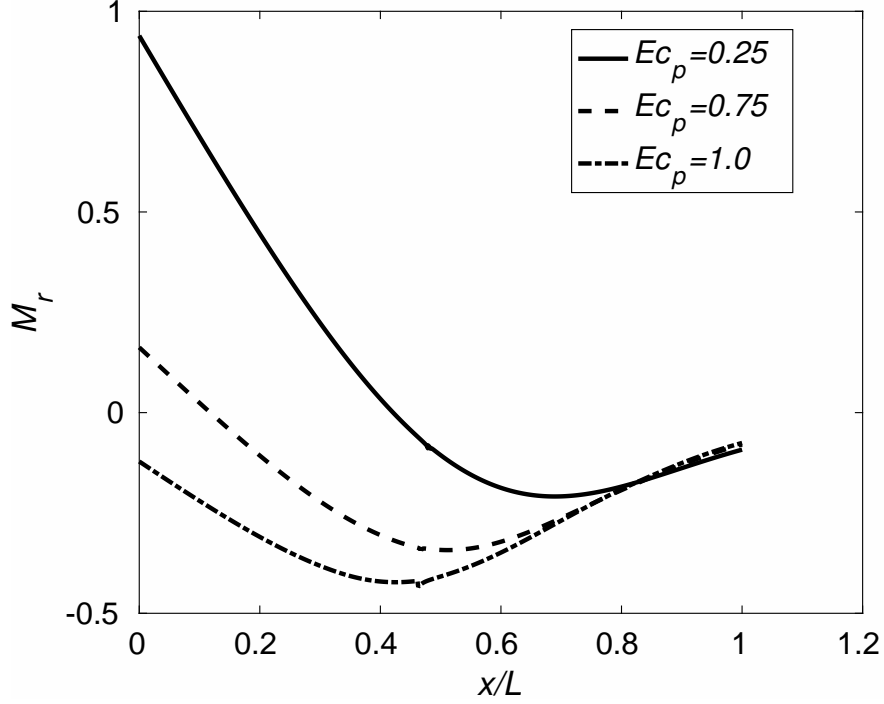
Figure 3.7: Relative Mach number, M_r, plotted along the nozzle length when Ec_p is varied, at $S_L = 0.11$, $M_\infty = 2$, $\alpha_t = 0.4$, $Stk = 0.2$

and M_∞. Overall, the net gain in pressure recovery becomes evident for $\alpha_t > 0.7$ and $Ec_p > 0.5$ at a Mach number of 5 and $Stk = 0.007$, and for $\alpha_t > 0.5$ and $Ec_p > 0.25$ at $M = 2.5$ and $Stk = 0.007$. Therefore, using nanoparticle injection to enhance intake performance is a complex, but solvable, optimization problem.

3.3.4   C-D Intake with a Normal Shockwave

The shock strength for this case was fixed at $M_s = 1.95$, resulting in a pressure recovery of 0.74 without particles. The results for the C-D intake with a standing normal shock wave are shown in Fig. 3.9. Similar to the previous case, pressure recovery increases with α_t and Ec_p. As mentioned above, this case represents a super-critical flow condition, with an unoptimized geometry and a strong normal shockwave. Even at these conditions, appreciable gains in pressure recovery are observed with particle injection. For instance, $\pi_c \sim 1.3$ when $\alpha_t = 1$ and $Ec_p = 1$, in contrast to the single-phase case, where $\pi_c = 0.74$, at a freestream Mach number of 5.
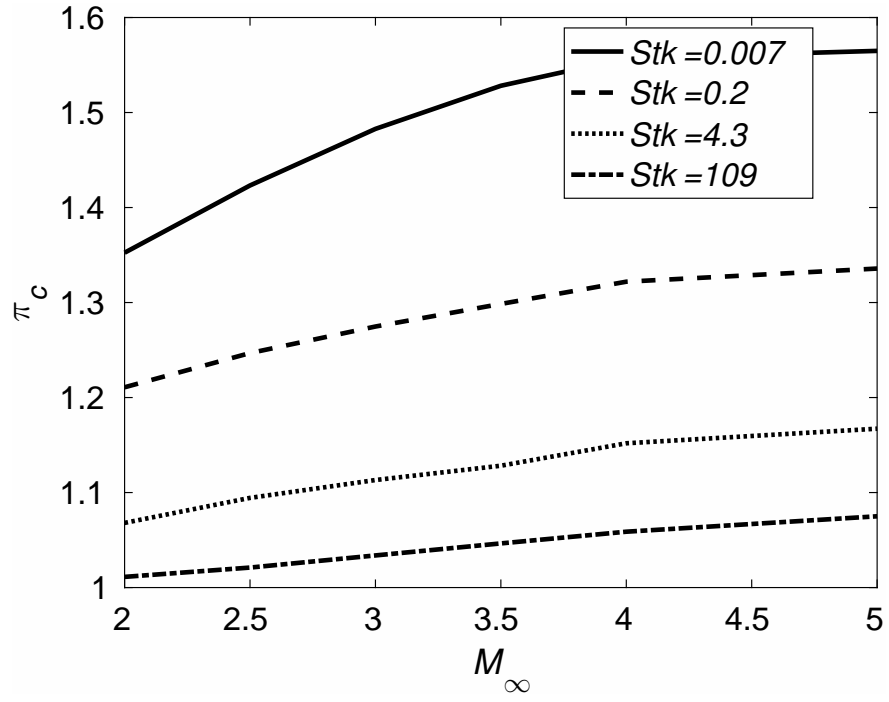
(a)
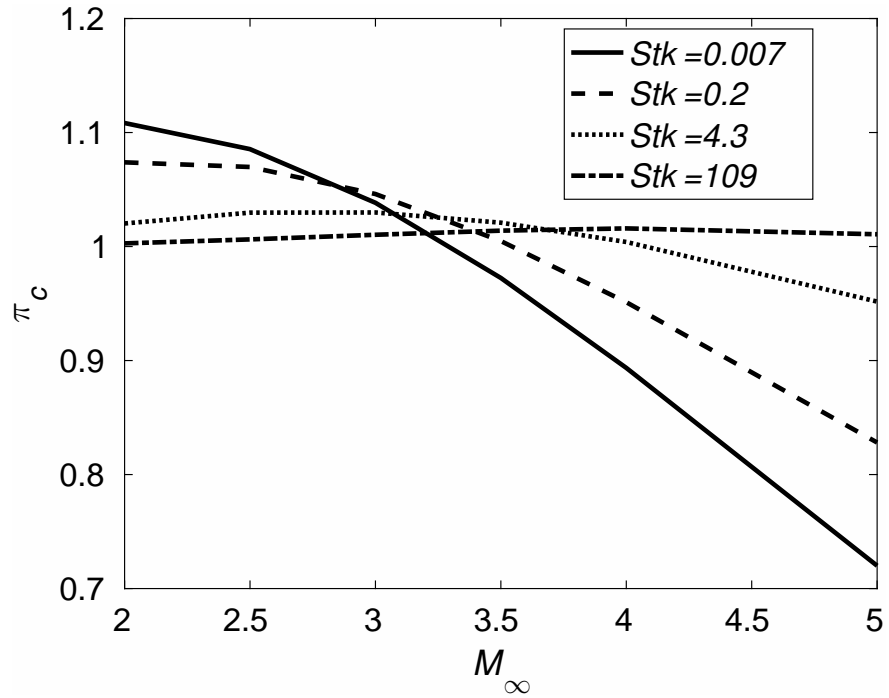
(b)

Figure 3.8: Effect of Stokes number on stagnation pressure recovery, at $S_{\mathrm{L}} = 0.11$ and: a) $Ec_p = 1$, $\alpha_{\mathrm{t}} = 0.85$; b) $Ec_p = 0.5$, $\alpha_{\mathrm{t}} = 0.4$
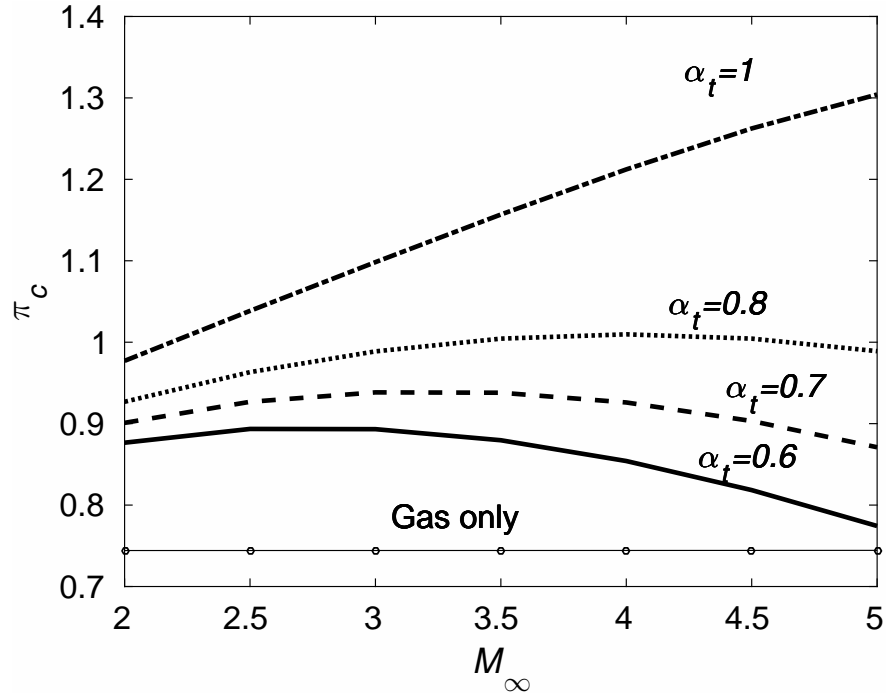
(a)
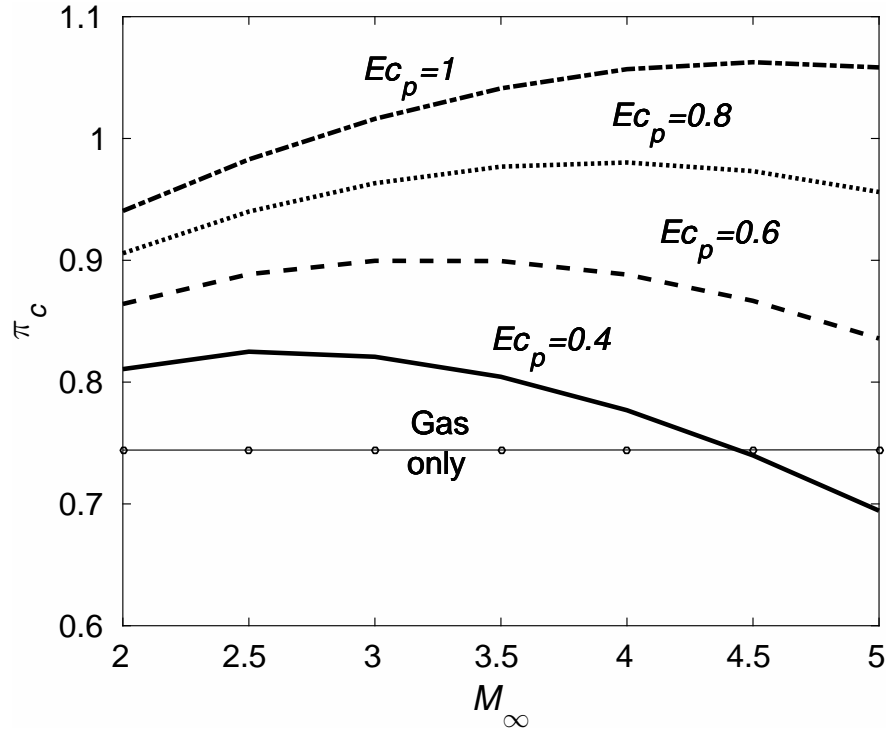
(b)

Figure 3.9: Effect of: a) particle heat transfer at $Ec_p = 1$; b) momentum and pressure work at $\alpha_t = 0.85$, against pressure recovery when $S_L = 0.11$, $M_s = 1.95$, and $Stk = 0.007$

Results from the 1D analysis illustrate considerable improvements in pressure recovery by injecting nanoparticles at favorable injection conditions. While the 1-D analyses described here are based on simplified conditions, which cannot be implemented in a practical intake configuration, insights gained are still useful in understanding the role that particle-gas interactions play in overall intake performance. Next, these observations are tested using a CFD analysis of a realistic intake configuration. A rectangular Mach-3 mixed-compression intake, with sufficient experimental data for validation (Anderson and Wong, 1970), has been chosen for the CFD study.

3.4   CFD Simulation of a 2D Mixed-Compression Mach 3 Intake with Particle Injection

3.4.1   Governing Equations and Solver Setup

CFD simulations were conducted using rhoCentralLPTFoam, a density-based compressible gas-particle solver. The solver is comprised of an Eulerian component (adapted from rhoCentralFoam (Greenshields et al., 2010)) that solves for the carrier gas phase, and a Lagrangian component (using OpenFOAM's built-in Lagrangian parcel tracking library) that solves for the dispersed solid phase. RhoCentralFoam is a decoupled explicit solver of the compressible Navier Stokes equations which uses Godunov-like KT and KNP schemes (Kurganov et al., 2001), that are total variation diminishing. It has been well verified and validated in the literature (Arisman et al., 2015; Greenshields et al., 2010; Hinman, 2017; Hinman and Johansen, 2016a,b; Jasak, 1996; Teh and Johansen, 2016). The Lagrangian component of the solver has recently been verified in the literature (Jagannathan et al., 2019b).

Carrier Gas Phase:

The carrier gas phase continuity, momentum and energy equations are described by

$$\frac{\partial \rho}{\partial t} + \nabla \cdot (\rho \mathbf{V}) = 0 \tag{3.21}$$

48

$$\frac{\partial \rho \mathbf{V}}{\partial t} + \nabla \cdot [(\rho \mathbf{V}) \mathbf{V}] = -\nabla P + \nabla \cdot \tau + \mathbf{S_M} \tag{3.22}$$

where $\mathbf{S_M}$ represents the momentum source term due to the dispersed phase

$$\tau = \left[\frac{-2}{3} \mu (\nabla \cdot \mathbf{V}) \right] I + \mu \left[(\nabla \mathbf{V}) + (\nabla \mathbf{V})^T \right] \tag{3.23}$$

$$\frac{\partial \rho E}{\partial t} + \nabla \cdot [(\rho E) \mathbf{V}] = -\nabla \cdot (P\mathbf{V}) + \nabla \cdot (\tau \cdot \mathbf{V}) - \nabla \cdot \mathbf{Q} + S_E \tag{3.24}$$

where S_E represents the energy source term due to the dispersed phase. The heat conduction $\mathbf{Q}$ is modeled using Fourier's law

$$\mathbf{Q} = -\kappa \nabla T \tag{3.25}$$

The specific heats, thermal conductivity, and viscosity were assumed to be constant for the present study, which correspond to a freestream temperature, $T_\infty = 338$ K, and Prandtl number, $Pr = 0.705$.

Dispersed Solid Phase:

The Lagrangian module of the solver has been used to model the solid dispersed phase. The particle momentum and energy equations are represented by

$$m_p \frac{d\mathbf{V}_p}{dt} = \mathbf{F}_p = \frac{\pi D_p^2}{8} \rho C_D |\mathbf{V} - \mathbf{V}_p| (\mathbf{V} - \mathbf{V}_p) \tag{3.26}$$

where C_D is modeled using Eq. 3.1. The model is valid across all rarefaction regimes and when $M_p < 1, Re_p < 200$. The momentum source term due to the particle drag force per unit volume is given by

$$\mathbf{S_M} = \frac{1}{v_{\text{cell}}} \frac{3}{4} \Sigma_{N_p} \left[\frac{C_D Re_p m_p \mu}{\rho_p D_p^2} \right] (\mathbf{V}_p - \mathbf{V}) \tag{3.27}$$

where v_{cell} represents the cell volume. The particle thermal energy equation is given as

$$m_p C_{\text{p}p} \frac{dT_p}{dt} = h_p A_p (T_{aw} - T_p) \qquad (3.28)$$

where A_p is the total surface area of a particle. The convective heat transfer coefficient, h_p, is estimated using the relation

$$h_p = \frac{(Nu_{ps})\kappa_s}{D_p} \qquad (3.29)$$

The energy source term due to the nanoparticles on the carrier phase is given by

$$S_{\text{E}} = \frac{-1}{v_{\text{cell}}} \Sigma_{N_p} \left(m_p C_{\text{p}p} \frac{dT_p}{dt} + \mathbf{F}_p \cdot \mathbf{V}_p \right) \qquad (3.30)$$

where the first and second terms in the bracket are the energy source terms from heat transfer and pressure work, respectively. The carrier phase continuity equation is solved explicitly, while the momentum and energy equations are solved semi-implicitly using a predictor-corrector algorithm. The discrete phase equations are solved semi-implicitly where: the drag coefficient/heat transfer coefficient is explicitly solved and the particle velocity/temperature is obtained using the Euler's implicit integration scheme.

3.4.2 Simulation Set-up

A rectangular Mach-3 mixed-compression intake (Anderson and Wong, 1970; Talcott and Kumar, 1985), tested for advanced supersonic aircraft, has been used to test the effect of particle injection. The intake geometry used here was taken from Anderson and Wong (1970). The computational domain and boundary conditions are described in Fig. 3.10. For simplicity, shockwave-boundary layer-particle interactions and other viscous effects are neglected by using a slip flow boundary condition at the walls. Freestream conditions were chosen at $M_\infty = 3$, $T_\infty = 338.7\,\text{K}$, and $P_\infty = 3914\,\text{Pa}$. The experimental study (Anderson and Wong, 1970) utilized bleeds to remove the boundary layer, and hence, was chosen to validate the present study. Outlet pressure was varied, for
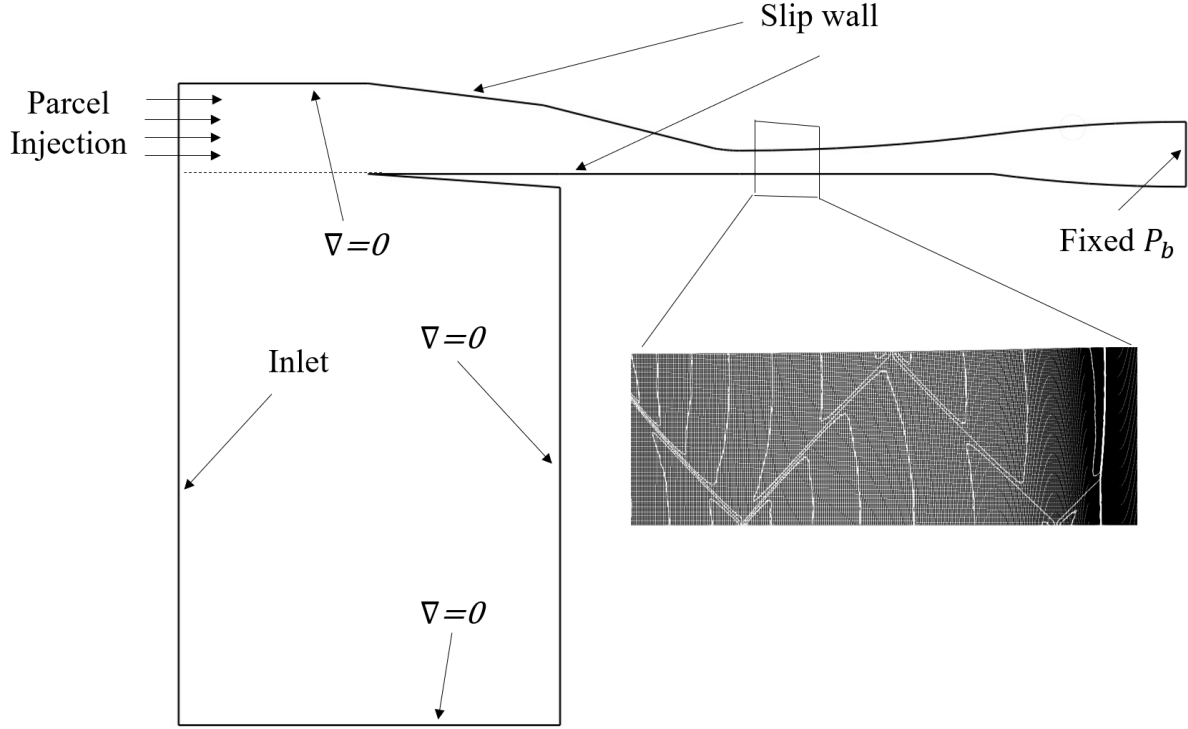
Figure 3.10: Domain boundary conditions and grid (coarse) resolution for the shock-train region shown using pressure-contour lines

single-phase and particle injection cases, to position the normal shockwave around the throat.

The freestream gas was seeded with particles from the inlet boundary. This setup represents an idealized injection condition. Injection temperature and velocity were chosen close to the freestream gas, to prevent any exchange in momentum/energy between the phases until after the first oblique shockwave. Parcel input parameters are tabulated in Table 3.1. The patch injection feature of OpenFOAM takes in total mass, injection duration, number of parcels per second, and particle size as inputs, and estimates the number of parcels to be injected at every time step. Parcels were injected from the cell centers of the indicated boundary (inlet). Although a significant number of parcels were introduced in the domain ($\sim 10^8$), they were orders of magnitude lower than the total number of particles ($\sim 10^{15}$). This introduces artificial unsteadiness, and must be considered in the interpretation of results.
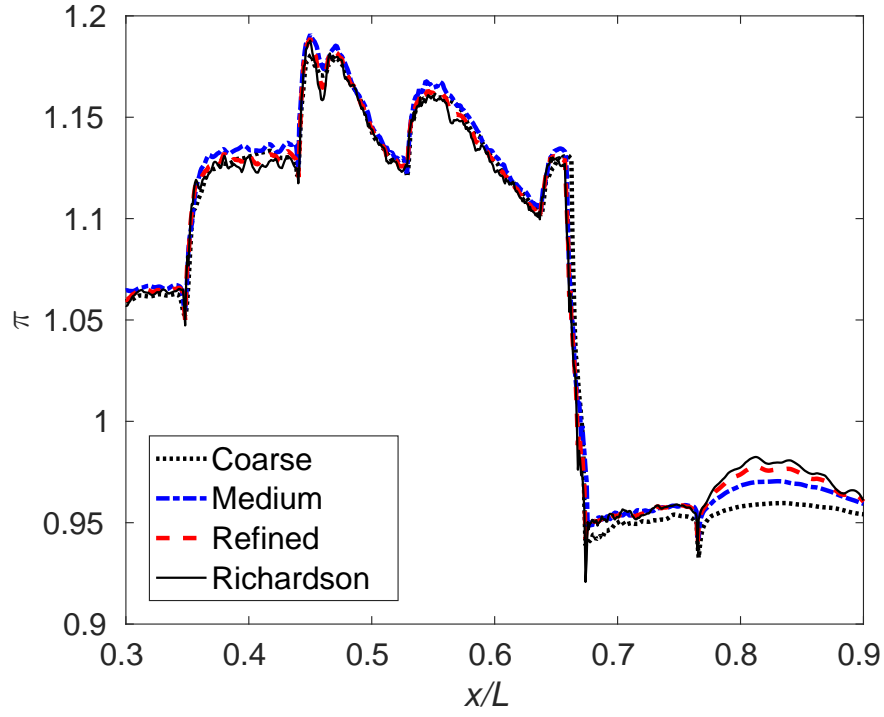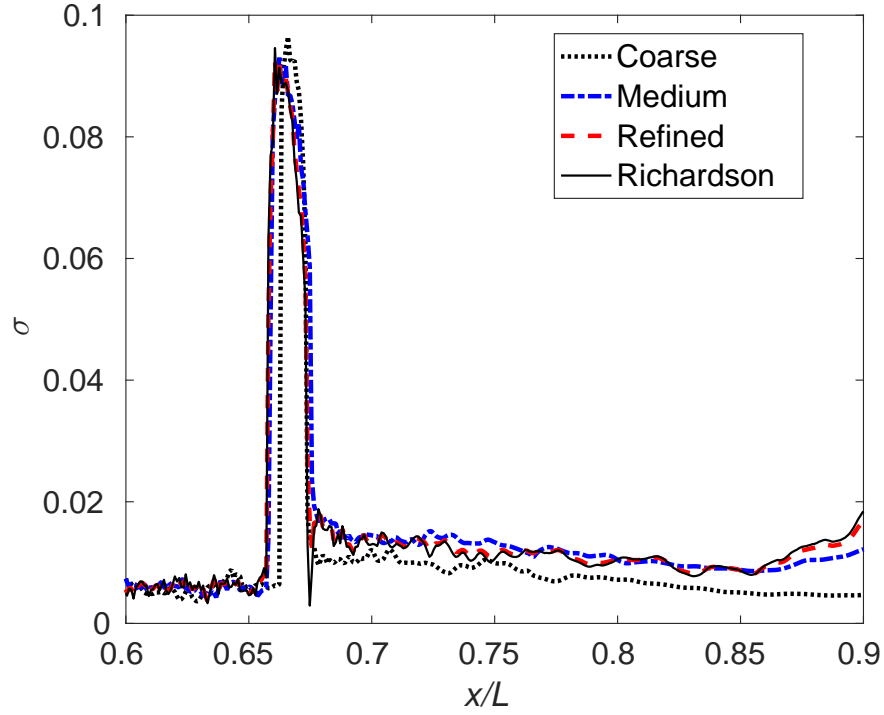
Figure 3.11: Plots of: a) time-averaged non-dimensionalized stagnation pressure; and b) standard deviation in π, against intake length, at $y/D = 0$, $P_{ex}/P_\infty = 32$, $S_L = 0.11$, $Stk = 0.0006$, $Ec_p = 1.25$, and $\alpha_t = 0.64$

Table 3.1: Parcel input properties

Inputs	Values
Parcels	$1 \times 10^8 \text{ s}^{-1}$
Mass flow rate	1.33 kg s^{-1} ($S_L = 0.11$)
Injection type	Patch
Injection face	Inlet
Injection temperature	330 K
Injection velocity	1100 m s^{-1}
Particle size	500 nm

Table 3.2: Grid convergence

Case	Cells	Parcels (s^{-1})	r
Coarse	7.5×10^4	0.5×10^8	4
Medium	3×10^5	1×10^8	2
Refine	1.2×10^6	2×10^8	1

3.4.3 Verification and Validation

Structured grids were created using the commercial software Pointwise. Grids were constructed to provide adequate resolution for shock capturing (observed in Fig. 3.10). To demonstrate convergence, refined grids were obtained by doubling the grid points (in every direction) and parcels w.r.t the reference grid, as tabulated in Table 4.2. Convergence behavior is assessed using the generalized Richardson extrapolation method (Roache, 1997). Grid convergence is demonstrated for averaged non-dimensionalized stagnation pressure in Fig. 3.11(a). The grid convergence index (GCI) for a medium-refine grid was between $0.000012\% < \text{GCI} < 2.81\%$, averaging at $\sim 0.19\%$, for pressure recovery. Convergence for artificial unsteadiness (as mentioned in the previous section) is demonstrated in Fig. 3.11(a). A physical form of unsteadiness (Seddon and Goldsmith, 1999), is also observed in the flow field when particles are injected (discussed in the next section). Therefore, time-averaged pressure recovery was used to investigate performance.

The boundary conditions and single-phase simulations of the CFD study are validated using the available experimental (Anderson and Wong, 1970) and simulation (Talcott and Kumar, 1985) data for the rectangular Mach-3 mixed-compression intake. To the author's knowledge, there were no relevant experiments/simulations to validate particle injection across an intake. However, the two-

phase CFD results matched with the predictions made on pressure recovery using the 1D analysis. Fig. 3.12 shows a comparison between CFD and experiment for the streamwise distribution of static pressure along the intake surface.
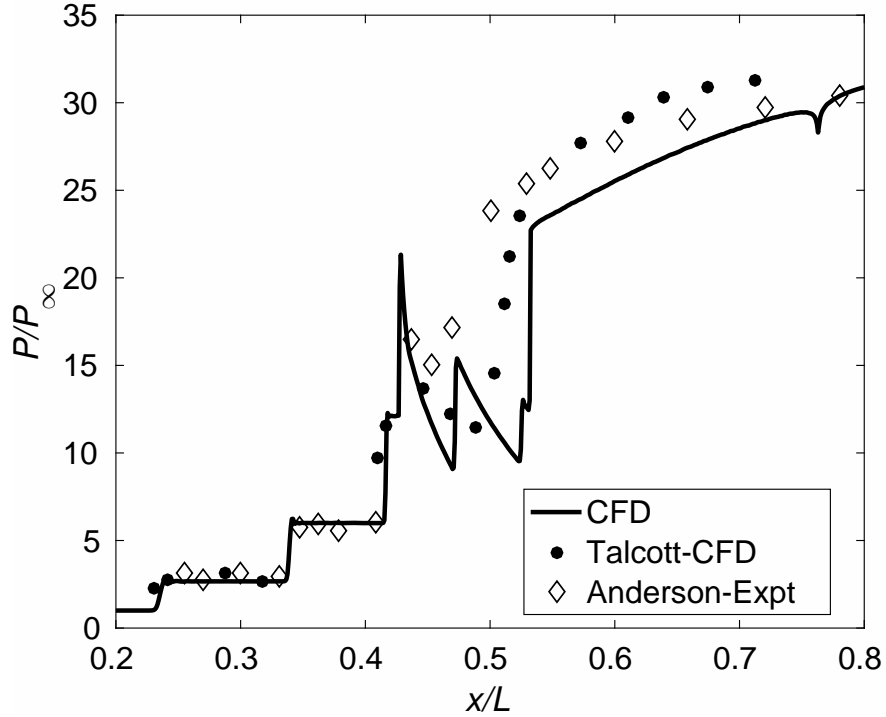
Figure 3.12: Validation of pressure ratio plotted along the cowl using data from Anderson and Wong (1970) and Talcott and Kumar (1985)

3.4.4 Results

Pressure recovery with, and without, particle injection is assessed at the condition of normal shockwave near the throat. This corresponds to the maximum achievable compression in the intake before unstart. A blue (minimum value) - red (maximum value) color scaling is used to interpret the CFD results. The supersonic flow encounters two oblique shockwaves generated by the compression ramps, a shockwave train formed around the throat region, and terminates with a normal shockwave, for both the cases.

The standard deviations in non-dimensionalized stagnation pressure (π) w.r.t. time, σ, is shown in Fig. 3.13 (showing the particle injection case at the top, and the single-phase case at the bot-
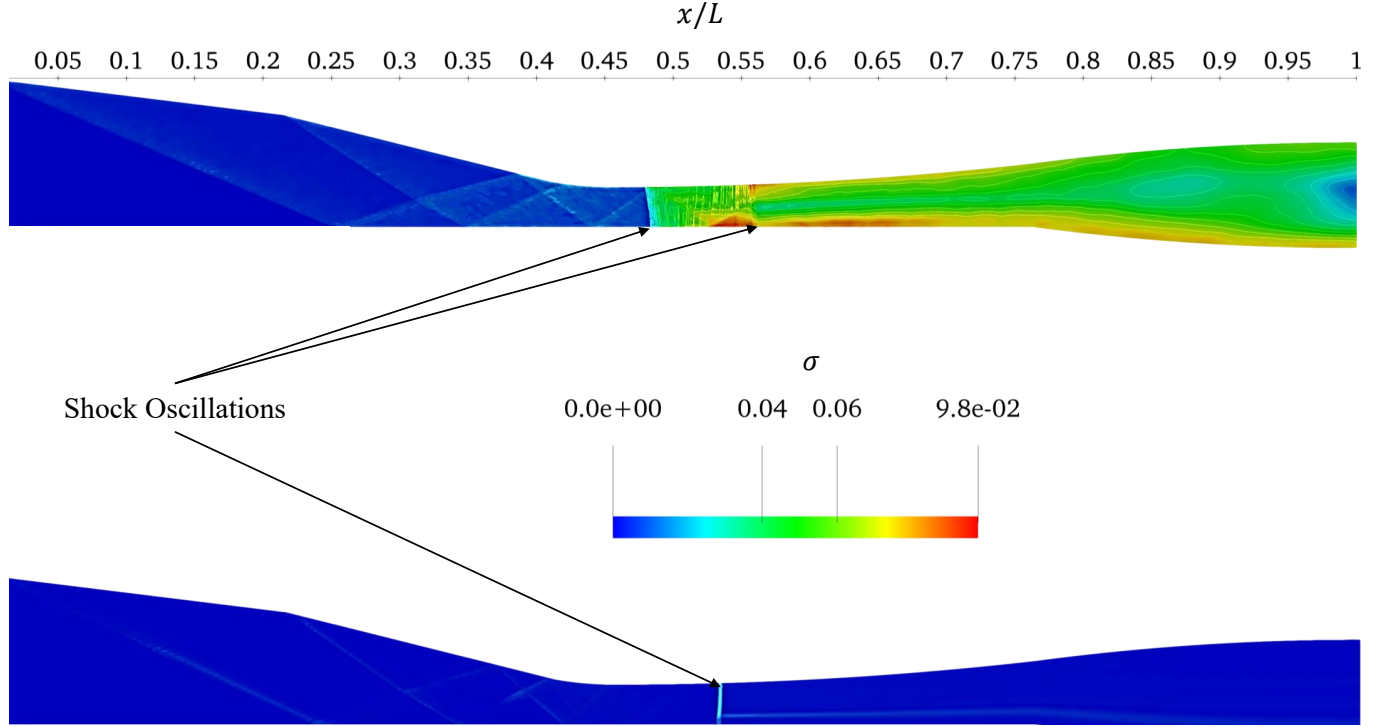
Figure 3.13: Standard deviations in π w.r.t. time: with (top) and without (bottom) particle injection, when $S_L = 0.11$, $Stk = 0.0006$, $Ec_p = 1.25$, and $\alpha_t = 0.64$

tom). For the particle injection case, σ is negligible in the domain up to $x/L \sim 0.47$, after which the effect of unsteadiness becomes appreciable. The vertical contour lines, observed in the region $0.47 < x/L < 0.55$, describe the motion of unsteady shock oscillations. On the other hand, shock oscillations for the single-phase case were negligible ($x/L \sim 0.54$), indicating steady state conditions.

The geometry and boundary conditions were chosen to achieve a critical/on-design intake performance for the single-phase case. As inferred from the 1D analysis, intake design conditions are changed when particles are injected. Therefore, the intake starts to operate at off-design conditions, resulting in shock oscillations. However, the amplitude of these oscillations are negligible when compared to the domain length (within 2.4% of the domain length, L). Unsteady variations in pressure recovery at the exit boundary were between 0-3%.

Contours of averaged π across the domain are shown in Fig. 3.14. π increases considerably through the shockwave train (for $0.2 < x/L < 0.6$) for the particle injection case (seen in (top)
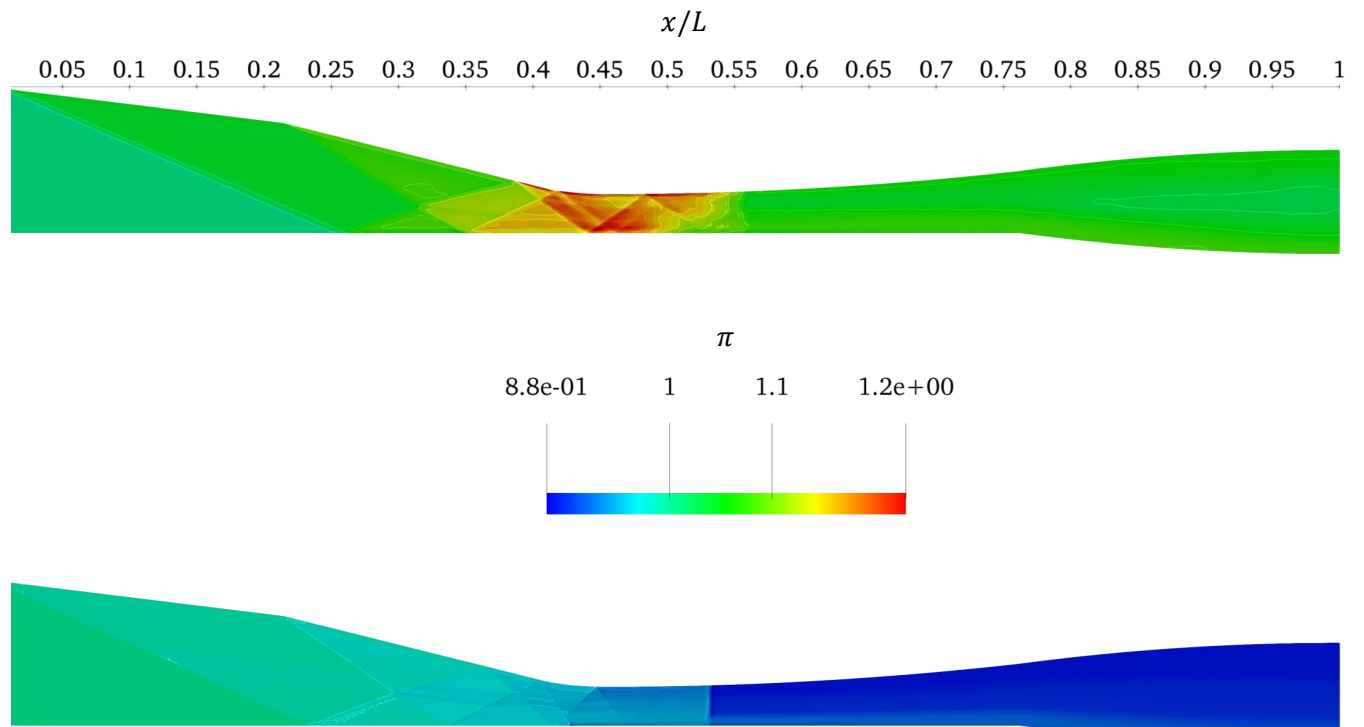
Figure 3.14: Averaged contours of non-dimensionalized stagnation pressure, π, across the intake: with (top) and without (bottom) particle injection, when $S_L = 0.11$, $Stk = 0.0006$, $Ec_p = 1.25$, and $\alpha_t = 0.64$

Fig. 3.14), while it decreases for the single-phase case. π decreases for both the cases across the normal shockwave. The flow downstream to the normal shockwave remains subsonic until the exit boundary. There is no appreciable change in pressure recovery during this region, for both the cases.

Gains in π from nanoparticle injection are further understood from the plots shown in Fig. 3.15(a), where the mean π is plotted along the intake length. As stated above, π for the particle-injection case increases whenever it encounters a shockwave, while it decreases for the single-phase case. This is because of the dynamic and thermal inertia of the particles. When the gas encounters a shockwave, there is an immediate increase in temperature and decrease in velocity. This sudden change decreases the stagnation pressure of the flow in the post-shock region (observed from the 'single-phase' curve in Fig. 3.15(a)). However, the particle variables do not immediately change across the shockwave. This establishes zones of dynamic and thermal non-equilibrium between the two-phases, in the immediate post-shock region. The heat energy transfers from the gas to particles, and the momentum and pressure work flow from the particles to gas, resulting in an increase of stagnation pressure (demonstrated in the above sub-sections 3.3.3 and 3.3.3). In a multi-shock system such as a mixed-compression intake, this state of non-equilibrium is established everytime the flow encounters a shockwave. In such cases, the pressure gain from the first shockwave is maximized if the particles attain momentum and thermal equilibrium before encountering the next shockwave. This is accomplished by injecting particles at a lower particle Stokes number or a smaller particle size (demonstrated in Fig. 3.15(a), where there is a near-instantaneous transfer of momentum and energy between the phases in the post-shock region at $Stk = 0.0006$).

CFD simulation of the mixed-compression intake is compared against the 1D solution obtained for a C-D intake with a standing normal shock formed near the throat, as seen in Fig. 3.15(b). The CFD results show a 16% increase in exit pressure recovery with particle injection while compared to a 22% increase observed from the 1D model. This is a first of its kind experiment/simulation showing a net gain in pressure recovery ($\pi_c = 1.04$). In a related experimental study, Perchonok
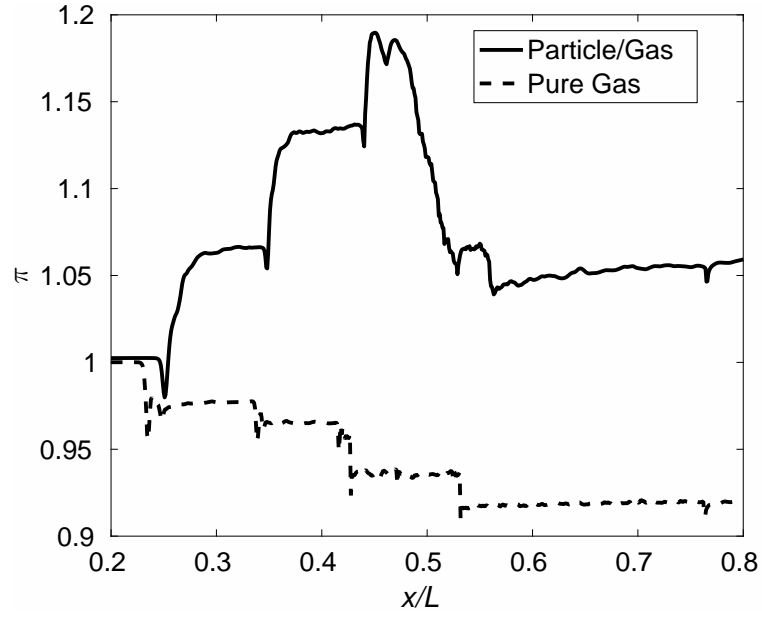
(a)
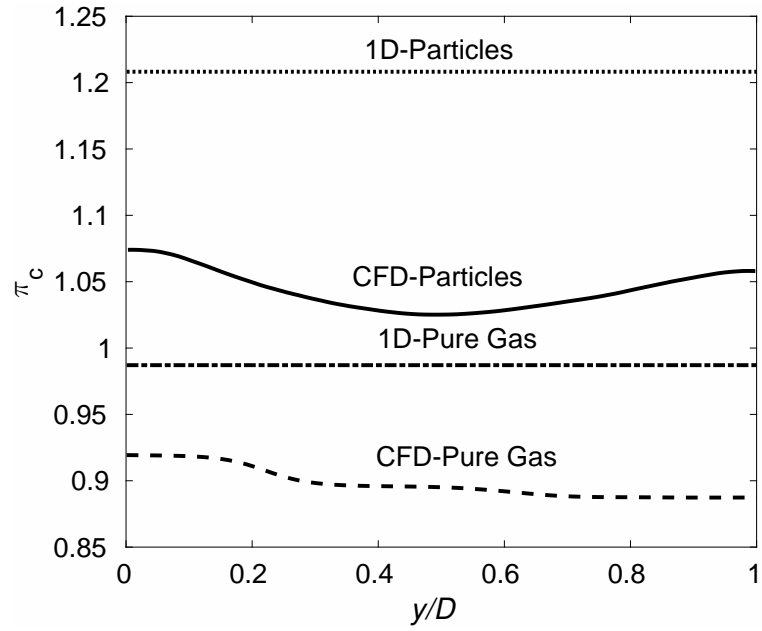
(b)

Figure 3.15: Plots of: a) π along the intake length at $y/D = 0$; and b) π_c along the exit cross-section for CFD and 1D solutions; when $S_L = 0.11$, $Stk = 0.0006$, $Ec_p = 1.25$, and $\alpha_t = 0.64$

and Wilcox (1956) observed a decrease in the intake pressure recovery with fluid injection. For instance, a 11% loss in pressure recovery was observed at a gas Mach number of 1.6, when the liquid (nitrogen) was injected at a Mach number of 0.4 and $S_L = 5\%$. Through the current CFD study, it was found that losses in pressure recovery could be mitigated through inter-phase heat transfer, even when particles are injected at the same or higher temperatures than the freestream gas, if injection velocity and particle size are favorable. In these cases, as the gas compresses and rises in temperature when moving through the intake, heat energy is transferred from the gas to particles, while momentum and pressure work is transferred from particles to the gas, both increasing the gas stagnation pressure.

3.5   Discussion

A novel approach to improve the performance of high-speed intake systems is demonstrated by injecting Boron nanoparticles. Through a 1D parametric analysis of converging-diverging intake, it was revealed that: a) there were considerable gains in pressure recovery with nanoparticle injection (in some cases $\pi_c > 1$) for idealized and single-shock compression cases; and b) these gains in pressure recovery were only achieved beyond a certain threshold combination of cooling (high α_t), injection velocity (high Ec_p), and particle size (low Stk). For instance, at a freestream Mach number of 5 ($V_\infty = 1508\,\mathrm{m\,s}^{-1}$) and particle size of $D_p = 500\,\mathrm{nm}$ ($Stk = 0.007$), gains in pressure recovery (idealized compression case) were observed for particle injection temperatures lower than 408 K ($\alpha_t > 0.7$) and velocities greater than $828\,\mathrm{m\,s}^{-1}$ ($Ec_p > 0.5$). CFD simulations conducted on a 2D mixed-compression Mach-3 intake predicted a 16% increase in exit pressure recovery with nanoparticle injection, which is consistent with the 22% gain from the 1D analysis. In a multi-shock mixed compression intake, momentum and energy exchanges between the two phases occur through dynamic and thermal non-equilibrium conditions established behind the shockwaves, resulting in the observed gains in pressure recovery.

Chapter 4

Stability Analysis of High-Speed Intakes with Nanoparticle Injection

4.1   Introduction

High-speed intakes/inlets are characterized by their ability to supply steady and uniform air flow rates with minimum pressure losses. However, unsteady intake flows are a common occurrence at sub-critical conditions (off-design Mach numbers or exit pressures). Intake stability is affected by two important flow characteristics: unstart and flow unsteadiness (i.e. intake buzz) (Curran, 2001; Curran and Murthy, 1991; Kantrowitz and Donaldson, 1945; Seddon and Goldsmith, 1999). Intake unstart/startability is characterized by isentropic and Kantrowitz operability limits (Curran, 2001). At a given Mach number, the isentropic limit is the maximum achievable contraction before unstart, and the Kantrowitz limit describes the minimum contraction required to self-start an intake (Kantrowitz and Donaldson, 1945). As an unsteady phenomenon, intake buzz could potentially result in thrust losses, combustion instability and even a complete engine breakdown (Seddon and Goldsmith, 1999). Intake buzz is a form of self-sustained flow oscillations through a closed feedback loop mechanism comprising of two important elements: a source of flow instability that gets convected downstream and an upstream-propagated pressure wave (Ho and Nosseir, 1981). Instabilities are generated either from the breakdown of vortex sheet entering the intake (formed due to normal-oblique shock interactions), known as the Ferri-type instability (Ferri and Nucci, 1951), or from the separation of boundary layer behind the normal shock, known as the Dailey-type instablility (Dailey, 1955). The upstream-propagated pressure waves are typically generated when the flow downstream gets choked, which is similar in principle to that of a jet impinging on the wall. Buzz oscillations are classified into *little-buzz* and *big-buzz* oscillations based on the

60

amplitude of oscillations. While the source of *little-buzz* oscillations have been attributed to both the Ferri-type (Ferri and Nucci, 1951) and Dailey-type (Chen et al., 2017) instabilities, *big-buzz* oscillations have been known to only be caused from the separation of boundary-layer at the ramp (Daines and Segal, 1998). During buzz, the intake oscillates between excessive and deficient mass flow rates compared to design conditions (Trapier et al., 2006).

There are several historical studies (Dailey, 1955; Ferri and Nucci, 1951; Fisher et al., 1970; Nagashima et al., 1972), as well as some recent works (as seen in Table 4.1), investigating the mechanism of intake buzz. The exact mechanism for intake buzz depends on a number of factors such as throttling ratio, freestream Mach number, Reynolds number, cross-sectional shape (rectangular or conical), the design of shock system, and characteristic length (Dailey, 1955; Ferri and Nucci, 1951; Herrmann et al., 2013; Lee et al., 2011; Lu and Jain, 1998; Trapier et al., 2008, 2007, 2006). As explained above, intake buzz comprises of an acoustic element in the form of upstream-propagated pressure waves, which are dependent on the characteristic length of the intake. For instance, *big-buzz* oscillations, with frequencies in the range of 252.2-444.7 Hz, were found for a Mach 2.5, rectangular, mixed-compression intake with a characteristic length of 0.11 m (Lee et al., 2011). However, big-buzz frequencies of 33-37 Hz were found for a similar shape (rectangular, Mach 2.5, mixed-compression intake) but with a characteristic length of 1.69 m (Herrmann et al., 2013). Similarly, the cross-sectional shape of the intake has been shown to have an observable effect on the trigger and mechanism of intake buzz. For instance, a study (Fisher et al., 1970) investigating the buzz characteristics of rectangular, external compression intakes reported the onset of buzz when ΔP_0 (stagnation pressure change across the vortex sheet entering the intake) was greater than 7%. On the other hand, another study (Zhang et al., 1983) investigating the same for axisymmetric external compression intakes reported stable flows until $\Delta P_0 < 11\%$. Throttling ratio (nozzle-exit-throat-area to intake-duct-exit-area), has been found to be another important parameter affecting intake buzz. As the throttling ratio is decreased, the buzz frequency increases (Fujiwara et al., 2002; Trapier et al., 2006).

Table 4.1: Supersonic Intake Buzz Studies

Reference	Methd	Geom.	Compression system	M	L (m)	Trigger	f (Hz)
Lu and Jain (1998)	Num	Axi	Two-shock	2	3.04	Dailey	27.7
Fujiwara et al. (2002)	Num	2D	Two-shock	1.4, 1.7, 2 (all design)	0.31	Ferri	60-200
Trapier et al. (2006)	Expt	2D	Mixed-compression	1.8, 2 (design), 3	1.861	Ferri, Dailey	120-140 (*little-buzz*), 12.4-20 (*big-buzz*)
Lee et al. (2011)	Expt, num	Axi, 2D	Mixed-compression	2.5	0.11	Ferri, Dailey	*little-buzz*: 386.7 (axi), 518 (2D); *big-buzz*: 312-447.8 (axi), 252.2-444.7 (2D)
Herrmann et al. (2013)	Expt	2D	Mixed-compression	2.5, 3-design, 3.5	1.69	Dailey	33-37
Soltani and Farahani (2013)	Expt	Axi	Two-shock	1.8, 2-design, 2.2	0.72	Ferri, Dailey	554 (*little-buzz*), 137 (*big-buzz*)
Chen et al. (2017)	Expt, theo	2D	Partially isentropic + two shocks	2	0.41	Dailey	124-204.4 (*little-* and *big-buzz*)
Chen et al. (2018)	Expt	2D	Partially isentropic + two shocks	2.5 (over-speed)	0.41	Dailey	162.3-214.9 (*little-*, *medium-* and *big-buzz*)
Yamamoto et al. (2019)	Num, expt	2D	Two-shock	2	0.24	Ferri	276-279 (*little-buzz*)

The elimination/avoidance of intake buzz and unstart comprise an essential part of the engine design process (Curran, 2001; Heiser and Pratt, 1994; Seddon and Goldsmith, 1999), as they can lead to undesirable effects like combustion instability, loss in thrust and even the complete failure of the engine system. A fundamental approach would be to incorporate stability constraints into the design. For instance, the Ferri-type instability can be avoided by choosing a cowl-lip angle so that the shock intersection point always remains outside the intake, thereby preventing the vortex sheet from entering the throat (Seddon and Goldsmith, 1999). Thus, this type of design eliminates the occurrence of Ferri-type instability, but at the cost of increased spillage (Seddon and Gold-smith, 1999). Intake stabilization can also be achieved using active flow control techniques such as variable-geometry intakes (Curran, 2001; Dalle et al., 2011; Fisher et al., 1970; Ogawa et al., 2010; Sorensen et al., 1976), over-speeding (Shapiro, 1953), over-board spillage (Moradian and Timo-feev, 2017; Veillard et al., 2008), and bleeds (Herrmann and Gülhan, 2014; Soltani et al., 2016; Trapier et al., 2006). In a variable-geometry intake, specific components of the geometry are var-ied to meet the corresponding demands of the flight envelope (Seddon and Goldsmith, 1999). The Eurofighter Typhoon, for instance, uses a hinged cowl lip that is varied to provide high incidences at low subsonic speeds, low spillage drag at high subsonic speeds, and a started supersonic flow in the form of an external compression geometry at Mach numbers 1.3-2 and a mixed compression geometry at Mach numbers between 2-2.5 (Seddon and Goldsmith, 1999). However, the variable-geometry method mainly suffers from the mechanical complexity and weight penalties associated with such designs. Over-speeding is a technique where the vehicle is accelerated beyond the design Mach number to swallow the normal shock and start the flow. This becomes increasingly difficult as the Mach numbers approach the hypersonic regime since the contraction ratio curve plateaus. During intake buzz, the flow oscillates between excessive and insufficient mass flow rates. In such scenarios, techniques like over-board spillage and bleeds are employed to vent out the excess fluid, thus dampening the oscillations. A study (Herrmann and Gülhan, 2014) reported an 8-27% in-crease in the throttling ratio until the onset of buzz with the use of boundary-layer-bleed systems.

63

Another study (Soltani et al., 2016) demonstrated improvements in the stability margin when the bleed slots were installed closer to the normal shock. Trapier et al. (2006) reported improvements in the intake pressure recovery and suppression of *little-buzz* oscillations using bleeds. However, the study also observed a decrease in the flow ratio. In addition to decreased flow ratios, bleeds increase the external drag, and adversely impact the intake stability and performance at high throttling ratios (Herrmann and Gülhan, 2014). In overboard spillage, the excess fluid is made to spill over the cowl, thereby swallowing the shock and starting the intake. Veillard et al. (2008) discussed a design method for this type of intake, and Moradian and Timofeev (2017) demonstrated the design prinicple for Prandtl-Meyer scramjet intakes. Similar to the bleed configuration, overboard spillage would increase the external drag experienced by the engine, which could potentially result in major thrust losses.

While the aforementioned methods have been shown to improve the intake stability and starting characteristics, benefits to performance (such as pressure recovery) have either been minimal or even detrimental (Ran and Mavris, 2005). In the previous study, an effort to improve the performance of supersonic/hypersonic intake systems was studied by injecting solid nanoparticles into a mixed-compression, supersonic intake (Jagannathan et al., 2019a). The study reported considerable gains ($\approx 16\%$) in the intake pressure recovery due to the momentum and energy transfer effects of the nanoaerosol. The injection of solid metal powders would also double as a fuel source due to the large gravimetric and volumetric energy densities of certain metals (e.g. Boron, Aluminum) (Goroshin et al., 2001). As it was shown that the advantageous exchange of momentum and energy between particles and the gas can improve the intake performance (Jagannathan et al., 2019a), it is expected that gas-particle interactions could also prevent unstart and associated instabilities.

The present study investigates the fundamental nature of gas-particle interactions on intake stability. A 1D analysis is performed to assess the isentropic and Kantrowitz limits of idealized supersonic intakes with nanoparticle injection. This is followed by CFD analysis of a rectangular,

external-compression, two-shock intake. Nanoparticles are injected from the ramp at three particle mass loading ratios (S_L) of 0, 0.12, and 0.24. Note that for Boron, $S_L = 0.105$ corresponds to stoichiometric combustion conditions. Therefore, $S_L = 0.24$ represents a very fuel-rich scenario or involves the temporary use of excess inert particles for the purpose of improving intake stability. The effect of stability is assessed by varying the throttling ratio of the expansion nozzle downstream to the intake.

4.2 1D Analysis

4.2.1 Governing Equations

An initial assessment of the intake operating limits was conducted using a quasi-1D compressible gas-particle flow model. The model assumes the following: a) particles are continuously distributed, incompressible, and spherical in shape; b) momentum transfer occurs only through aerodynamic drag; c) temperature is uniformly distributed within the particles and effect of thermal radiation is neglected; d) the system assumes two-way coupling ($\phi_p < 10^{-4}$, where ϕ_p is the particle volume fraction). The governing equations of the quasi-1D gas-particle model are described in Eqs. (4.1)-(4.6) (Jagannathan et al., 2019a).

Gas Phase Continuity Equation:

$$\frac{d(\rho A V)}{dx} = 0 \tag{4.1}$$

Gas Phase Momentum Equation:

$$\left(T_{\text{area}} + T_{\text{energy}} + T_{\text{drag}}\right) \left\{ \frac{M[2 + (\gamma - 1)M^2]}{2(1 - M^2)} \right\} = \frac{dM}{dx} \tag{4.2}$$

$$T_{\text{area}} = \frac{-1}{A} \frac{dA}{dx} \tag{4.3}$$

$$T_{\text{energy}} = \frac{1 + \gamma M^2}{2T_0} \frac{dT_0}{dx} \tag{4.4}$$

65

$$T_{\text{drag}} = \frac{S_{\text{L}}V}{RT_0}\left(1 + \frac{\gamma-1}{2}M^2\right)\frac{dV_p}{dx} \tag{4.5}$$

T_{area}, T_{energy}, and T_{drag} represent the area (pressure) source term, energy source term, and aerodynamic drag term, respectively.

Gas Phase Energy equation:

$$C_{\text{p}}\frac{dT_0}{dx} = \frac{-6S_{\text{L}}Nu_{ps}\kappa_s}{\rho_p D_p^2 V}(T_{aw} - T_p) - S_{\text{L}}V_p\frac{dV_p}{dx} \tag{4.6}$$

Particle Momentum Equation:

$$C_{\text{D}}\frac{1}{2}\rho V_r \mid V_r \mid S_{\text{ref}} = m_p V\frac{dV_p}{dx} \tag{4.7}$$

Particle Thermal Energy Equation:

$$\frac{6Nu_{ps}\kappa_s(T_{aw} - T_p)}{\rho_p D_p^2 V} = C_{\text{pp}}\frac{dT_p}{dx} \tag{4.8}$$

4.2.2 Case Setup

The effects of particle injection on the startability of supersonic intakes were assessed using a converging duct geometry. Intake startability is characterized by computing the isentropic and Kantrowitz contraction limits. The operating range of the intake is based on possible pressure ratio (P^*/P_∞) and Mach number ranges (ΔM) determined from the analysis. The parameter, P^*/P_∞, is obtained for an isentropic compression process with a sonic flow at the exit, as described by the functional relationship in Eq. (4.9). ΔM is defined as the range of isentropic operating speeds obtained by varying S_{L} for a fixed geometry intake, as described in Eq. (4.10). The gas-particle system, described by Eqs. (4.2)-(4.8), was discretized using a fourth order Runge Kutta method.

$$\left(\frac{P^*}{P_\infty}, \frac{A^*}{A_\infty}\right) = f\left(S_{\text{L}}, M_\infty\right) \tag{4.9}$$

$$(\Delta M) = f\left(\frac{A^*}{A_\infty}, M_\infty, S_{\text{L}}\right) \tag{4.10}$$

Inflow boundary conditions were selected to represent supersonic flight at an altitude of 30 km, which is similar to the cruise conditions of other high-speed vehicle concepts with advanced intake systems (Jivraj et al., 2007). Based on the International Standard Atmosphere (ISA), this altitude corresponds to a temperature and pressure of 226.51 K and 1197 Pa, respectively. Boron nanoparticles were selected as the corresponding particle-type, with $C_{pp} = 1026 \, \text{kJ} \, \text{kg}^{-1} \, \text{K}^{-1}$ and $\rho_p = 2370 \, \text{kg} \, \text{m}^{-3}$. Again, as described in Goroshin et al. (2001); Jagannathan et al. (2019a), Boron is a desirable solid fuel for high-speed airbreathing engine systems due to its high gravimetric and volumetric energy densities.

4.2.3 Results
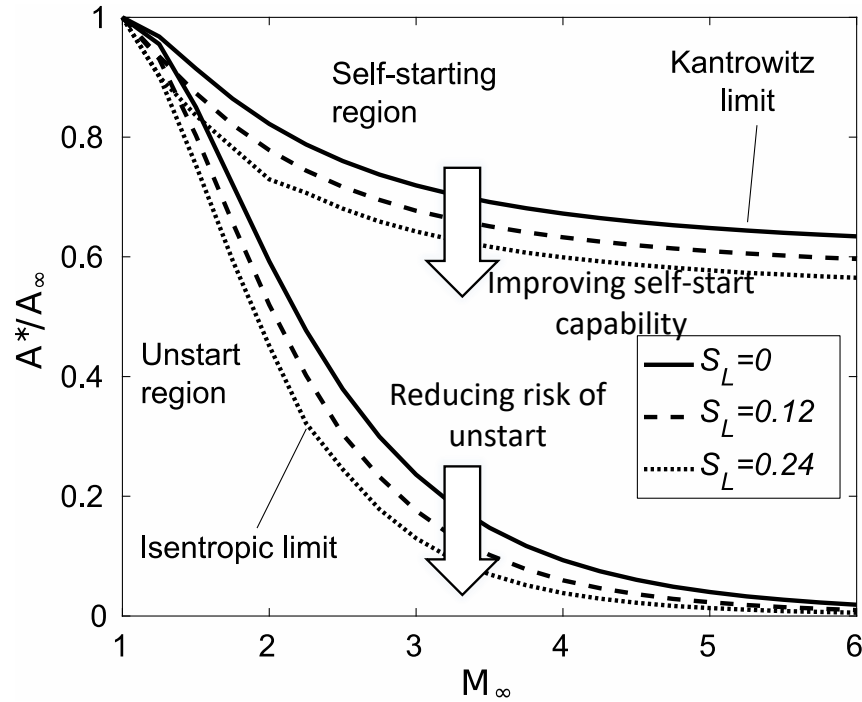
Figure 4.1: Starting and Kantrowitz limits of a converging intake with, and without particles

The isentropic and Kantrowitz contraction limits are shown in Fig. 4.1, at particle mass loading ratios of 0, 0.12, and 0.24. The region between the two curves represents the dual solution region, where both the unstarted and started configurations are possible. In order to satisfy the compression requirements of an engine system, the intake is typically designed close to the isentropic curve

and is forcibly started through external mechanisms (e.g. variable geometry for instance). The 1D analysis shows a positive correlation between particle mass loading and improved operational limits of the intake at all Mach numbers.

Even a small change in the contraction ratio at the isentropic limit results in a large increase in the operational range of the intake. For example, at a design Mach number of $M = 6$, the injection of nanoparticles at a mass loading of $S_L = 0.24$ results in an increase in the maximum pressure ratio by 200% (see Fig. 4.2). Similarly, Fig. 4.3 shows that an intake designed for Mach 6 can be operated down to Mach 4.3 if nanoparticles are injected at a mass loading of $S_L = 0.24$.
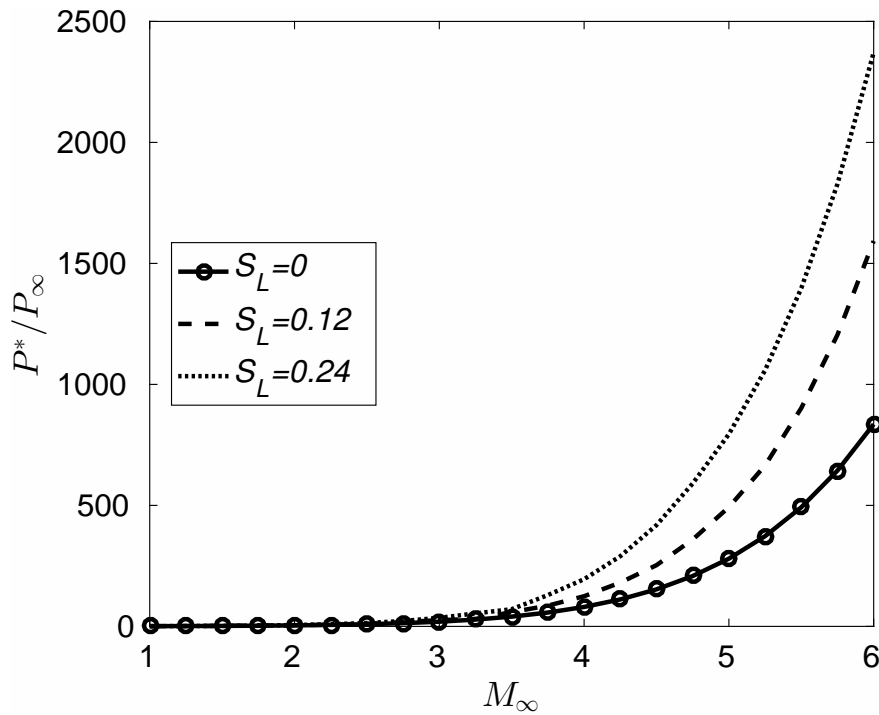
Figure 4.2: Effect of particle mass loading ratio on the exit pressure ratio of an idealized intake

While the 1D analysis is useful for predicting potential performance gains with the use of particles, CFD is required to assess the effect of nanoparticles across a practical intake design, and to predict more complex phenomena such as Ferri- and Dailey-type instabilities (Seddon and Goldsmith, 1999). Therefore, unsteady, compressible, multi-phase, 2D simulations of a realistic supersonic intake were performed using a custom-modified OpenFOAM solver described in the next section.
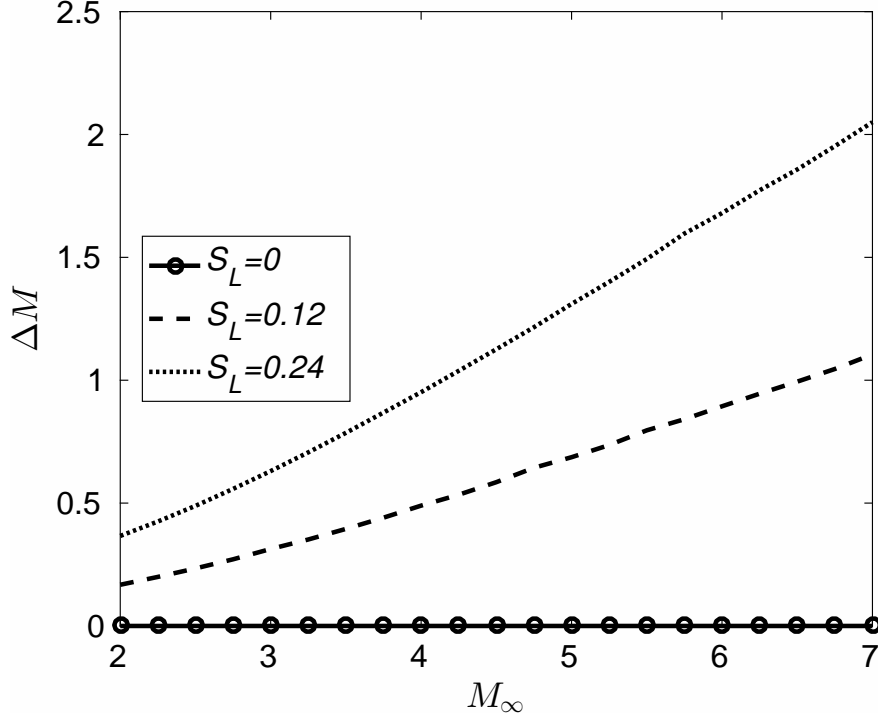
Figure 4.3: Effect of particle mass loading on the operating Mach number range of an idealized intake, demonstrating an increase in the operating range (at a fixed intake geometry) as S_L is increased

4.3 CFD Study

4.3.1 Governing Equations and Solver Setup

CFD simulations were performed using rhoCentralLPTFoam, a modified density-based, compressible, gas-particle flow solver in OpenFOAM. The carrier phase is modeled using the Eulerian approach, which is adopted from rhoCentralFoam. RhoCentralFoam is a decoupled explicit solver of compressible Navier Stokes equations which uses the KT and KNP schemes (Kurganov et al., 2001), that are total variation diminishing. There are several verification and validation studies on rhoCentralFoam in the literature (Arisman et al., 2015; Greenshields et al., 2010; Hinman, 2017; Hinman and Johansen, 2016a,b; Jagannathan et al., 2019a; Jasak, 1996; Teh and Johansen, 2016). The dispersed phase was modeled using the Lagrangian parcel tracking algorithm, where each parcel (or computational particle) represents a collection of physical particles. A detailed description of the custom Eulerian-Lagrangian solver and its governing equations is given in (Jagannathan

et al., 2019a,b).

4.3.2   Computational Domain and Boundary Conditions
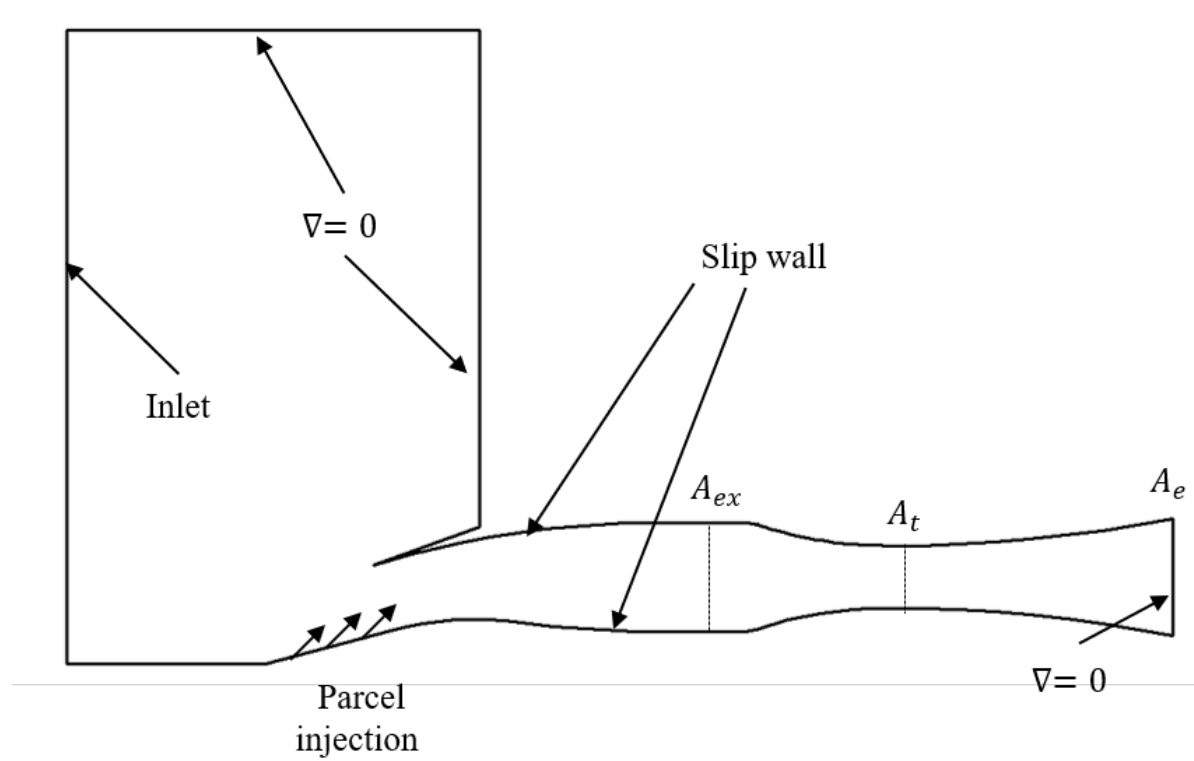
Figure 4.4: Computational domain and boundary conditions of the CFD setup, where the subscripts ex, t, and e represent the intake exit, nozzle throat, and nozzle exit conditions

The goal of the CFD study is to evaluate the stability characteristics of a realistic supersonic intake when nanoparticles are injected. For that purpose, the following constraints were imposed on the computational domain: a) the domain should represent a practical intake configuration while being simple enough to capture the fundamental aspects of the gas-particle system inside the intake; b) the domain should include a physical trigger for instability; c) the domain should incorporate a practical method of particle injection. Based on the above requirements, a two-shock, external-compression intake was selected (Fujiwara et al., 2002) (as seen in Fig. 4.4). Intake buzz was generated by varying the throttling ratio (A_t/A_{ex}) of the expansion nozzle. Inflow boundary conditions ($P = 1197\,\text{Pa}$, $T = 226.51\,\text{K}$) were selected to represent a Mach 2 flight at an altitude of 30 km.

Table 4.2: Grid convergence

Case	Cells	Parcels (s^{-1})	Refinement ratio (r)
Coarse	8×10^4	0.5×10^8	4
Medium	3.2×10^5	1×10^8	2
Refine	1×10^6	2×10^8	1

A_t/A_{ex} was varied from 0.57 until 0.44, while S_L was varied from 0 to 0.24. Nanoparticles were injected from the ramp at an angle of $30°$ relative to the horizontal, and at speeds and temperatures equal to those of the freestream gas. The injection angle was selected with the aim of achieving higher particle concentrations closer to the ramp-side of the flow, where the flow remains supersonic because of the two-shock compression system (as opposed to the single-shock compression region closer to the cowl-side of the flow during intake buzz). As discussed in Chapter-3, particles are only effective in improving the intake performance when the flow is supersonic (Jagannathan et al., 2019a).

Slip wall boundaries were specified at all surfaces for several reasons. First, shock-boundary-layer interactions are complex and would make the interpretation of the results difficult when trying to isolate and observe the effects of particle-gas interactions on the Ferri-type instability. Second, the growth and state of the boundary layer is directly influenced by the overall engine length scale. By removing the boundary layer, the results will have more generality and will not be tied to a single engine size. Finally, the end effect of specifying a slip-wall boundary would be similar to using boundary-layer-bleeds. Therefore, the results shown here could also be interpreted as the effects of particle-gas interactions combined with the implementation of ideal boundary-layer bleed along the surfaces. Nonetheless, the presence of boundary layers should be investigated in a future work, especially for flows with low Reynolds number or when shock-boundary-layer-interactions become a major factor.

4.3.3 Verification

The CFD of supersonic gas-particle intake systems deals with several modeling challenges such as flow unsteadiness, shock capture, and gas-particle interaction terms. For this reason, a verification analysis was conducted to ensure grid convergence while analyzing the intake buzz and performance. Convergence was evaluated for both the carrier and discrete phases. The analysis was performed using three structured grids created in Pointwise, where each stage of refinement was obtained by both doubling the grid points (carrier phase convergence) and number of injected parcels (discrete phase convergence) from the coarser case (shown in Tab. 4.2).

Predictions of non-dimensionalized stagnation pressure (π) distributions along the intake wall for several grids are shown in Fig. 4.5. Numerical uncertainties were calculated through the grid convergence index (*GCI*), which is estimated using the generalized Richardson extrapolation method (Roache, 1997). A global estimate of the observed order of accuracy was used in the calculation of *GCI*, which was obtained by averaging the local orders of accuracy (Oberkampf and Roy, 2010). A factor of safety of 1.25 was used at monotone nodes while a value of 3.0 was used at nodes exhibiting an oscillatory convergence behavior (Oberkampf and Roy, 2010). The net *GCI* of π (distributed over the wall) between medium and refined grids was found to be approximately 2%, which was considerably smaller than the 8% difference in (time-averaged) pressure recovery observed between $S_L = 0$ and $S_L = 0.24$.

Sampling data was obtained by observing the exit pressure transience, as seen in Fig. 4.6. Once the initial transience disappears, the pressure oscillates periodically. A sampling time of $0.14\,\text{s}$ ($\Delta t_{\text{sample}}/\tau_g = 270$) was selected so as to characterize intake buzz with minimal errors while minimizing the computational expense. The base frequency of the oscillations were found to be in the range of 100-200 Hz and the sampling rate corresponds to a Nyquist frequency of $1000\,\text{Hz}$. Verification analysis of the intake buzz was conducted by comparing the fundamental frequency of the buzz oscillations for different grids. These parameters were calculated using a power-spectral density (PSD) analysis of pressure fluctuations and shock motion. The convergence behavior of
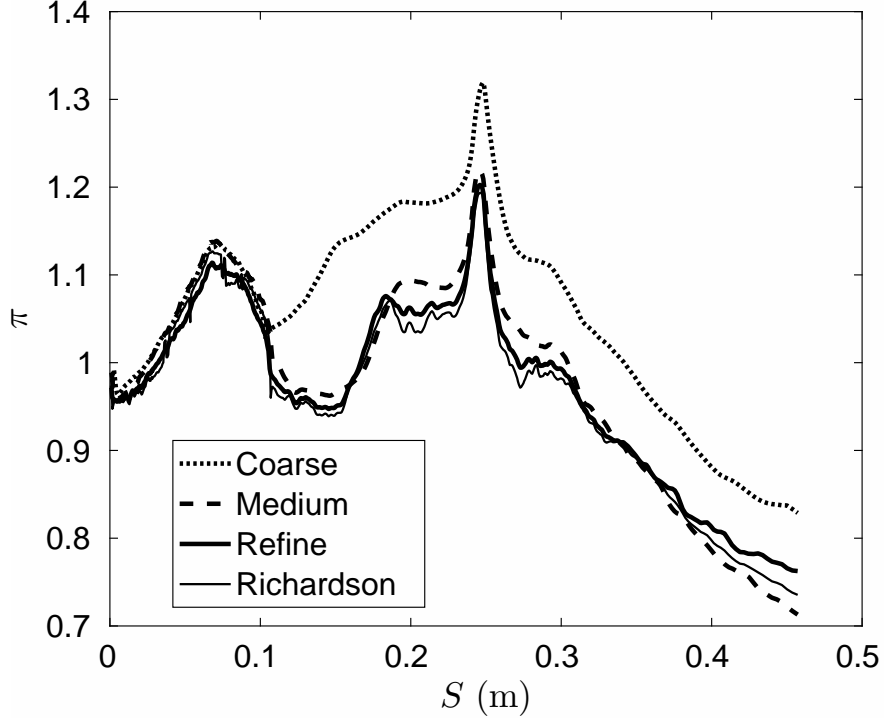
Figure 4.5: Grid convergence of time-averaged, non-dimensionalized stagnation pressure plot along the intake wall ($A_t/A_{ex} = 0.50$ and $S_L = 0.24$)

the oscillation frequency has been shown in Fig. 4.7. The *GCI* based on the o scillation frequency, between the medium and refined grid, was estimated to be 2%.

In addition to grid convergence, CFD simulations using the medium grid for the gas-only case were compared to CFD results reported by Fujiwara et al. (2002). In that work (Fujiwara et al., 2002), slip flow wall boundaries were also specified. Fig. 4.8 shows the comparison of the predicted time-averaged mass flow rate ratio for various throttle parameters to the CFD results by Fujiwara et al. (2002). Disagreement between the two CFD predictions are less than 2%. As a result, the medium grid was selected as the reference grid for the current work.

4.3.4 Results

Starting Characteristics:

As described above, the external compression system (Fujiwara et al., 2002) was designed for a gas-only flow at a freestream Mach number of 2. The design point occurs when $A_t/A_{ex} = 0.57$
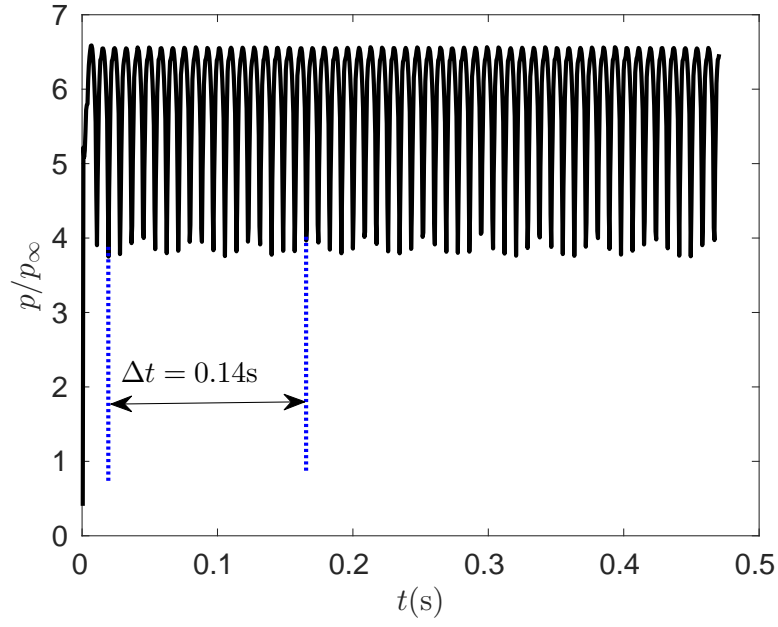
Figure 4.6: Pressure transience observed at the intake exit, $x/L = 0.77$, $S_\text{L} = 0$
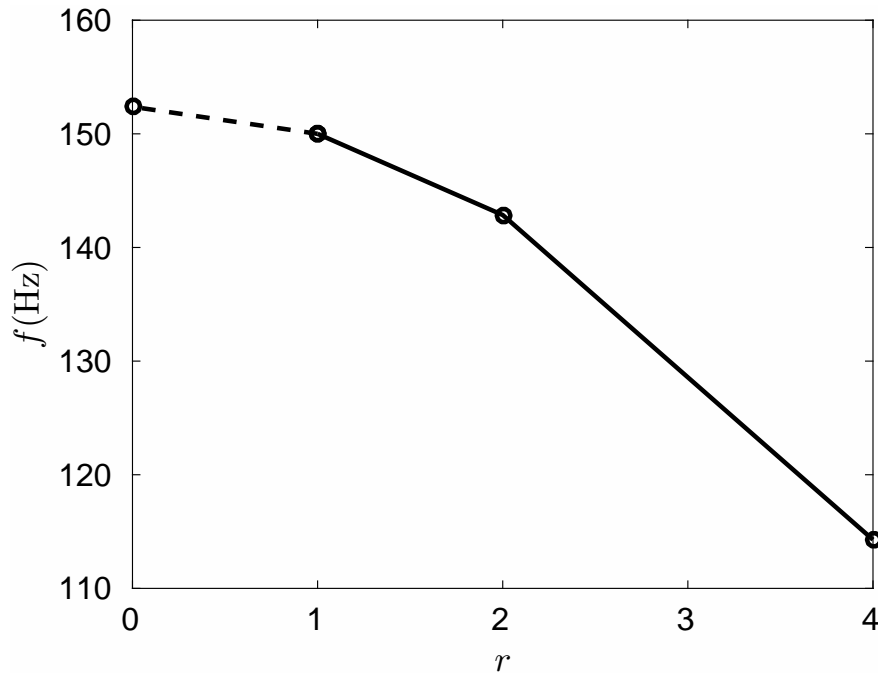
Figure 4.7: Grid convergence based on the oscillation frequency ($A_t/A_{ex} = 0.50$, $S_\text{L} = 0.24$)
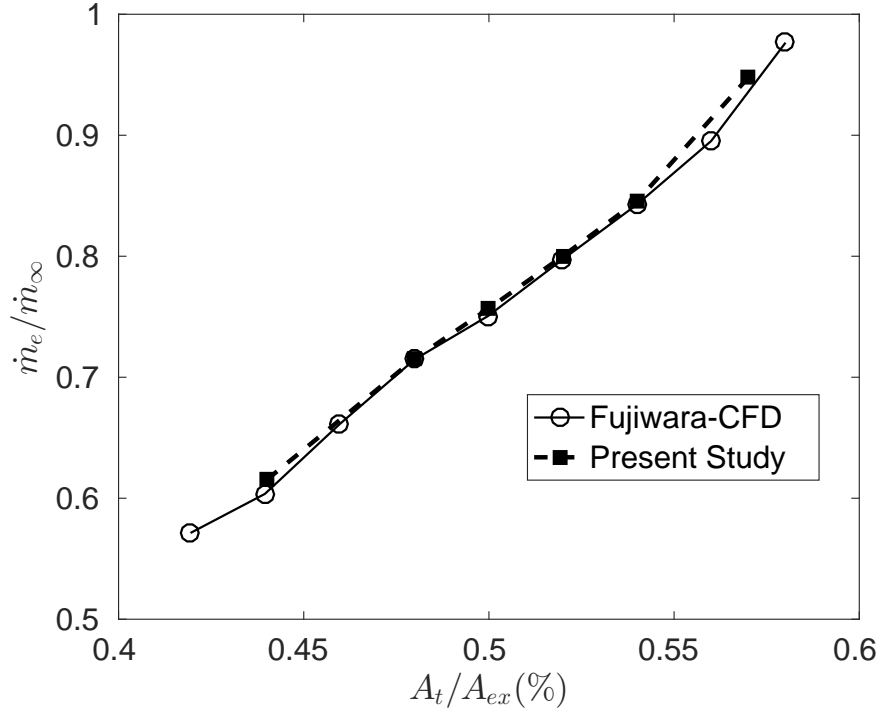
Figure 4.8: Comparison of the predicted mass flow rate ratio to CFD results in the literature (Fujiwara et al., 2002)

| (a) | (b) |
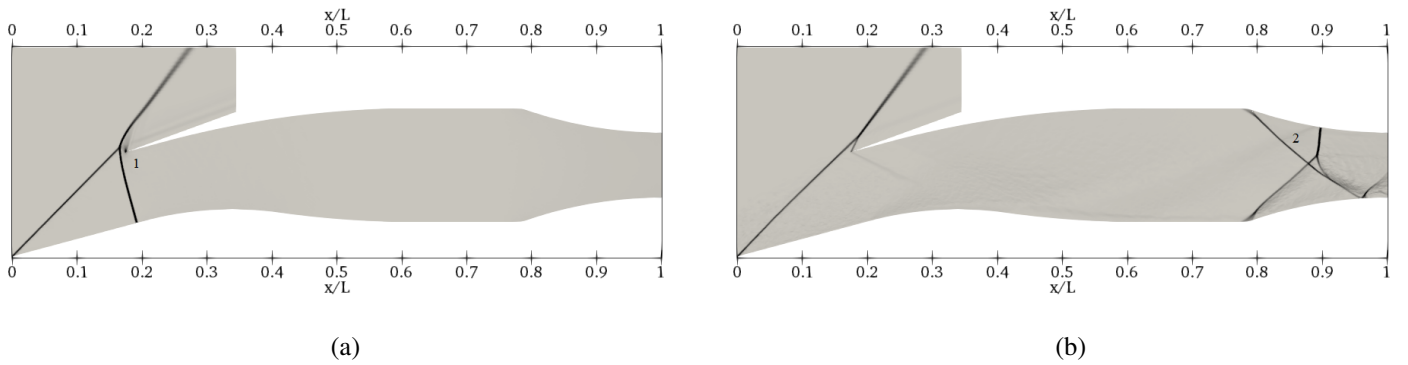
Figure 4.9: Synthetic schlieren images ($A_t/A_{ex} = 0.57$) at: a) $S_L = 0$, where the normal shock is stationary at the cowl-lip (point 1); b) $S_L = 0.24$, which represents a fully started, supersonic flow inside the intake, with the normal shock pushed downstream to the expansion nozzle (point 2)

and the unstart occurs when $A_t/A_{ex} = 0.44$. In the former case, the flow at $S_L = 0$ encounters a stationary normal shock at the lip (labeled as point 1 in Fig. 4.9(a)) and a steady flow is established. In the latter case ($A_t/A_{ex} = 0.44$), the normal shock moves upstream in front of the intake (see point 3 in Fig. 4.10(a)) and establishes a subsonic flow throughout the duct. As expected, the particle injection significantly affects the intake flow at a fixed throttling ratio. For instance, the normal shock moves downstream (shown by point 2 in Fig. 4.9(b) and point 4 in Fig. 4.10(b)) as the particle mass loading is increased. At $A_t/A_{ex} = 0.57$ and $S_L = 0.24$, the normal shock is swallowed by the intake ($x_{msh}/L \approx 0.9$), which results in a fully started flow. However, an unsteady flow is established at $S_L = 0.12$ at the same throttling ratio ($A_t/A_{ex} = 0.57$), which is investigated in the next section. At $A_t/A_{ex} = 0.44$ and $S_L = 0.24$, the normal shock moves downstream from $x/L \approx 0$ to $x/L \approx 0.12$, as seen at point 4 in Fig. 4.10(b). To further substantiate this behavior, time-averaged locations of the normal shock (x_{msh}) have been compared against different particle loadings at various throttling ratios in Fig. 4.11. It was found that x_{msh} increases with A_t/A_{ex} and S_L. In other words, the greater the particle loading, further downstream the normal shock location shifts. Hence, these observations show that the injection of nanoparticles improves the starting characteristics of the intake system.

(a)   (b)
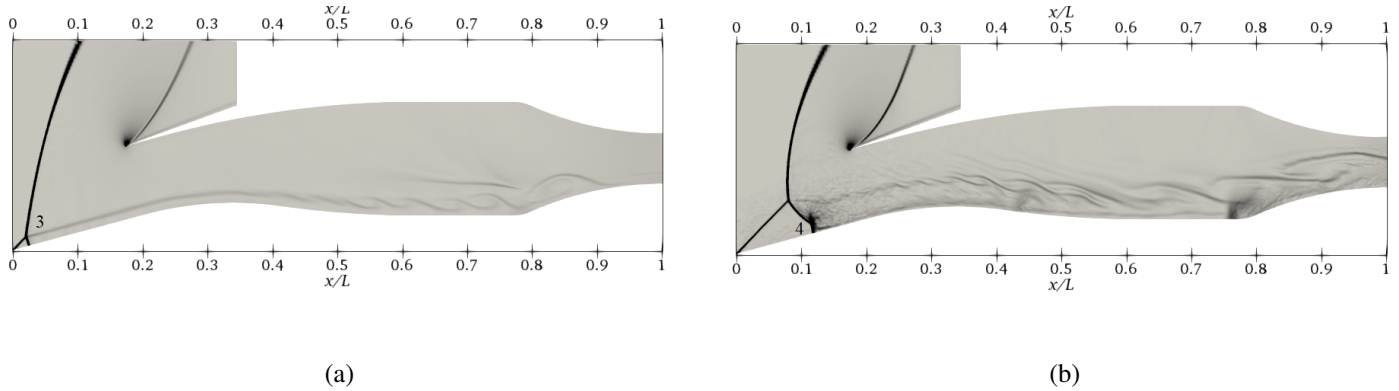
Figure 4.10: Synthetic schlieren images at $A_t/A_{ex} = 0.44$ at: a) $S_L = 0$, where point 3 represents intake unstart; and b) $S_L = 0.24$, when the normal shock moves downstream to point 4
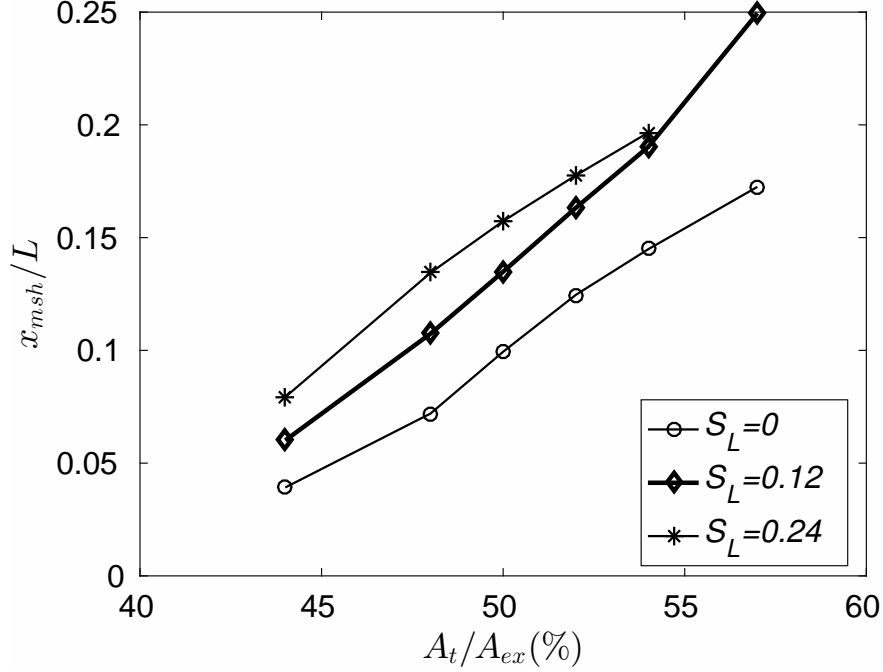
Figure 4.11: The time-averaged shock position against the nozzle ratio at varying S_L, where $x_{msh} = 0$ corresponds to the ramp leading edge and $x_{msh}/L = 0.175$ indicates a normal shock at the cowl-lip

Buzz Mechanism:

The effect of S_L on flow stability was investigated by decreasing A_t/A_{ex} from 0.54 (when the Ferri-type instability is triggered) to 0.44 (when unstart is observed for the gas-only case). The buzz cycle for a typical intake flow without particles is shown in Fig. 4.12. The cycle begins with a high back pressure (not shown in figure) and the normal shock at the cowl-lip (denoted by point 5 in Fig. 4.12(a)); the high back pressure forces the normal shock to move upstream (denoted by point 7 in Fig. 4.12(b)). The upstream-moving normal shock interacts with the oblique shock which results in a vortex sheet entering the intake (see point 6 in Fig. 4.12(b)). As a result, the captured flow is non-uniform and comprises of a slower moving region near the cowl-side of the intake (see point 8 in Fig. 4.12(c)) and a faster moving region with a greater pressure recovery near the ramp-side of the intake (see point 9 in Fig. 4.12(c)). The vortex sheet then separates and grows while moving downstream (observed by point 10 in Fig. 4.12(c)). At $t = 0.0069$ s (see point 11 in Fig. 4.12(d)), the normal shock reaches the extreme upstream position, where the flow entering the cowl is at

77
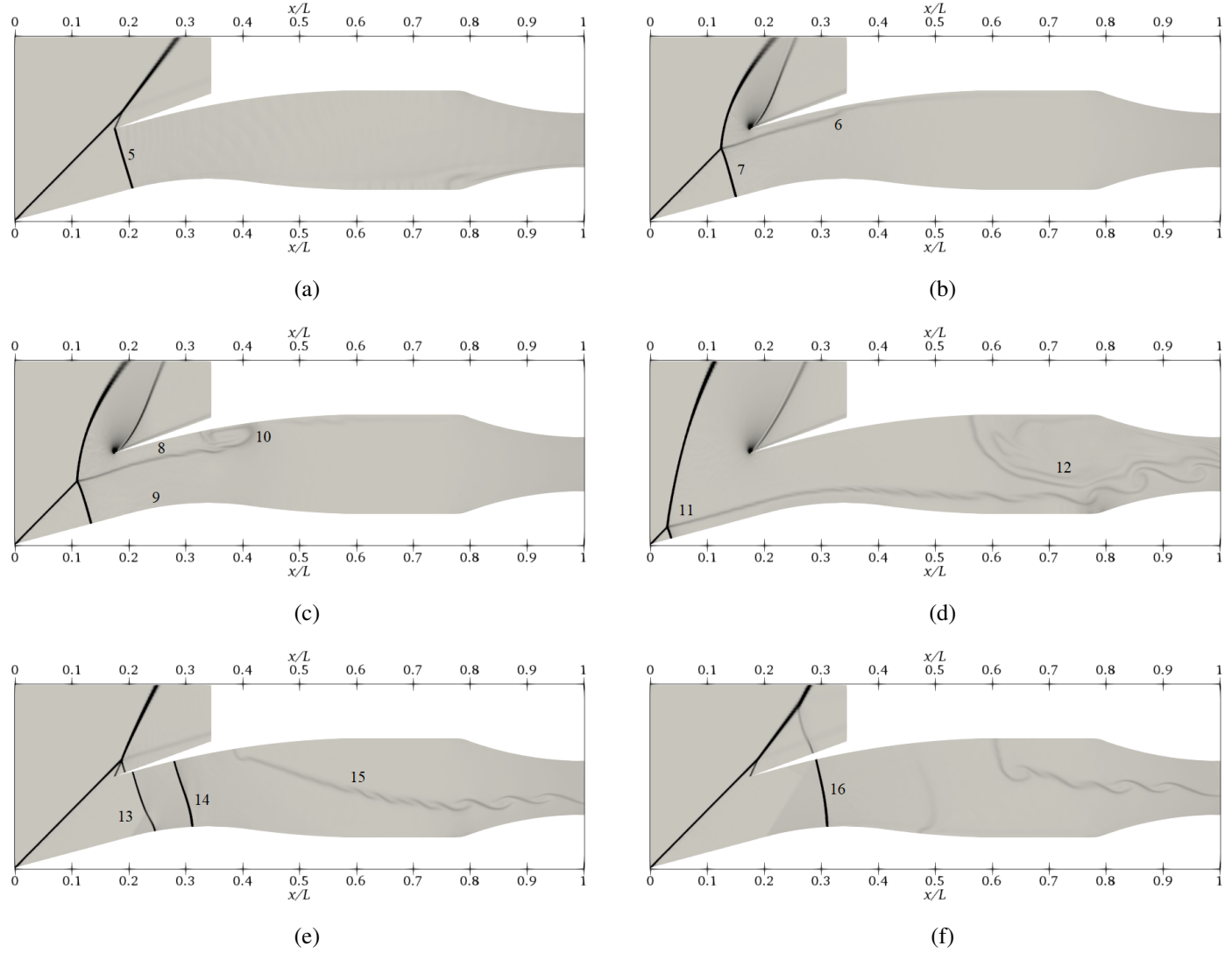
Figure 4.12: Synthetic schlieren images at $A_t/A_{ex} = 0.54$ and $S_L = 0$ at: a) $t = 0.0021$ s, when the normal shock is at the cowl-lip (point 5); b) $t = 0.0041$ s, when the vortex sheet enters the intake (point 6); c) $t = 0.0046$ s, when the vortex sheet separates (point 10); d) $t = 0.0069$ s, when x_{sh} is minimum (point 11); e) $t = 0.0085$ s, when the shock moves downstream (point 13); f) $t = 0.009$ s, when the normal shock returns to the super-critical position (point 16)

the minimum. At the same time, the flow exiting the nozzle is greater (not shown in figure), thus resulting in a pressure wave that forces the normal shock downstream (see point 13 in Fig. 4.12(e)). The cycle ends with the normal shock reaching the extreme downstream position, when the flow rate entering the intake is maximum (see point 16 in Fig. 4.12(f)). Hence, the intake flow oscillates between excessive (super-critical) and deficient (sub-critical) flow rates.
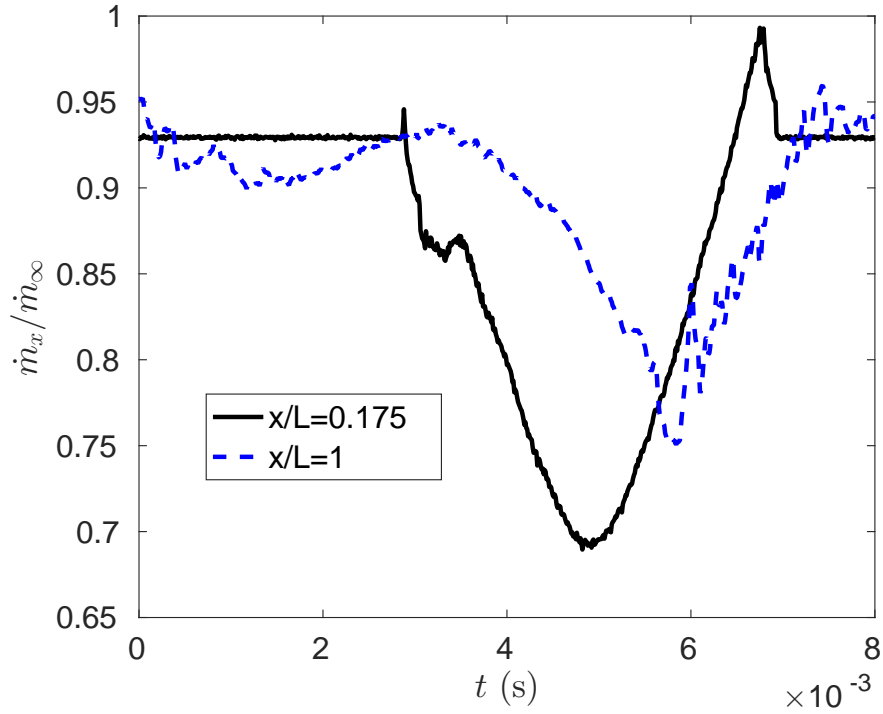
Figure 4.13: Flow ratio varying with time during a single buzz cycle at $A_t/A_{ex} = 0.54$ and $S_L = 0.12$, showing a temporal delay between the two locations

The buzz cycle for an intake flow with particle injection has been described using the synthetic Schlieren images in Fig. 4.14 and the flow ratio curve (plotted at the intake cowl and nozzle throat) in Fig. 4.13. Firstly, the buzz mechanism with particle injection is characterized by the formation of two different separation regions instead of just the one observed for the flow without particles. The cycle begins at a super-critical state where the normal shock lies inside the intake (see point 17 in Fig. 4.14(a)) and the flow entering the cowl is steady (seen in Fig. 4.13). At the same time, the flow exiting the nozzle throat fluctuates (due to the motion of separated flow regions from the previous cycle). The observed fluctuations in the nozzle flow rate causes a disturbance in pressure

79
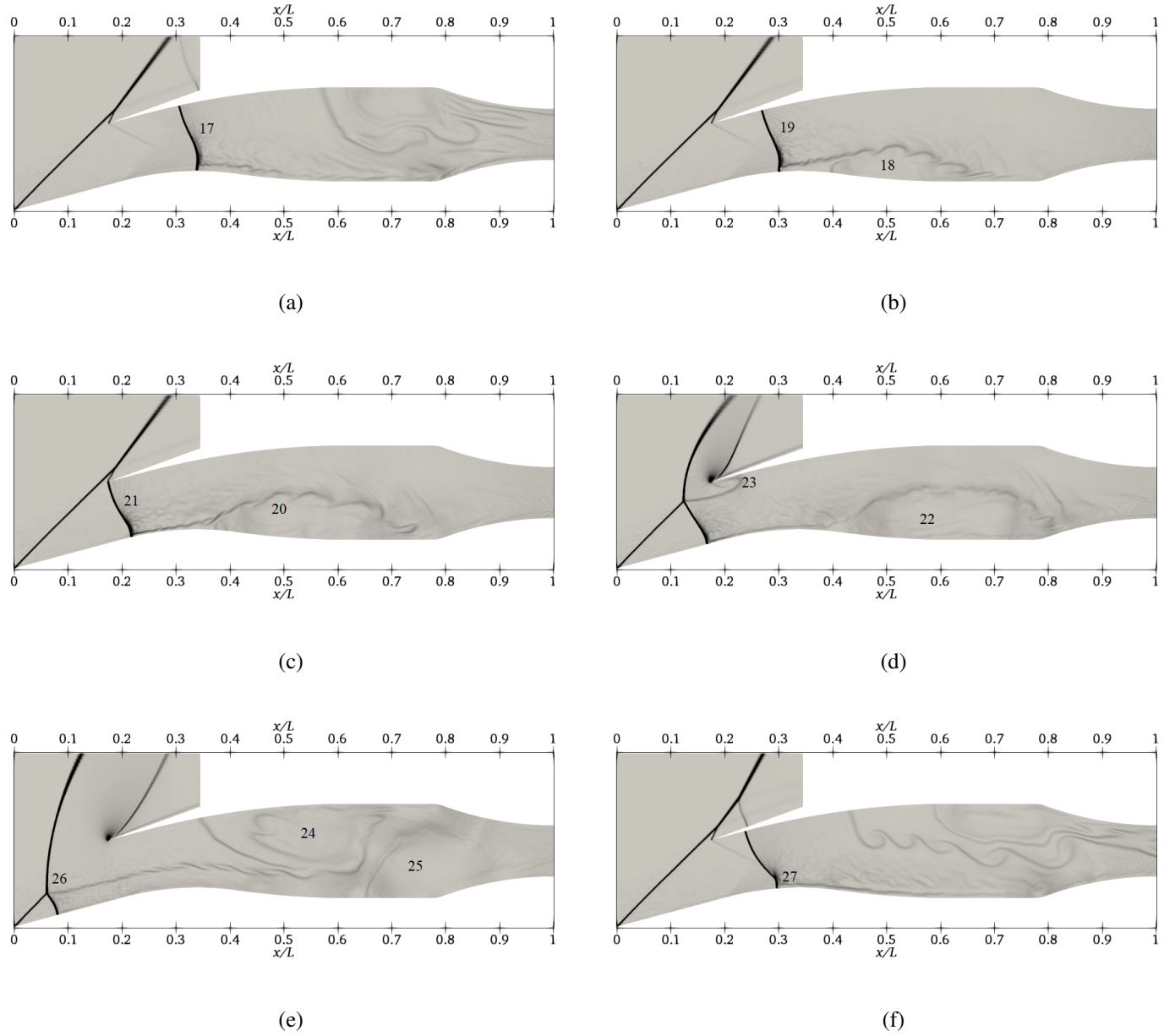
Figure 4.14: Synthetic schlieren images at $A_t/A_{ex} = 0.54$ and $S_L = 0.12$ at: a) $t = 0$ s, when x_{sh} is maximum (point 17); b) $t = 0.00162$ s, when particle-induced separation initiates (point 18); c) $t = 0.00288$ s, when the normal shock moves to cowl-lip (point 21); d) $t = 0.00378$ s, when the vortex sheet separates (point 23); e) $t = 0.00534$ s, showing vortex sheet separation (point 24) and particle-induced separation (point 25); f) $t = 0.00729$ s, when the shear layer is generated from the shock-particle-gas interactions (point 27) at the super-critical state

that is transmitted upstream (not shown in figure), which forces the normal shock to move upstream at $t = 0.00162$ s (as seen by point 19 in Fig. 4.14(b)). During the same period, the first separation region is generated behind the normal shock (seen by point 18 in Fig. 4.14(b)) near the ramp-side inside the intake. The shock continues to travel upstream and reaches the cowl lip at $t = 0.00288$ s (point 21 in Fig. 4.14(c)), while the first separation region grows as it moves downstream (point 20 in Fig. 4.14(c)). The flow rate entering the cowl remains unaffected by the flow features inside the intake until this period (Fig. 4.13). However, as the shock continues to move upstream, the vortex sheet (similar to the one observed in the case without particles) enters the intake (point 23 in Fig. 4.14(d)), resulting in the formation of a second separation region at $t = 0.00378$ s which causes a sudden decrease in the cowl flow rate (seen in Fig. 4.13). The cowl flow rate reaches a minimum at $t = 0.00534$ s while the nozzle flow rate remains greater. The greater flow rate exiting the nozzle results in a decreased back pressure (not shown in figure), which causes the normal shock to travel downstream. The normal shock then reaches the super-critical position observed at $t = 0.00729$ s (see point 27 in Fig. 4.14(f)). At this stage, a shear layer is formed behind the normal shock in the ramp-side of the intake, the breakdown of which results in the first separation region that was observed during the initial stages of the cycle. The buzz cycle repeats when the shock reaches the extreme downstream position again (see point 17 in Fig. 4.14(a).

The self-sustained oscillations in the buzz phenomenon occurring at $S_L = 0.12$ is fundamentally similar to the case observed at $S_L = 0$. In both of these cases, the oscillations are sustained by a source of instability that travels downstream and a pressure wave that propagates upstream (Ho and Nosseir, 1981). However, as explained above, the buzz cycle with particle injection consists of two sources of instabilities, while the single-phase case comprises of only one source. The two instability sources observed with the particle-injected cases are generated from the separation of shear layer beind the normal shock near the ramp-side of the intake and the separation of vortex sheet entering the cowl-side of the intake. The former is a result of particle injection and the latter is generated from the normal-oblique shock interactions (also known as the Ferri-type instability

(Ferri and Nucci, 1951)). The ramp-side shear layer is likely generated because of the following factors: the relative differences in the particle-injection angle and the flow angle behind the oblique shockwave; particle inertia; normal shock strength; and the presence of an adverse pressure gradient in the subsonic diffuser.

The relative impact of particle mass loading on stability was assessed by comparing the shock amplitudes at varying throttling ratios, as seen in Fig. 4.15. It was found that the shock amplitude increases with S_L. However, at $A_t/A_{ex} = 0.57$ and $S_L = 0.24$, the intake reaches a fully started condition, resulting in a zero-amplitude, steady supersonic flow inside the intake. Hence, the formation of two separation regions, observed with particle injection, negatively impacts intake stability, as observed in Fig. 4.15.
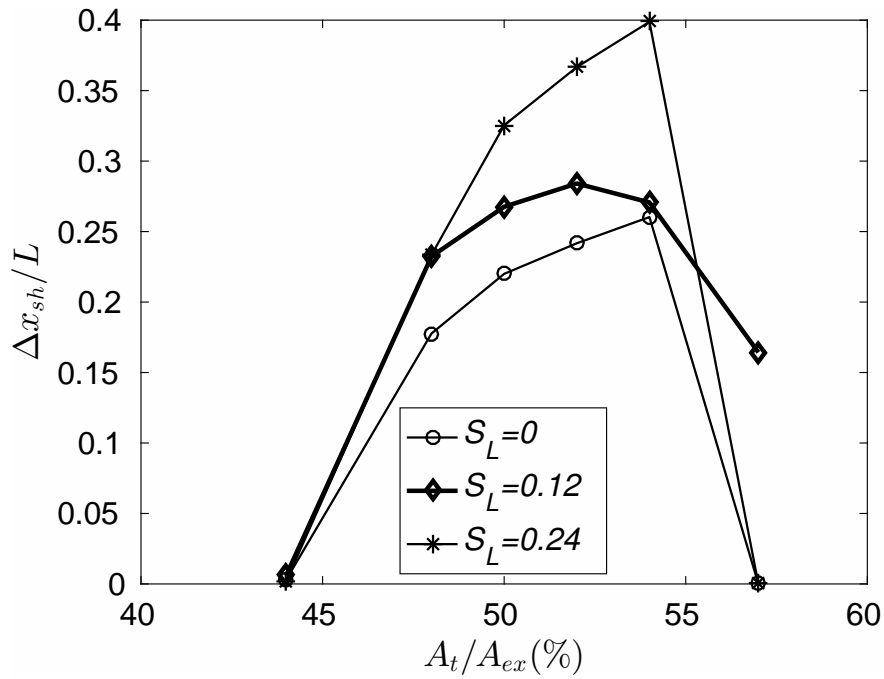
Figure 4.15: Normal shock amplitude against the throttling ratio at varying S_L, where $\Delta x_{sh} = 0$ denotes a steady, subsonic flow with a stationary normal shock ($A_t/A_{ex} = 0.44$), or a fully-started, supersonic flow without any normal shocks ($S_L = 0.24$, $A_t/A_{ex} = 0.57$)

4.4 Discussion

The physics of intake flow starting and stability were studied for high-speed intake systems with particle injection. Through a 1D analysis, it was revealed that were: a) improvements in starting and maximum contraction ratios with particle mass loading ratio; b) considerable changes in the operating Mach number range and pressure ratio. CFD simulations conducted across a rectangular external compression two-shock intake were shown to improve the starting characteristics of the intake but predicted an increase in the amplitudes once the buzz initiated. The negative impact on stability with particle mass loading has been attributed to the formation of a second separation bubble. This is likely caused by a combination of factors such as the relative difference between particle injection angle and flow angle behind the oblique shockwave, dynamic and thermal inertia of nanoparticles, relative normal shock strength between particle-filled and particle-free zones; and the adverse pressure gradient of the subsonic diffuser.

Chapter 5

Conclusions

5.1 Verification and Validation

A novel method, known as the mixed polynomial extrapolation, was developed for estimating the discretization errors in the dispersed phase for multiphase flows with one-way coupling. The mixed polynomial extrapolation was found to provide a consistently more accurate solution than the generalized Richardson extrapolation method, when tested for cases of supersonic flows across a compression ramp and diverging duct.

5.2 Performance Analysis of Supersonic Intakes

By conducting a similarity profile analysis of the governing quasi-1D gas-particle equations, four independent particle parameters of the system were identified: particle mass loading ratio, particle Eckert number (momentum and pressure work transfer), thermal transport number (interphase heat transfer), and Stokes number (particle size). A 1D parametric analysis of an idealized converging-diverging intake revealed the following: a) there were considerable gains in pressure recovery with nanoparticle injection (in some cases $\pi_c > 1$) for idealized and single-shock compression cases; and b) these gains in pressure recovery were only achieved beyond a certain threshold combination of cooling (high α_t), injection velocity (high Ec_p), and particle size (low Stk). For instance, at a freestream Mach number of 5 ($V_\infty = 1508\,\mathrm{m\,s^{-1}}$) and particle size of $D_p = 500\,\mathrm{nm}$ ($Stk = 0.007$), gains in pressure recovery (idealized compression case) were observed for particle injection temperatures lower than $408\,\mathrm{K}$ ($\alpha_t > 0.7$) and velocities greater than $828\,\mathrm{m\,s^{-1}}$ ($Ec_p > 0.5$). CFD simulations conducted on a 2D mixed-compression Mach-3 intake predicted a 16% increase in exit pressure recovery with nanoparticle injection, which is consistent with the

22% gain from the 1D analysis. In a multi-shock mixed compression intake, momentum and energy exchanges between the two phases occur through dynamic and thermal non-equilibrium conditions established behind the shockwaves, resulting in the observed gains in pressure recovery.

5.3   Stability Analysis of Supersonic Intakes

Through a quasi-1D analysis across converging intakes, the starting characteristic, which was measured through the isentropic and Kantrowitz compression limits, was observed to improve with the particle mass loading ratio. The 1D result was further substantiated with the CFD results obtained for a 2D, two-shock, external compression intake at Mach 2. For instance, in the CFD study, the time-averaged shock location was observed to move downstream as the particle mass loading ratio was increased. Furthermore, at a throttling ratio of 0.57, a fully started intake flow was achieved at a mass loading of 0.24, while the same geometry at a particle mass loading ratio of 0 resulted in the formation of a normal shock at the cowl-lip. On the other hand, the injection of nanoparticles from the ramp (at an angle of $30°$) was found to have an adverse impact on the intake stability. For instance, the shock-amplitude was found to increase with the particle mass loading ratio. The adverse impact on stability with particle injection has been attributed to the formation of a particle induced separation (PIS) region. The PIS region occurs due to a combination of contributing factors: particle injection location; injection angle; Stokes number; particle Eckert number; particle mass loading ratio; and thermal transport parameter.

Chapter 6

Future Studies

6.1 Verification and Validation

Research studies on verification and validation constitute a significant component in the development of CFD. This study lays a strong groundwork for the solution verification process applied to multiphase flows with one-way coupling. In other words, the study investigates the effect of carrier phase discretization on the dispersed phase solution. In contrast, future studies could focus on doing the opposite, i.e., investigating the effect of dispersed phase discretization on the carrier phase solution. This would especially be important when the volumetric fraction of the dispersed phase is large enough for two-way coupling or higher. Alternatively, the present study could be improved by evaluating the mixed polynomial extrapolation method using test cases from various other categories of multiphase flows where the dispersed phase solution is of significance, such as gas-droplet flows and particle deposition effects in gas turbines.

6.2 Performance Analysis of Supersonic Intakes

The goal of this study was to provide a fundamental assessment of nanoparticle injection on the intake performance. Therefore, CFD simulations were conducted using the slip flow boundary conditions to eliminate the complex behavior of shockwave-boundary-layer-particle interactions. Moving forward, future studies could be focused on improving the accuracy of CFD predictions by including a no-slip boundary condition for the walls.

6.3   Stability Analysis of Supersonic Intakes

Future studies in the field of supersonic intake stability can focus on determining the combination of input parameters such as the injection location and angle, Stokes number, particle Eckert number, thermal transport number and particle mass loading ratio, which would eliminate the vortex sheet and particle induced separation regions, which were found to be the two sources of instabilities in this study. Furthermore, particle injection can be tested for *big-buzz*, which is known to be caused by the SBLIs. This could be done by using a no-slip boundary condition at the intake walls, as well as identifying the appropriate turbulence model to accuately resolve the physics of SBLIs.

Bibliography

Amano, R. S., Yen, Y.-H., Miller, T. C., Ebnit, A., Lightfoot, M., and Sankaran, V. (2016). Study of the liquid breakup process in solid rocket motor. *Journal of Spacecraft and Rockets*, 53(5):980–992.

Anderson, J. D. and Wendt, J. (1995). *Computational fluid dynamics*. Springer.

Anderson, W. E. and Wong, N. D. (1970). Experimental investigation of a large scale, two-dimensional, mixed-compression inlet system: Performance at design conditions at a mach number of 3.0. *NASA TM X-2016*.

Arisman, C., Johansen, C., Bathel, B., and Danehy, P. (2015). Investigation of gas seeding for planar laser-induced fluorescence in hypersonic boundary layers. *AIAA Journal*, 53(12):3637–3651.

Auslender, A., Suder, K., and Thomas, S. (2009). An overview of the NASA FAP hypersonics project airbreathing propulsion research. In *16th AIAA/DLR/DGLR International Space Planes and Hypersonic Systems and Technologies Conference*, page 7277.

Billig, F. S. (1995). Supersonic combustion ramjet missile. *Journal of Propulsion and Power*, 11(6):1139–1146.

Blinde, P. L., Humble, R. A., Van Oudheusden, B. W., and Scarano, F. (2009). Effects of micro-ramps on a shock wave/turbulent boundary layer interaction. *Shock Waves*, 19(6):507.

Bobashev, S. V., Erofeev, A. V., Lapushkina, T. A., Poniaev, S. A., Vasil'eva, R. V., and Van Wie, D. M. (2005). Effect of magnetohydrodynamics interaction in various parts of diffuser on inlet shocks: Experiment. *Journal of Propulsion and Power*, 21(5):831–837.

Brady, P. T., Herrmann, M., and Lopez, J. M. (2012). Code verification for finite volume multiphase

scalar equations using the method of manufactured solutions. *Journal of Computational Physics*, 231(7):2924–2944.

Brock, J. R. (1962). On the theory of thermal forces acting on aerosol particles. *Journal of Colloid Science*, 17(8):768–780.

Brown, M., Mudford, N., Neely, A., and Tapabrata, R. (2006). Robust design optimization of two-dimensional scramjet inlets. In *14th AIAA/AHI Space Planes and Hypersonic Systems and Technologies Conference*, page 8140.

Carlson, D. J. (1965). Experimental determination of velocity lag in gas-particle nozzle flows. *AIAA Journal*, 3(2):354–357.

Carlson, D. J. and Hoglund, R. F. (1964). Particle drag and heat transfer in rocket nozzles. *AIAA Journal*, 2(11):1980–1984.

Carrier, G., Knight, D., Rasheed, K., and Montazel, X. (2001). Multi-criteria design optimization of two-dimensional supersonic inlet. In *39th AIAA Aerospace Sciences Meeting and Exhibit, Reno, NV*, page 1064.

Chamberlain, R. (1992). Computation of film cooling characteristics in hypersonic flow. In *AIAA Materials Specialist Conference-Coating Technology for Aerospace Systems*, page 657.

Chang, I.-S. (1980). One-and two-phase nozzle flows. *AIAA Journal*, 18(12):1455–1461.

Chang, I.-S. (1983). Three dimensional, two-phase supersonic nozzle flows. *AIAA Journal*, 21(5):671–678.

Chang, I.-S. (1990). Three-dimensional, two-phase, transonic, canted nozzle flows. *AIAA journal*, 28(5):790–797.

Chen, H., Tan, H.-J., Zhang, Q.-F., and Zhang, Y. (2017). Buzz flows in an external-compression inlet with partially isentropic compression. *AIAA Journal*, 55(12):4286–4295.

Chen, H., Tan, H.-J., Zhang, Q.-F., and Zhang, Y. (2018). Throttling process and buzz mechanism of a supersonic inlet at overspeed mode. *AIAA Journal*, 56(5):1953–1964.

Choudhary, A. and Roy, C. J. (2018). Verification and validation for multiphase flows. *Handbook of Multiphase Flow Science and Technology*, pages 1–37.

Choudhary, A., Roy, C. J., Dietiker, J.-F., Shahnam, M., Garg, R., and Musser, J. (2016). Code verification for multiphase flows using the method of manufactured solutions. *International Journal of Multiphase Flow*, 80:150–163.

Crowe, C. T. (1982). Numerical models for dilute gas-particle flows. *Journal of Fluids Engineering*, 104(3):297–303.

Crowe, C. T. and Willoughby, P. G. (1966). A mechanism for particle growth in a rocket nozzle. *AIAA Journal*, 4(9):1677–1678.

Curran, E. T. (2001). Scramjet engines: the first forty years. *Journal of Propulsion and Power*, 17(6):1138–1148.

Curran, E. T. and Murthy, S. N. B. (1991). *High-speed flight propulsion systems*. AIAA.

Dailey, C. L. (1955). Supersonic diffuser instability. *Journal of the Aeronautical Sciences*, 22(11):733–749.

Daines, R. and Segal, C. (1998). Combined rocket and airbreathing propulsion systems for space-launch applications. *Journal of Propulsion and Power*, 14(5):605–612.

Dalle, D., Torrez, S., and Driscoll, J. (2011). Performance analysis of variable-geometry scramjet inlets using a low-order model. In *47th AIAA/ASME/SAE/ASEE Joint Propulsion Confrence and Exhibit*, page 5756.

Daniel, E., Loraud, J. C., Larini, M., and Saurel, R. (1994). Cooling of a gaseous nozzle flow by injection of liquid droplets. *Mechanics research communications*, 21(6):635–644.

Dass, P., Johansen, C., Jagannathan, R., and Trivedi, M. (2017). Precooled airbreathing engine. *Patent*, (PCT/CA2016/051289).

de la Mora, J. F., Hering, S., Rao, N., and McMurry, P. (1990). Hypersonic impaction of ultrafine particles. *Journal of Aerosol Science*, 21(2):169–187.

Deen, N. G., Annaland, M. V. S., Van der Hoef, M. A., and Kuipers, J. A. M. (2007). Review of discrete particle modeling of fluidized beds. *Chemical engineering science*, 62(1-2):28–44.

Delery, J. M. (1985). Shock wave/turbulent boundary layer interaction and its control. *Progress in Aerospace Sciences*, 22(4):209–280.

Dykhuizen, R. C. and Smith, M. F. (1998). Gas dynamic principles of cold spray. *Journal of Thermal Spray Technology*, 7(2):205–212.

Eckert, E. R. G. (1956). Engineering relations for heat transfer and friction in high-velocity laminar and turbulent boundary-layer flow over surfaces with constant pressure and temperature. *Transactions of the ASME*, 78(6):1273–1283.

Eckert, E. R. G., Goldstein, R. J., Haji-Sheikh, A., and Tsou, F. K. (1966). Film cooling with air and helium injection through a rearward-facing slot into a supersonic air flow. *AIAA Journal*, 4(6):981–985.

Elghobashi, S. (1994). On predicting particle-laden turbulent flows. *Applied Scientific Research*, 52(4):309–329.

Fan, L.-S. and Zhu, C. (2005). *Principles of gas-solid flows*. Cambridge University Press.

Ferri, A. and Nucci, L. M. (1951). The origin of aerodynamic instability of supersonic inlets at subcritical conditions. *NACA RM-L50K30*.

Fisher, S. A., Neale, M. C., and Brooks, A. J. (1970). *On the sub-critical stability of variable ramp intakes at mach numbers around 2*. National Gas Turbine Establishment ARC/R&M-3711.

Flaherty, K. W., Andrews, K. M., and Liston, G. W. (2010). Operability benefits of airbreathing hypersonic propulsion for flexible access to space. *Journal of Spacecraft and Rockets*, 47(2):280–287.

Forde, M. (1986). Quasi-one-dimensional gas/particle nozzle flows with shock. *AIAA Journal*, 24(7):1196–1199.

Fujiwara, H., Murakami, A., and Watanabe, Y. (2002). Numerical analysis on shock oscillation of two-dimensional external compression intakes. In *32nd AIAA Fluid Dynamics Conference and Exhibit*, page 2740.

Fukuda, M. K., Hingst, W. G., and Reshotko, E. (1975). *Control of shock wave-boundary layer interactions by bleed in supersonic mixed compression inlets*. NASA CR-2595.

Gaiddon, A. and Knight, D. (2003). Multicriteria design optimization of integrated three-dimensional supersonic inlets. *Journal of Propulsion and Power*, 19(3):456–463.

Gaiddon, A., Knight, D., and Poloni, C. (2004). Multicriteria design optimization of a supersonic inlet based upon global missile performance. *Journal of Propulsion and Power*, 20(3):542–558.

Goroshin, S., Higgins, A., and Kamel, M. (2001). Powdered metals as fuels for hypersonic ramjets. *37th Joint Propulsion Conference and Exhibit*, page 3919.

Greenfield, B., Louisos, W., and Hitt, D. (2011). Numerical simulations of multiphase flow in supersonic micro-nozzles. In *49th AIAA Aerospace Sciences Meeting including the New Horizons Forum and Aerospace Exposition*, page 189.

Greenshields, C. J., Weller, H. G., Gasparini, L., and Reese, J. M. (2010). Implementation of semi-discrete, non-staggered central schemes in a colocated, polyhedral, finite volume framework, for high-speed viscous flows. *International Journal for Numerical Methods in Fluids*, 63(1):1–21.

Harloff, G. J. and Smith, G. E. (1996). Supersonic-inlet boundary-layer bleed flow. *AIAA Journal*, 34(4):778–785.

Heiser, W. H. and Pratt, D. T. (1994). *Hypersonic airbreathing propulsion*. AIAA.

Herrmann, D. and Gülhan, A. (2014). Experimental analyses of inlet characteristics of an airbreathing missile with boundary-layer bleed. *Journal of Propulsion and Power*, 31(1):170–179.

Herrmann, D., Siebe, F., and Gülhan, A. (2013). Pressure fluctuations (buzzing) and inlet performance of an airbreathing missile. *Journal of Propulsion and Power*, 29(4):839–848.

Heufer, K. A. and Olivier, H. (2006). Film cooling of an inclined flat plate in hypersonic flow. In *14th AIAA/AHI Space Planes and Hypersonic Systems and Technologies Conference*, page 8067.

Hinman, W. S. (2017). *Laminar Near Wake of Hypersonic Blunt Bodies*. PhD thesis, University of Calgary.

Hinman, W. S. and Johansen, C. (2016a). Interaction theory of hypersonic laminar near-wake flow behind an adiabatic circular cylinder. *Shock Waves*, 26(6):717–727.

Hinman, W. S. and Johansen, C. (2016b). Rapid prediction of hypersonic blunt body flows for parametric design studies. *Aerospace Science and Technology*, 58:48–59.

Ho, C.-M. and Nosseir, N. S. (1981). Dynamics of an impinging jet. Part 1. The feedback phenomenon. *Journal of Fluid Mechanics*, 105:119–142.

Hoglund, R. F. (1962). Recent advances in gas-particle nozzle flows. *ARS Journal*, 32(5):662–671.

Hwang, C. J. and Chang, G. C. (1988). Numerical study of gas-particle flow in a solid rocket nozzle. *AIAA Journal*, 26(6):682–689.

Ibsen, C. H., Helland, E., Hjertager, B. H., Solberg, T., Tadrist, L., and Occelli, R. (2004). Comparison of multifluid and discrete particle modelling in numerical predictions of gas particle flow in circulating fluidised beds. *Powder Technology*, 149(1):29–41.

Jagannathan, R., Hinman, W. S., and Johansen, C. (2019a). Performance assessment of supersonic and hypersonic intake systems with nano-particle injection. *Acta Astronautica*, 159:609–621.

Jagannathan, R., Hinman, W. S., and Johansen, C. (2019b). Solution verification of multiphase flows with one-way coupling. *Journal of Computational Physics*, 402:109033.

Jagannathan, R. and Johansen, C. (2019). Numerical assessment of intake buzz with nano-particles across a supersonic external compression intake. In *AIAA Propulsion and Energy 2019 Forum*, page 4425.

Jasak, H. (1996). *Error Analysis and Estimation for the Finite Volume Method with Applications to Fluid Flows*. PhD thesis, Imperial College of Science, Technology and Medicine.

Jivraj, F., Bond, A., Varvill, R., and Paniagua, G. (2007). The Scimitar pre-cooled Mach 5 engine. 2nd European Conference for Aerospace Sciences.

Jolgam, S. A., Ballil, A. R., Nowakowski, A. F., and Nicolleau, F. C. (2012). Simulations of compressible multiphase flows through a tube of varying cross-section. In *ASME 2012 11th Biennial Conference on Engineering Systems Design and Analysis*, pages 101–110.

Kantrowitz, A. and Donaldson, C. D. (1945). *Preliminary investigation of supersonic diffusers*. NACA WR L-713.

Kestin, J. and Wood, R. (1970). The mechanism which causes free stream turbulence to enhance stagnation line heat and mass transfer. *4th International Heat Transfer Conference*, page 27.

Kurganov, A., Noelle, S., and Petrova, G. (2001). Semidiscrete central-upwind schemes for hyperbolic conservation laws and Hamilton-Jacobi equations. *SIAM Journal on Scientific Computing*, 23(3):707–740.

Kurganov, A. and Tadmor, E. (2000). New high-resolution central schemes for nonlinear conservation laws and convection–diffusion equations. *Journal of Computational Physics*, 160(1):241–282.

Lear, W. E. and Sherif, S. A. (1997). Two-phase non-dissipative supersonic nozzle flow analysis for maximum condensed phase momentum flux. *Acta Astronautica*, 40(10):707–712.

Lear, W. E., Sherif, S. A., and Langford, J. R. (1997). Efficiency and gas dynamic analysis of two-phase mixtures in supersonic nozzles with inter-phase heat transfer and slip. *Acta Astronautica*, 40(10):701–706.

Lee, H. J., Lee, B. J., Kim, S. D., and Jeung, I.-S. (2011). Flow characteristics of small-sized supersonic inlets. *Journal of Propulsion and Power*, 27(2):306–318.

Li, X. and Bai, B. (2014). Motion of submicron particles in supersonic laminar boundary layers. *AIAA Journal*, 53(4):1037–1047.

Ling, Y., Balachandar, S., and Parmar, M. (2016). Inter-phase heat transfer and energy coupling in turbulent dispersed multiphase flows. *Physics of Fluids*, 28(3):033304.

Ling, Y., Haselbacher, A., and Balachandar, S. (2011a). Importance of unsteady contributions to force and heating for particles in compressible flows. Part 1: Modeling and analysis for shock–particle interaction. *International Journal of Multiphase Flow*, 37(9):1026–1044.

Ling, Y., Haselbacher, A., and Balachandar, S. (2011b). Importance of unsteady contributions to force and heating for particles in compressible flows. Part 2: Application to particle dispersal by blast waves. *International Journal of Multiphase Flow*, 37(9):1013–1025.

Ling, Y., Parmar, M., and Balachandar, S. (2013). A scaling analysis of added-mass and history forces and their coupling in dispersed multiphase flows. *International Journal of Multiphase Flow*, 57:102–114.

Liu, Z., Bi, Q., Guo, Y., Ma, X., and Zhao, S. (2012). Thermal induced static flow instability of hydrocarbon fuel in the regeneratively cooled structures of hypersonic vehicles. In *18th AIAA/3AF International Space Planes and Hypersonic Systems and Technologies Conference*, page 5859.

Loth, E. (2000). Numerical approaches for motion of dispersed particles, droplets and bubbles. *Progress in Energy and Combustion Science*, 26(3):161–223.

Lu, P.-J. and Jain, L.-T. (1998). Numerical investigation of inlet buzz flow. *Journal of Propulsion and Power*, 14(1):90–100.

Macheret, S. O., Shneider, M. N., and Miles, R. B. (2004). Scramjet inlet control by off-body energy addition: a virtual cowl. *AIAA Journal*, 42(11):2294–2302.

Mahoney, J. J. (1990). *Inlets for supersonic missiles*. AIAA.

McCormick, D. C. (1993). Shock/boundary-layer interaction control with vortex generators and passive cavity. *AIAA Journal*, 31(1):91–96.

Melis, M. and Wang, W.-P. (1999). Multiphysics simulation of active hypersonic cowl lip cooling. In *30th Fluid Dynamics Conference*, page 3510.

Miller, E. (1975). Alumina particle velocity and temperature in a solid rocket plume. *AIAA Journal*, 13(12):1668–1670.

Moradian, N. and Timofeev, E. (2017). Starting characteristics of Prandtl–Meyer scramjet intakes with overboard spillage. *Journal of Propulsion and Power*, 34(1):189–197.

Musgrove, G. O., Barringer, M. D., Thole, K. A., Grover, E., and Barker, J. (2009). Computational design of a louver particle separator for gas turbine engines. In *ASME Turbo Expo 2009: Power for Land, Sea, and Air*, pages 1313–1323. American Society of Mechanical Engineers.

Musser, J. and Choudhary, A. (2015). MFIX documentation, volume 3: Verification and validation manual.

Nagashima, T., Obokata, T., and Asanuma, T. (1972). *Experiment of supersonic air intake buzz*. Institute of Space and Aeronautical Science, University of Tokyo.

Nishida, M. and Ishimaru, S. (1990). Numerical analysis of gas-solid two-phase non-equilibrium nozzle flows. *JSME Jnternational Journal*, 33(3):494–500.

Oberkampf, W. L. and Roy, C. J. (2010). *Verification and validation in scientific computing*. Cambridge University Press.

Oberkampf, W. L. and Trucano, T. G. (2002). Verification and validation in computational fluid dynamics. *Progress in Aerospace Sciences*, 38(3):209–272.

Ogawa, H., Grainger, A. L., and Boyce, R. R. (2010). Inlet starting of high-contraction axisymmetric scramjets. *Journal of Propulsion and Power*, 26(6):1247–1258.

Owens, L. R., Allan, B. G., and Gorton, S. A. (2008). Boundary-layer-ingesting inlet flow control. *Journal of Aircraft*, 45(4):1431–1440.

Perchonok, E. and Wilcox, F. (1956). *Preliminary attempts at isothermal compression of a supersonic air stream*. NACA RM E55 129.

Persson, S. (2017). *Development of a Test Suite for Verification & Validation of OpenFOAM*. PhD thesis, Chalmers University of Technology.

Qin, J., Bao, W., Zhou, W., and Yu, D. (2009). Performance cycle analysis of an open cooling cycle for a scramjet. *Proceedings of the Institution of Mechanical Engineers, Part G: Journal of Aerospace Engineering*, 223(6):599–607.

Ran, H. and Mavris, D. (2005). Preliminary design of a 2D supersonic inlet to maximize total pressure recovery. In *AIAA 5th Aviation, Technology, Integration and Operations Conference, Virginia*, page 7357.

Richards, B. and Stollery, J. (1977). An experimental study of the cooling effectiveness of a laminar two-dimensional tangential film in hypersonic flow. In *10th Fluid and Plasmadynamics Conference*, page 703.

Richardson, L. F. (1911). The approximate arithmetical solution by finite differences of physical problems involving differential equations, with an application to the stresses in a masonry dam. *Philosophical Transactions of the Royal Society of London. Series A, Containing Papers of a Mathematical or Physical Character*, 210:307–357.

Richardson, L. F. and Gaunt, J. A. (1927). The deferred approach to the limit. Part I. Single lattice. Part II. Interpenetrating lattices. *Philosophical Transactions of the Royal Society of London. Series A, containing papers of a mathematical or physical character*, 226:299–361.

Ripplinger, S. (2013). *Development of a coupled fluid and colloidal particle transport model*. PhD thesis, Utah State University.

Roache, P. J. (1997). Quantification of uncertainty in computational fluid dynamics. *Annual Review of Fluid Mechanics*, 29(1):123–160.

Roache, P. J. (1998). *Verification and validation in computational science and engineering*. Hermosa Publishers.

Roy, C. J. (2003). Grid convergence error analysis for mixed-order numerical schemes. *AIAA Journal*, 41(4):595–604.

Roy, C. J. (2005). Review of code and solution verification procedures for computational simulation. *Journal of Computational Physics*, 205(1):131–156.

Roy, C. J. and Blottner, F. G. (2001). Assessment of one-and two-equation turbulence models for hypersonic transitional flows. *Journal of Spacecraft and Rockets*, 38(5):699–710.

Rudinger, G. (1970). Gas-particle flow in convergent nozzles at high loading ratios. *AIAA Journal*, 8(7):1288–1294.

Rudinger, G. (2012). *Fundamentals of gas particle flow*, volume 2. Elsevier.

Saffman, P. G. T. (1965). The lift on a small sphere in a slow shear flow. *Journal of Fluid Mechanics*, 22(02):385–400.

Schetz, J. A. and Bowersox, R. D. W. (2011). *Boundary layer analysis*. AIAA.

Schwarzkopf, J. D., Sommerfeld, M., Crowe, C. T., and Tsuji, Y. (2011). *Multiphase flows with droplets and particles*. CRC press.

Seddon, J. and Goldsmith, E. L. (1999). *Intake aerodynamics*. AIAA.

Shahnam, M., Gel, A., Dietiker, J.-F., Subramaniyan, A. K., and Musser, J. (2016). The effect of grid resolution and reaction models in simulation of a fluidized bed gasifier through nonintrusive uncertainty quantification techniques. *Journal of Verification, Validation and Uncertainty Quantification*, 1(4):041004.

Shang, J. S. and Surzhikov, S. T. (2005). Magnetoaerodynamic actuator for hypersonic flow control. *AIAA Journal*, 43(8):1633–1652.

Shapiro, A. H. (1953). *The dynamics and thermodynamics of compressible fluid flow, Vol. 1*. Ronald Press, New York.

Sherif, S. A., Lear, W. E., and Winowich, N. S. (1994). Effect of slip velocity and heat transfer on the condensed phase momentum flux of supersonic nozzle flows (no. conf-940659-). Technical report, American Society of Mechanical Engineers, New York, NY (United States).

Shneider, M. and Macheret, S. (2005). Hypersonic aerodynamic control and thrust vectoring by nonequilibrium cold-air MHD devices. In *43rd AIAA Aerospace Sciences Meeting and Exhibit*, page 979.

Smart, M. K. (1999). Optimization of two-dimensional scramjet inlets. *Journal of Aircraft*, 36(2):430–433.

Smart, M. K. and Tetlow, M. R. (2009). Orbital delivery of small payloads using hypersonic airbreathing propulsion. *Journal of Spacecraft and Rockets*, 46(1):117–125.

Soltani, M. R., Daliri, A., Younsi, J. S., and Farahani, M. (2016). Effects of bleed position on the stability of a supersonic inlet. *Journal of Propulsion and Power*, 32(5):1153–1166.

Soltani, M. R. and Farahani, M. (2013). Experimental investigation of effects of mach number on the flow instability in a supersonic inlet. *Experimental Techniques*, 37(3):46–54.

Soltani, M. R., Farahani, M., and Younsi, J. S. (2011). Performance study of a supersonic inlet in the presence of a heat source. *Scientia Iranica*, 18(3):375–382.

Sorensen, N. E., Latham, E. A., and Smeltzer, D. B. (1976). Variable geometry for supersonic mixed-compression inlets. *Journal of Aircraft*, 13(4):309–312.

Sutton, G. P. and Biblarz, O. (2010). *Rocket propulsion elements*. John Wiley & Sons.

Taguchi, H., Kobayashi, H., Kojima, T., Hongoh, M., Masaki, D., and Nishida, S. (2015). Performance evaluation of hypersonic pre-cooled turbojet engine. In *20th AIAA International Space Planes and Hypersonic Systems and Technologies Conference*, page 3593.

Talcott, N. and Kumar, A. (1985). Two-dimensional viscous simulation of inlet/diffuser flows with terminal shocks. *Journal of Propulsion and Power*, 1(2):103–108.

Tedeschi, G., Gouin, H., and Elena, M. (1992). Solution of the equation of particle motion across a shock wave. *La Recherche Aerospatiale(English Edition)*, (6):1–9.

Tedeschi, G., Gouin, H., and Elena, M. (1999). Motion of tracer particles in supersonic flows. *Experiments in Fluids*, 26:288–296.

Teh, E. J. and Johansen, C. (2016). Effect of particle momentum transfer on an oblique-shock-wave/laminar-boundary-layer interaction. *Acta Astronautica*, 128:431–439.

Trapier, S., Deck, S., and Duveau, P. (2008). Delayed detached-eddy simulation of supersonic inlet buzz. In *Advances in Hybrid RANS-LES Modelling*, pages 242–251. Springer.

Trapier, S., Deck, S., Duveau, P., and Sagaut, P. (2007). Time-frequency analysis and detection of supersonic inlet buzz. *AIAA Journal*, 45(9):2273–2284.

Trapier, S., Duveau, P., and Deck, S. (2006). Experimental study of supersonic inlet buzz. *AIAA Journal*, 44(10):2354–2365.

Vasenin, I. M., Narimanov, R. K., Glazunov, A. A., Kuvshinov, N. E., and Ivanov, V. A. (1995). Two-phase flows in the nozzles of solid rocket motors. *Journal of Propulsion and Power*, 11(4):583–592.

Veillard, X., Tahir, R., Timofeev, E., and Molder, S. (2008). Limiting contractions for starting simple ramp-type scramjet intakes with overboard spillage. *Journal of Propulsion and Power*, 24(5):1042–1049.

Verma, S. B. and Manisankar, C. (2012). Shockwave/boundary-layer interaction control on a compression ramp using steady microjets. *AIAA Journal*, 50(12):2753–2764.

Williams, W. C. (2015). Gas-based nanofluids (nanoaerosols). In *Heat Transfer Enhancement with Nanofluids*, pages 453–469. CRC Press.

Yamamoto, J., Kojima, Y., Kameda, M., Watanabe, Y., Hashimoto, A., and Aoyama, T. (2019). Prediction of the onset of supersonic inlet buzz. *Aerospace Science and Technology*, 96:105523.

Yan, H. and Gaitonde, D. (2011). Parametric study of pulsed thermal bumps in supersonic boundary layer. *Shock Waves*, 21(5):411–423.

Yang, L., Erdem, E., and Kontis, K. (2010). Flow control using thermal bumps in hypersonic flows. In *48th AIAA Aerospace Sciences Meeting Including the New Horizons Forum and Aerospace Exposition*, page 1098.

Yang, W.-C. (2003). *Handbook of fluidization and fluid-particle systems*. CRC press.

Yu, Y. and Liu, S. (2007). Simulation of two phase viscous flows in a solid rocket motor. In *New Trends in Fluid Mechanics Research*, pages 586–589. Springer.

Zhang, G. and Kim, H. D. (2018). Theoretical and numerical analysis on choked multiphase flows of gas and solid particle through a convergent–divergent nozzle. *The Journal of Computational Multiphase Flows*, 10(1):19–32.

Zhang, K., Yu, S., and Peng, C. (1983). Effect of a shear layer on stability of an axisymmetric external compression air intake. *Acta Aeronautica et Astronautica Sinica*, 4:56–62.

Zhang, S., Qin, J., Bao, W., and Zhang, L. (2014). Numerical analysis of supersonic film cooling in supersonic flow in hypersonic inlet with isolator. *Advances in Mechanical Engineering*, 6:468790.

Zhao, Z., Li, J.-M., Zheng, J., Cui, Y., and Khoo, B. C. (2014). Study of shock and induced flow dynamics by nanosecond dielectric-barrier-discharge plasma actuators. *AIAA Journal*, 53(5):1336–1348.

Appendix A

Order of Magnitude Analysis of Interphase Momentum and Energy Sources in Compressible Gas-Nanoparticle Flows

An order of magnitude analyses of energy and momentum source terms were conducted. The following analysis assesses the relative time scales of the relevant force and energy transfer terms for gas-particle flows. Spherical, solid nano-particles ($10\,\text{nm} < D_p < 10\,\mu\text{m}$) of Boron are suspended in a high-speed compressible flow of air through a channel/intake of length, L. The following list describes the scaling arguments used in the time scale analysis. Scalar notations have been used for time scale calculations:

1. The gas velocity (V) scales with the freestream reference value (V_∞).

2. The particle velocity (V_p) scales with the particle injection velocity ($V_{p\infty}$).

3. The relative velocity ($V_r = V - V_p$) scales with the term, ($V_\infty - V_{p\infty}$).

4. The axial length variable (x) scales with the channel/duct length (L).

5. The cross-sectional length variable (y), scales with the channel/duct diameter (D) for inviscid flows/regions, and with the boundary layer thickness (δ) at the boundary layers; $\delta \sim L/Re_L^{0.5}$, where Re_L is the Reynolds number based on the channel/duct length (L) and gas velocity (V).

6. For supersonic duct/channel flows that involve compression such as the intake, the gas entering at a high-speed-low-temperature state is compressed to a low-speed-high-temperature state. In such cases, the gas temperature, T, scales with the term, ($T_{0\infty} - T_\infty$). A particle temperature with $T_p \sim T$, will also scale with the term, ($T_{0\infty} - T_\infty$).

7. The flow time scale, τ_f, is defined by

$$\tau_f = \frac{L}{V_\infty} \tag{A.1}$$

8. The time scale of a source term, τ, is represented by

$$\frac{d\psi_p}{dt} = \frac{1}{\tau}(\psi - \psi_p) \tag{A.2}$$

where ψ is velocity/temperature, and the subscript p denote the particle variable.

A.1 Momentum Transfer

The generalized momentum equation for a single particle dispersed in a fluid flow is given by (Loth, 2000; Schwarzkopf et al., 2011)

$$m_p \frac{d\mathbf{V}_p}{dt} = \Sigma \mathbf{F}_p = \mathbf{F}_D + \mathbf{F}_{gr} + \mathbf{F}_L + \mathbf{F}_U + \mathbf{F}_{th} \tag{A.3}$$

where the variable, $\mathbf{F}_p$, denotes the forces acting on a particle, and $\mathbf{F}_D$, $\mathbf{F}_{gr}$, $\mathbf{F}_L$, $\mathbf{F}_U$, and $\mathbf{F}_{th}$ represent the aerodynamic drag, gravitational, lift, unsteady, and thermophoretic forces. The variable, m_p, represents the mass of a single particle, and $\mathbf{V}_p$ is the particle velocity. The forces associated with unsteady particle acceleration/deceleration are the Basset history and added mass forces. The effect of both of these forces depends on the density ratio, ρ/ρ_p (Fan and Zhu, 2005; Rudinger, 2012). Tedeschi et al. (1992) found the Basset history force to be negligible for a single particle moving across a shockwave when $\rho/\rho_p = 10^{-2}$. In the present study, $\rho/\rho_p < 10^{-4}$. Hence, the unsteady force terms have been neglected. In addition to the above forces, the particle experiences an impulse when it moves across a shockwave, due to the pressure jump across the shock. A simple theoretical assessment of this impulse was conducted for a gas-particle system across the shock. It was found that the effect was found to be negligible within the range of mass loading ratio used in this study. However, a deeper look into this source of momentum transfer will be required at higher particle mass loadings.

A.1.1 Aerodynamic Drag Force

The presence of a non-zero relative velocity between the gas and a particle induces drag. The aerodynamic drag force for a sphere is expressed by

$$\mathbf{F}_D = \frac{\pi D_p^2}{8} \rho C_D |\mathbf{V} - \mathbf{V}_p| (\mathbf{V} - \mathbf{V}_p) \tag{A.4}$$

where C_D is defined as the aerodynamic drag coefficient, ρ is the gas density, D_p is the particle diameter, and $\mathbf{V}$ is the gas velocity. The aerodynamic drag time scale for a Knudsen particle is given by Eq. A.5 (Williams, 2015).

$$\tau_D \sim \frac{\rho_p D_p^2}{18\mu} k \tag{A.5}$$

where k is the Cunningham correction factor, which is given by

$$k = 1 + (Kn_p) \left[\alpha + \beta e^{-\gamma/(Kn_p)} \right] \tag{A.6}$$

where $\alpha \sim 2.34$, $\beta \sim 1.05$ and $\gamma \sim -0.39$.

A.1.2 Lift Force

The lift force has two components: shear-induced lift (Saffman force) and spin-induced lift (Magnus force) (Loth, 2000). The Saffmann lift is generated in the presence of a (relative) velocity gradient around a particle. The expression for the shear-induced lift, $\mathbf{F}_L$, is described by (Fan and Zhu, 2005; Saffman, 1965)

$$\mathbf{F}_L = \left[\frac{6.46}{4} \mu D_p^2 |\mathbf{V} - \mathbf{V}_p| \sqrt{\frac{1}{\nu} |\nabla (\mathbf{V} - \mathbf{V}_p)|} \right] \frac{\nabla (\mathbf{V} - \mathbf{V}_p)}{|\nabla (\mathbf{V} - \mathbf{V}_p)|} \tag{A.7}$$

where μ and ν are the dynamic and kinematic viscosities, respectively.

The Magnus force can be considered to be negligible when compared to the aerodynamic drag force and shear induced lift at lower particle Reynolds numbers (Re_p), smaller particle sizes, and lower spin velocities (Fan and Zhu, 2005; Saffman, 1965). Since $Re_p \ll 1$ in the present study,

the Magnus force has been neglected. By applying the scaling arguments for the cross-sectional length variable ($y \sim L/\sqrt{Re_L}$ and $y \sim D$, with and without boundary layers, respectively) and relative velocity ($V_r \sim (V_\infty - V_{p\infty})$), the time scale for the Saffman lift force is given by Eq. A.8 at the boundary layers, and by Eq. A.9 for the inviscid flow/region.

$$\tau_L \sim \frac{\rho_p D_p}{3.08\mu} \sqrt{\frac{\nu L}{(V_\infty - V_{p\infty})\sqrt{Re_L}}} \tag{A.8}$$

$$\tau_L \sim \frac{\rho_p D_p}{3.08\mu} \sqrt{\frac{\nu D}{(V_\infty - V_{p\infty})}} \tag{A.9}$$

A.1.3 Gravitational Force

The gravitational force is obtained by

$$\mathbf{F}_{gr} = m_p \mathbf{g} \tag{A.10}$$

where $\mathbf{g}$ is the acceleration due to gravity. The time scale for gravity is given by Eq. A.11.

$$\tau_{gr} \sim \frac{V_\infty - V_{p\infty}}{g} \tag{A.11}$$

A.1.4 Thermophoretic Force

One of the most commonly used expressions for the thermophoretic force, $\mathbf{F}_{th}$, was developed by Brock (Brock, 1962), which is described by

$$\mathbf{F}_{th} = -6\pi\mu\nu D_p C_s \frac{1}{1+6C_m(Kn_p)} \frac{\frac{\kappa_s}{\kappa_p}+2C_t(Kn_p)}{1+2\frac{\kappa_s}{\kappa_p}+4C_t(Kn_p)} \frac{1}{T}\nabla T \tag{A.12}$$

where C_s, C_t, and C_m are known as the thermal slip coefficient, thermal exchange coefficient, and momentum exchange coefficient, respectively. Additionally, Kn_p is the particle Knudsen number, κ_s and κ_p represent the thermal conductivities of the gas (calculated at the particle surface) and

particle, respectively. By introducing the scaling arguments for the axial length variable $(x \sim L)$ and gas temperature $(T \sim (T_{0\infty} - T_{\infty}))$, the thermophoretic time scale is given by Eq. A.13.

$$\tau_{\text{th}} \sim \frac{\rho_p D_p^2 L (V_{\infty} - V_{p\infty})}{36\lambda \mu \nu} \tag{A.13}$$

where

$$\lambda = \left[\frac{C_s}{1 + 6C_m(Kn_p)} \right] \left[\frac{\frac{\kappa_s}{\kappa_p} + 2C_t(Kn_p)}{1 + 2\frac{\kappa_s}{\kappa_p} + 4C_t(Kn_p)} \right] \tag{A.14}$$
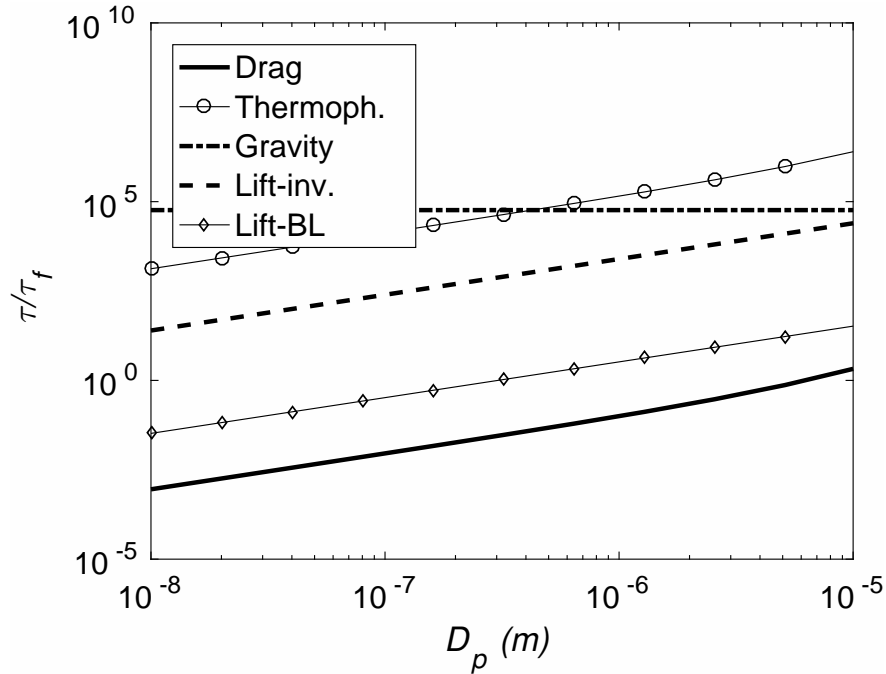

Figure A.1: Time-scale comparisons between the drag, Saffman lift (at the inviscid region and boundary layers), thermophoretic and gravitational forces, when $M_{\infty} = 2.5$, $L \sim 1$ m and calculated using the conditions for an altitude of $30\,\text{km}$

The time scale ratios of drag, lift, thermophoresis, and gravity are plotted in Fig. A.1. Momentum transfer through the drag force occurs much quicker than all the other forces. The Saffman lift becomes comparable to the flow time scale at the boundary layers $(\tau_L/\tau_f < 1)$. But, when compared to drag, it trails by almost two orders of magnitude. The drag also dominates over thermophoretic and gravitational forces by several orders of magnitude. Hence, in the present study, aerodynamic drag has been considered to be the only mechanism for momentum transfer.

A.2 Heat Transfer

Heat transfer between the gas and particle occurs through convection and radiation at the particle surface and gets distributed within the particle through conduction.

A.2.1 Convective Heat Transfer

The energy transfer equation across a particle surface by convection is described by

$$m_p C_{pp} \frac{dT_p}{dt} = h_p A_p (T - T_p) \tag{A.15}$$

where h_p is the convective heat transfer coefficient, A_p denotes the particle surface area, and C_{pp} is the specific heat of the particle. The time scale for convection is estimated by (Williams, 2015)

$$\tau_{\text{conv}} = \frac{\rho_p D_p C_{pp}}{6 h_p} \tag{A.16}$$

A.2.2 Radiation

The energy transfer equation for a particle due to thermal radiation is described using the Stefan-Boltzmann law, which is given by (assuming black body)

$$m_p C_{pp} \frac{dT_p}{dt} = \sigma A_p (T^4 - T_p^4) \tag{A.17}$$

where σ is the Stefan-Boltzmann constant. The radiation time scale (Eq. A.19) is obtained by linearizing the expression in Eq. A.18, and by applying the scaling arguments for the gas temperature $(T \sim (T_{0\infty} - T_\infty))$.

$$T^4 - T_p^4 \approx 4T^3 (T - T_p) \tag{A.18}$$

$$\tau_{\text{rad}} \sim \frac{\rho_p D_p C_{pp}}{6 \sigma (T_{0\infty} - T_\infty)^3} \tag{A.19}$$

A.2.3 Internal Heat Re-distribution

The time scale for internal heat redistribution through conduction is estimated using (Williams, 2015)

$$\tau_{\text{cond}} = \frac{\rho_p D_p^2 C_{\text{p}p}}{0.12\kappa_p} \tag{A.20}$$
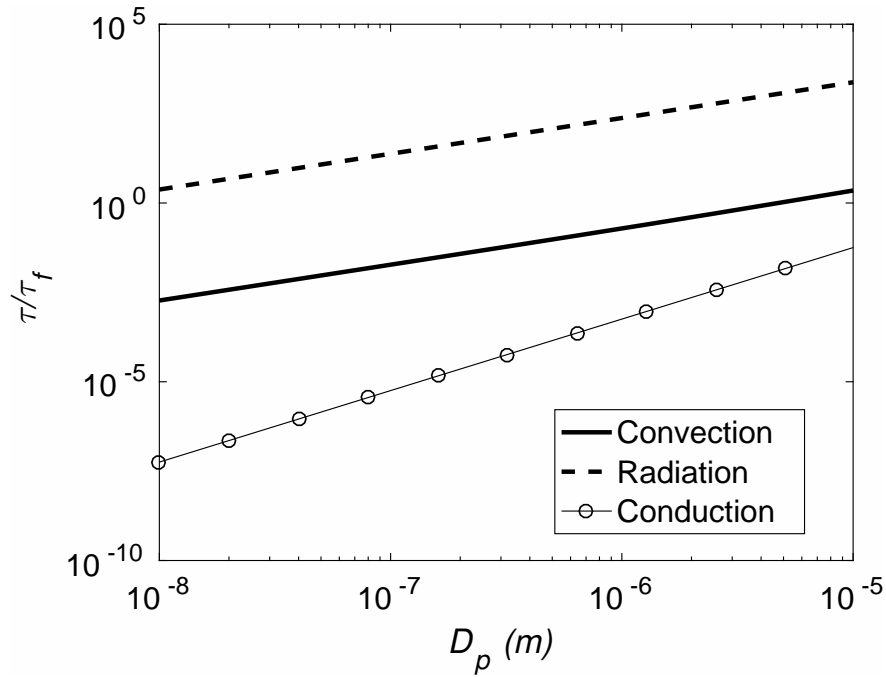

Figure A.2: Thermal time constants of convection, radiation and internal conduction versus the gas flow timescale with particle diameter

The time scales of convection, radiation, and conduction are compared against the flow time scale in Fig. A.2. Heat transfer through radiation takes considerably longer duration than the flow timescale (observed in Fig. A.2). Hence, it has been neglected. At smaller diameters, energy re-distribution within the particle is near-instantaneous. Hence, the temperature is assumed to be uniform within the particle. Hence, the primary mechanism of heat transfer is forced convection at the particle surface, and is combined with the lumped capacitance model for solid interior of the particle.

Appendix B

Derivation of Quasi-1D Compressible Gas-Particle Flows

B.1   Continuity Equation

The flow is assumed to be steady

$$\frac{d\dot{m}_g}{dt} = 0 \tag{B.1}$$

where $\dot{m}_g$ represents the gas mass flow rate.

$$\dot{m}_g = \rho A V = \text{constant} \tag{B.2}$$

B.2   Momentum Equation

The momentum equation for the fluid in this control volume can be written as

$$PA - (P+dP)(A+dA) + \left(P + \frac{dP}{2}\right)dA - F_{np} = \rho A V (V+dV) - \rho A V^2 \tag{B.3}$$

where D_{np} represents the total drag force acting on the particles in the control volume. Simplifying and ignoring higher order terms

$$-AdP - F_{np} = \rho A V dV \tag{B.4}$$

$$AdP + F_{np} + \rho A V dV = 0 \tag{B.5}$$

The momentum equation for a single particle is expressed by

$$F_p = m_p a_p \tag{B.6}$$

$$C_D \frac{1}{2} \rho V_r^2 S_{\text{ref}} = m_p \frac{dV_p}{dt} = m_p V \frac{dV_p}{dx} \tag{B.7}$$

where V_r is the relative velocity of gas w.r.t particles, $S_{\text{ref}} = \pi D_p^2/4$ is the particle reference area and a_p is the particle acceleration.

$$C_D \frac{1}{2} \rho V_r \mid V_r \mid S_{\text{ref}} = m_p V \frac{dV_p}{dx} \tag{B.8}$$

Eq. B.8 represents the momentum equation for a single particle. The particle loading ratio S_L is defined as

$$S_L = \frac{\text{particle mass flow rate } (kg/s)}{\text{gaseous flow rate } (kg/s)} = \frac{\dot{m}_p}{\rho A V} \tag{B.9}$$

The flow is assumed to be steady. Hence, the total mass ratio in the control volume is obtained from

$$S_L = \frac{\dot{m}_p}{\rho A V} = \frac{N_p m_p}{\rho A dx} \tag{B.10}$$

where N_p represents the total number of particles in the control volume of length dx

$$N_p = \frac{S_L \rho A dx}{m_p} \tag{B.11}$$

The net drag force experienced by N_p particles is given by

$$F_{np} = m_p V \frac{dV_p}{dx} \frac{S_L \rho A dx}{m_p} = S_L \rho A V dV_p \tag{B.12}$$

Substituting Eq. B.12 in the fluid momentum equation

$$AdP + (S_L \rho A V)dV_p + \rho A V dV = 0 \tag{B.13}$$

Since $\rho V^2 = \gamma P M^2$,

$$\frac{dP}{P} + \left(\frac{S_\mathrm{L}\rho V}{P}\right) dV_p + \gamma M^2 \frac{dV}{V} = 0 \tag{B.14}$$

$$\frac{dP}{P} + \left(\frac{S_\mathrm{L}V}{RT}\right) dV_p + \gamma M^2 \frac{dV}{V} = 0 \tag{B.15}$$

$$\frac{dP}{P} + \left(\frac{S_\mathrm{L}V}{RT_0}\right)\left(1 + \frac{\gamma-1}{2}M^2\right) dV_p + \gamma M^2 \frac{dV}{V} = 0 \tag{B.16}$$

From ideal gas relation

$$\frac{dP}{P} = \frac{d\rho}{\rho} + \frac{dT}{T} \tag{B.17}$$

Substituting in Eq. B.16

$$\frac{d\rho}{\rho} + \frac{dT}{T} + \left(\frac{S_\mathrm{L}V}{RT_0}\right)\left(1 + \frac{\gamma-1}{2}M^2\right) dV_p + \gamma M^2 \frac{dV}{V} = 0 \tag{B.18}$$

From the Mach number definition

$$\frac{dV}{V} = \frac{dM}{M} + \frac{1}{2}\left(\frac{dT}{T}\right) \tag{B.19}$$

And with the continuity equation

$$\frac{dA}{A} + \frac{d\rho}{\rho} + \frac{dV}{V} = 0 \tag{B.20}$$

Substituting the above relation

$$-\frac{dA}{A} - \frac{dV}{V} + \frac{dT}{T} + \left(\frac{S_\mathrm{L}V}{RT_0}\right)\left(1 + \frac{\gamma-1}{2}M^2\right) dV_p + \gamma M^2 \left(\frac{dM}{M} + \frac{1}{2}\frac{dT}{T}\right) = 0 \tag{B.21}$$

Substituting dV/V from Eq. B.19

$$-\frac{dA}{A} - \frac{dM}{M} - \frac{1}{2}\left(\frac{dT}{T}\right) + \frac{dT}{T} + \left(\frac{S_\mathrm{L}V}{RT_0}\right)\left(1 + \frac{\gamma-1}{2}M^2\right) dV_p + \gamma M^2 \left(\frac{dM}{M} + \frac{1}{2}\frac{dT}{T}\right) = 0 \tag{B.22}$$

From the definition of stagnation temperature

$$\frac{dT}{T} = \frac{dT_0}{T_0} - \frac{(\gamma-1)M^2}{1+\frac{\gamma-1}{2}M^2}\frac{dM}{M}$$
(B.23)

The Equation then becomes

$$-\frac{dA}{A} + \left(\frac{2(M^2-1)}{2+(\gamma-1)M^2}\right)\frac{dM}{M} + \left(\frac{1+\gamma M^2}{2T_0}\right)\frac{dT_0}{T_0} + \left(\frac{S_L V}{RT_0}\right)\left(1+\frac{\gamma-1}{2}M^2\right)dV_p = 0 \quad \text{(B.24)}$$

Rearranging,

$$\left(\frac{-1}{A}\frac{dA}{dx} + \frac{1+\gamma M^2}{2T_0}\frac{dT_0}{dx} + \frac{S_L V}{RT_0}\left(1+\frac{\gamma-1}{2}M^2\right)\frac{dV_p}{dx}\right)\frac{M[2+(\gamma-1)M^2]}{2(1-M^2)} = \frac{dM}{dx} \quad \text{(B.25)}$$

The gaseous momentum equation becomes

$$\left(T_{\text{area}} + T_{\text{energy}} + T_{\text{drag}}\right)\left\{\frac{M[2+(\gamma-1)M^2]}{2(1-M^2)}\right\} = \frac{dM}{dx}$$
(B.26)

$$T_{\text{area}} = \frac{-1}{A}\frac{dA}{dx}$$
(B.27)

$$T_{\text{energy}} = \frac{1+\gamma M^2}{2T_0}\frac{dT_0}{dx}$$
(B.28)

$$T_{\text{drag}} = \frac{S_L V}{RT_0}\left(1+\frac{\gamma-1}{2}M^2\right)\frac{dV_p}{dx}$$
(B.29)

B.3   Energy Equation

The energy transfer in the gas can be expressed through the first Law of thermodynamics

$$\dot{m}_g C_p dT_0 = d\dot{Q}_{np} + \dot{W}_{np}$$
(B.30)

where $\dot{W}_{np}$ is the net work rate done on the gas within the control volume and $d\dot{Q}_{np}$ represents the heat source term on the gas due to the particles within the control volume. The net work rate due

to the drag force on the particle is given by

$$\dot{W}_p = F_p V_p \tag{B.31}$$

The work done on the gas due to N_p particles in the control volume is given by

$$\dot{W}_{np} = -F_{np}V_p = -S_{\text{L}}\rho AVV_p dV_p \tag{B.32}$$

Assuming insulated walls, heat transfer occurs through convection at the gas-particle boundary. Assuming the temperature of the gas to be greater the temperature of the particles

$$\dot{m}_g C_{\text{p}} dT_0 = -N_p h_p A_p (T_{aw} - T_p) - S_{\text{L}}\rho AV_p V dV_p \tag{B.33}$$

The work term arises from the work done by the drag force in the fluid. Since, $h_p = Nu_p \kappa_s / D_p$

$$\dot{m}_g C_{\text{p}} dT_0 = -\frac{S_{\text{L}}\rho A dx N u_{ps}\kappa_s}{m_p D_p} A_p (T_{aw} - T_p) - S_{\text{L}}\rho AVV_p dV_p \tag{B.34}$$

Simplifying

$$C_{\text{p}}\frac{dT_0}{dx} = \frac{-6S_{\text{L}}Nu_{ps}\kappa_s}{\rho_p D_p^2 V}(T_{aw} - T_p) - S_{\text{L}}V_p\frac{dV_p}{dx} \tag{B.35}$$

B.4 Particle Energy Equation

The convective heat transfer over a solid would only impact the thermal energy of the particles. Unlike gases, the mechanical and thermal energy of solids are uncoupled. This is because the solid particles have a tightly packed molecular structure.

$$\frac{6S_{\text{L}}Nu_{ps}\kappa_s(T_{aw} - T_p)\rho A dx}{\rho_p D_p^2} = \dot{m}_p C_{\text{pp}} dT_p \tag{B.36}$$

$$\frac{6S_{\text{L}}Nu_{ps}\kappa_s(T_{aw} - T_p)\rho A dx}{\rho_p D_p^2} = \dot{m}_p C_{\text{pp}} dT_p \tag{B.37}$$

114

$$\frac{6Nu_{ps}\kappa_s(T_{aw}-T_p)}{\rho_p D_p^2 V} = C_{\mathrm{p}p}\frac{dT_p}{dx} \tag{B.38}$$

Appendix C

Scaling Analysis of Compressible Gas-Particle Flows

Undergoing Compression

The characteristic parameters of the gas-particle flow system were identified using an order of magnitude analysis of the governing 1D equations. The following scaling arguments can be made for a gas-particle flow undergoing compression:

1. The stagnation temperature (T_0) scales with the freestream reference value ($T_{0\infty}$).

2. Particles can attain a maximum temperature ($T_p \sim T_{0\infty}$) at the end of compression, and a minimum temperature ($T_p \sim T_{p\infty}$) at the start of compression. Hence, particle temperature (T_p) scales with the term, ($T_{0\infty} - T_{p\infty}$). Similarly, the adiabatic wall temperature (T_{aw}) and temperature difference ($T_{aw} - T_p$) also scale with the term, ($T_{0\infty} - T_{p\infty}$).

3. The gas velocity (V) scales with the freestream value (V_∞).

4. The particle velocity (V_p) scales with $V_{p\infty}$.

5. Axial distance variable (x) scales with the characteristic intake length (L).

Using the above arguments, Eq. 3.14 is non-dimensionalized into

$$\frac{dT_0^*}{d\chi} = -\frac{S_{\mathrm{L}} Nu_{ps} \alpha_{\mathrm{t}}}{3 Stk Pr_{ps}} \frac{\Delta T^*}{\Lambda} - (S_{\mathrm{L}} Ec_p) \Lambda_p \frac{d\Lambda_p}{d\chi} \tag{C.1}$$

where T_0^*, ΔT^*, Λ and Λ_p, and χ are the non-dimensionalized stagnation temperature, temperature difference, gas and particle velocity, and axial distance variable, respectively. S_{L} is the particle

mass loading ratio (Eq. C.2), *Stk* is the Stokes number (Eq. C.3), α_t is the thermal transport number (Eq. C.4), and Ec_p is the particle Eckert number (Eq. C.5).

$$S_L = \frac{\dot{m}_p}{\rho A V} \tag{C.2}$$

$$Stk = \frac{\rho_p D_p^2 V_\infty}{18 \mu L} \tag{C.3}$$

$$\alpha_t = \frac{T_{0\infty} - T_{p\infty}}{T_{0\infty}} \tag{C.4}$$

$$Ec_p = \frac{V_{p\infty}^2}{C_p T_{0\infty}} \tag{C.5}$$

A similar analysis using Eq. 3.14 and 3.16 gives Eq. C.6, and with Eq. 3.10 gives Eq. (C.7).

$$dT_0^* = \left(S_L C_{pr} \alpha_t \right) dT_p^* \tag{C.6}$$

where C_{pr} is the ratio of particle-gas specific heat.

$$\frac{dM}{d\chi} = \mathrm{f}(M) S_L \sqrt{\frac{\gamma}{\gamma - 1}} \sqrt{Ec_p} \frac{\Lambda}{T_0^*} \frac{d\Lambda_p}{d\chi} \tag{C.7}$$

where the expression $\mathrm{f}(M)$ is a function of Mach number. Hence, by observing Eqs. (C.1), (C.6) and (C.7), important particle parameters of interest are S_L, C_{pr}, *Stk*, α_t, and Ec_p. The present study investigates the injection of Boron nano-particles at stoichiometric conditions. This fixes $C_{pr} = 1.02 \approx 1$ and $S_L = 0.105$.

Appendix D

Governing Equations of rhoCentralLPTFoam

D.1 Governing Equations of the Carrier Gas Phase in the Index Notation:

$$\frac{\partial \rho}{\partial t} + \frac{\partial}{\partial x_i}(\rho v_i) = 0 \tag{D.1}$$

$$\frac{\partial}{\partial t}(\rho v_i) + \frac{\partial}{\partial x_i}P + \frac{\partial}{\partial x_j}(\rho v_i v_j - \tau_{ji}) = S_M \tag{D.2}$$

$$\frac{\partial}{\partial t}(\rho E) + \frac{\partial}{\partial x_j}\left(\rho v_j H - \kappa\frac{\partial T}{\partial x_j} - v_i \tau_{ij}\right) = S_E \tag{D.3}$$

$$\tau_{ij} = \mu\left(\frac{\partial v_i}{\partial x_j} + \frac{\partial v_j}{\partial x_j} - \frac{2}{3}\frac{\partial v_k}{\partial x_k}\delta_{ij}\right) \tag{D.4}$$

$$E = e + \frac{v_i v_i}{2} \tag{D.5}$$

$$H = h + \frac{v_i v_i}{2} \tag{D.6}$$

D.2 Governing Equations of the Carrier Gas Phase in the Compact Vector Notation:

Continuity equation:

$$\frac{\partial \rho}{\partial t} + \nabla \cdot (\rho \mathbf{V}) = 0 \tag{D.7}$$

Momentum Equation:

$$\frac{\partial \rho \mathbf{V}}{\partial t} + \nabla \cdot \left[(\rho \mathbf{V})\mathbf{V}^T\right] = -\nabla P + \nabla \cdot \tau + \mathbf{S}_M \tag{D.8}$$

$$\tau = \left[\frac{-2}{3}\mu(\nabla \cdot \mathbf{V})\right]I + \mu\left[(\nabla\mathbf{V}) + (\nabla\mathbf{V})^{\mathrm{T}}\right] \tag{D.9}$$

Energy Equation:

$$\frac{\partial \rho E}{\partial t} + \nabla \cdot [(\rho E)\mathbf{V}] = -\nabla \cdot (P\mathbf{V}) + \nabla \cdot (\tau \cdot \mathbf{V}) - \nabla \cdot \mathbf{Q} + S_E \tag{D.10}$$

$$\mathbf{Q} = -\kappa \nabla T \tag{D.11}$$

D.3 Governing Equations of the Dispersed Solid Phase in the Index Notation:

The Lagrangian module of the solver has been used to model the solid dispersed phase. The particle momentum and energy equations are represented by

$$m_p \frac{dv_{pi}}{dt} = F_{pi} = \frac{\pi D_p^2}{8}\rho C_{\mathrm{D}}(V - V_p)(v_i - v_{pi}) \tag{D.12}$$

where C_{D} is modeled using Eq. 3.1). The model is valid across all rarefaction regimes and when $M_p < 1, Re_p < 200$. The momentum source term due to the particle drag force per unit volume is given by

$$S_{\mathrm{M}} = \frac{1}{v_{\mathrm{cell}}}\frac{3}{4}\Sigma_{N_p}\left[\frac{C_{\mathrm{D}}Re_p m_p \mu}{\rho_p D_p^2}\right](v_{pi} - v_i) \tag{D.13}$$

where v_{cell} represents the cell volume. The particle thermal energy equation is given as

$$m_p C_{\mathrm{p}p}\frac{dT_p}{dt} = h_p A_p(T_{aw} - T_p) \tag{D.14}$$

where A_p is the total surface area of a particle. The convective heat transfer coefficient, h_p, is estimated using the relation

$$h_p = \frac{(Nu_{ps})\kappa_s}{D_p} \tag{D.15}$$

The energy source term due to the nano-particles on the carrier phase is given by

$$S_{\mathrm{E}} = \frac{-1}{v_{\mathrm{cell}}} \Sigma_{N_p} \left(m_p C_{pp} \frac{dT_p}{dt} + F_{pj} v_{pj} \right) \tag{D.16}$$

D.4 Governing Equations of the Dispersed Solid Phase in the Compact Vector Notation:

Momentum Equation:

$$m_p \frac{d\mathbf{V}_p}{dt} = \mathbf{F}_p = \frac{\pi D_p^2}{8} \rho C_D |\mathbf{V} - \mathbf{V}_p| (\mathbf{V} - \mathbf{V}_p) \tag{D.17}$$

$$\mathbf{S}_M = \frac{1}{vol_{\mathrm{cell}}} \frac{3}{4} \Sigma_{N_p} \left[\frac{C_D Re_p m_p \mu}{\rho_p D_p^2} \right] (\mathbf{V}_p - \mathbf{V}) \tag{D.18}$$

Energy Equation:

$$m_p C_{p_p} \frac{dT_p}{dt} = h_p A_p (T_{aw} - T_p) \tag{D.19}$$

$$h_p = \frac{(Nu_{ps}) \kappa_s}{D_p} \tag{D.20}$$

$$T_{ps} = T + 0.5(T_p - T) + 0.22(T_{aw} - T) \tag{D.21}$$

$$T_{aw} = T + r \frac{V_r^2}{2C_p} \tag{D.22}$$

$$r \approx Pr^{0.5} \tag{D.23}$$

$$S_E = \frac{-1}{vol_{\mathrm{cell}}} \Sigma_{N_p} \left(m_p C_{p_p} \frac{dT_p}{dt} + \mathbf{F}_p \cdot \mathbf{V}_p \right) \tag{D.24}$$